A STUDY OF THE MAGNETIC AND STRUCTURAL PROPERTIES OF ULTRATHIN Fe/Ni(111)/W(110) FILMS

A STUDY OF THE MAGNETIC AND STRUCTURAL PROPERTIES OF ULTRATHIN Fe/Ni(111)/W(110) FILMS

By

Hamish Johnston, M.Sc.

A thesis

Submitted to the School of Graduate Studies

in Partial Fulfilment of the Requirements

for the Degree

Doctor of Philosophy

McMaster University

Doctor Of Philosophy (1997) McMaster University
(Physics) Hamilton, Ontario

Title: A Study of the Magnetic and Structural Properties of Ultrathin Fe/Ni(111)/W(110) Films.
Author: Hamish Johnston
Supervisor: Dr. David Venus
Number of Pages: vi, 154

Abstract

The structural and magnetic properties of ultrathin Fe/Ni(111)/W(110) films are investigated using LEED, two Auger electron spectroscopy techniques and magneto-optic Kerr magnetometry. A 2 ML Ni(111) buffer layer is used to grow fcc Fe(111) films to a thickness of 3 monolayers. The Ni substrate allows good wetting and lattice matching of the Fe without significant interfacial diffusion. Above 3 ML a continuous structural transition from fcc to bcc is observed.

An electron energy analyser for use with a spin polarised low energy electron diffraction (SPLEED) electron spin analyser was designed and built. The energy analyser is used to study the growth mode and structure of ultrathin Fe/Ni(111)/W(110) films using angle resolved auger emission spectroscopy (ARAES). A method is developed to fit computer simulations to the ARAES data to determine the growth mode of ultrathin films.

Preliminary magnetic measurements of the fcc phase below 4 ML indicate that the Fe films are ferromagnetic with a magnetic moment perpendicular to the surface at coverages of 0.25 to 2.0 ML. At 2.5 ML a spin reorientation transition appears to occur and both perpendicular and in plane magnetic moments are observed. At 3.0 ML the magnetic moment is in the plane of the film.

Acknowledgments

I would like to acknowledge the significant contribution to this project made by David Venus, whose positive attitude and thoughtful guidance throughout my tenure at McMaster was indispensable. I would also like to acknowledge the technical expertise of Marek Kiela, whose tremendous skills and cheerful determination to get the job done have made this project a success. I would also like to acknowledge the contribution made by Stephen Arnold, whose camaraderie and team oriented approach to research greatly enhanced my experience at McMaster I would also like to acknowledge others who have made contributions to this project including Trevor Jones, Stephen Cool, Stephen Urquhart, James Francis, Tolek Tyliszczak, Chris Mathers, Chris Butcher, Clealand Berwick, Gino Innocenti, Adam Hitchcock, Malcolm Collins and Stewart Johnston.

I wish to thank my parents for their support throughout my time at McMaster. In particular I wish to thank my parents for providing me with a retreat where I could write this thesis in peaceful surroundings.

Table of Contents

Chapter 1

Introduction

Section 1.1

Introduction to Ultrathin Magnetic Films and Structures

The growth of ultrathin magnetic films and structures provides an unique scientific and technological opportunity to study and engineer materials with novel and diverse magnetic properties. By carefully controlling ultrathin film growth, magnetic characteristics such as the direction of the magnetisation and the nature of the magnetic coupling may be modified. This is of great scientific and technological interest because materials may be engineered to exhibit desired magnetic properties such as perpendicular magnetisation and giant magnetoresistance.[1]

From a scientific perspective, ultrathin films provide the opportunity to carefully control individual parameters in a magnetic system. This is possible because magnetic interactions occur over both macroscopic and microscopic length scales. Ultrathin films are in a regime where both macroscopic and microscopic interactions may be controlled. The classic example of this is the phenomenon of perpendicular anisotropy, or the tendency of magnetic moments to align perpendicular to the surface of a magnetic material. The macroscopic demagnetising interaction favours alignment in the plane of the surface. On a microscopic scale, magnetocrystalline anisotropies at the surface often favour perpendicular alignment. For bulk materials the demagnetising interaction dominates and the moments align in plane. However, in an ultrathin film the relative importance of these terms changes and for very thin films the magnetic moments often align perpendicular to the plane.

Materials with perpendicular magnetisation are important from a technological point of view because they have a strong magneto-optic response and play an important role in magneto-optic information storage technology. To increase the magneto-optic response of these materials, layered structures are made by growing magnetic films which alternate between magnetic and non-magnetic layers. If the layer spacing is carefully chosen each magnetic layer will have a perpendicular magnetisation and contribute to the magneto-optic response.

Another phenomenon of ultrathin film magnetism which is of considerable scientific and technological interest is giant magnetoresistance or GMR. Materials which display GMR are also layered structures, with alternating layers of magnetic and non-magnetic (or antiferromagnetic) material. In these structures the magnetic layers are coupled antiferromagnetically across the interleaving material. The nature of this coupling can be precisely engineered by controlling the thickness of the non-magnetic (or anti-ferromagnetic) material. An important consequence of the alternating magnetisation is that the spin polarised conduction electrons from one magnetic layer are scattered by a spin dependant energy barrier at the interface of the next magnetic layer. This results in a large resistance. If the antiferromagnetic coupling is destroyed by applying a magnetic field which aligns the layers, the energy barrier is removed and the resistance drops to that of a typical metal. GMR materials are of considerable technological interest, particularly as magnetic sensors for information storage and other applications.

Another very exciting field of ultrathin film magnetism is the engineering of magnetic materials with crystal structures different than that found in the bulk. For example Fe, which assumes the body centred cubic (bcc) structure at room temperature, can be grown as very thin films with the face centred cubic (fcc) structure. The fcc Fe has very different magnetic properties than bcc Fe, providing remarkable insight into the strong relationship between magnetism and structure.

A common theme in all the examples given above is that the magnetic properties of a system can be studied and controlled by modifying the structure. Therefore, any serious investigation of ultrathin film magnetism must begin with a comprehensive structural study. In the early years of ultrathin film magnetism research, the emphasis was on finding novel magnetic systems often at the expense of careful structural characterisation. However as the field has matured greater emphasis has been placed on the importance of structure in ultrathin magnetism.

Section 1.2

Ultrathin Fe/Ni(111)/W(110) Films

This thesis is concerned with the study of ultrathin Fe films grown on a Ni(111)/W(110) substrate. This system is of particular interest because the Fe initially grows with a fcc structure which is not the normal crystal structure for Fe. As the thickness of the Fe film increases, the structure is expected to revert to bcc. The effect of this structural transition on the magnetic properties of the film is of interest. Also, the magnetocrystalline anisotropy of the Fe(111) surface favours a perpendicular magnetisation whereas the Ni(111) surface anisotropy favours an in plane magnetisation. Therefore Fe(111)/Ni(111) system should be a good candidate for a spin reorientation transition. This will be discussed in greater detail in the following sections of this chapter.

Others have studied fcc Fe(111) films grown on Cu(111) substrates.[2, 3] Although the system has interesting magnetic properties, the structure of the films is complicated by poor growth conditions on Cu(111). In this study a 2 ML (monolayer) Ni 'buffer' film grown on a W(110) surface is used as a substrate. Although the W(110) surface is bcc, the Ni film assumes a fcc structure after the completion of one atomic layer. The Ni(111) substrate was chosen because Ni offers much better growth conditions than Cu. This is discussed in detail in chapters 3 and 4.

Section 1.3

Introduction to Ultrathin Film Magnetism

The most fundamental definition of a magnetic material is a substance which contains magnetic moments which tend to align. For example, in a bar magnet, most of the magnetic moments align along the north-south axis, adding to give a net magnetisation. A bar magnet is an example of a ferromagnet, so named because iron is the prototypical ferromagnet. In an antiferromagnet, the moments align in alternating directions, first north, then south, then north, then south and so on. In an antiferromagnet the moments cancel each other out and there is zero net magnetisation.

These magnetic moments arise from the electrons in the material. Electrons are charged particles, and whenever a charged particle travels in an orbit (or more precisely has orbital angular momentum), a magnetic field is generated. To complicate matters, the electron also has an intrinsic angular momentum (the electron spin) which generates a magnetic field.

In insulators all of the electrons are locked into atomic orbitals and in these materials the nature of the magnetism is atomic. The net angular momentum of the atom is defined by how the electrons fill the orbitals in the ground state. In the atomic model, the exchange interaction encourages electrons in partially filled orbitals to align their spin in the same direction because this minimises the overlap of the electron wave functions and thus the electrostatic energy of the system. Addition of the spin and orbital contributions gives the magnetic moment of the atom.

Metallic Magnetism

In transition metal ferromagnets such as Fe, Co and Ni the picture is more complicated and the nature of the magnetism is not as well understood. In these materials it is the conduction (or itinerant) electrons which are responsible for the magnetism.[4] The conduction electrons are free to travel throughout the metal and are responsible for the conduction of electricity.

Instead of filling atomic orbitals, the conduction electrons (or free electrons) fill energy bands. Energy bands are regions in energy and momentum space and are somewhat analogous to atomic orbitals which are regions in energy and angular momentum space. The energy bands consist of closely spaced quantum states which allow for near continuous change in the energy and momentum of the electrons.

In the free electron model, setting all the electron spins in one direction results in a significant increase in the kinetic energy. Each momentum state may contain two electrons of opposite spin. If the spin of one electron is flipped it must occupy another state (a result of the exclusion principle) and the only available states have a greater kinetic energy. Only if the energy gained through the exchange interaction is greater than the energy lost to kinetic energy will the system be ferromagnetic. This does not occur at metallic electron densities and in almost all metals the electrons spins cancel to give a zero net magnetisation.

The band structure in metallic magnets like Fe is complicated by atomic-like energy bands and it is these bands that are responsible for the magnetism. The magnetic electrons are in the d bands, so named because they are described as linear combinations of d atomic orbitals. The d band electrons 'hop' from atom to atom, being itinerant and atomic at the same time. An important atomic-like property of the d bands is that they are narrow and the energy states are very closely spaced (this is a result of the breaking of translational symmetry, the extreme limit being an ensemble of identical atomic states).

The close spacing in energy states means that the exchange energy can be reduced by aligning spins without a significant increase in kinetic energy. The result is a magnetic polarisation of the d band electrons. This polarisation is normally described as a splitting of the d band into a majority band (parallel to the polarisation) and minority bands (antiparallel to the polarisation). It is this band splitting which is responsible for the giant magnetoresistance phenomenon discussed in section 1.1.

In transition metal antiferromagnets the exchange interaction favours an antiparallel alignment of spins. An antiferromagnetic exchange coupling arises from the oscillatory nature of the electron wave function in space. This is accomplished over several atoms in a spin wave as in Cr.

What determines ferromagnetic or antiferromagnetic behaviour is the precise nature of the d bands. Therefore the magnetism is highly dependent upon the atomic species and the position of the atoms in the lattice.

Electron probes are the ideal tool to study the magnetic properties of transition metal magnets. For example, the polarisation of the conduction electrons can be directly measured to give the magnetisation of the material. The interaction of low energy electrons with the material is dependent upon the magnetisation and can be used to probe the magnetic band structure. A number of magnetically sensitive electron probes will be discussed in chapter 2.

Magnetic Interactions

In any magnetic system there are four important factors which are involved in the magnetism; the exchange interaction, entropy, the dipole interaction and the magnetocrystalline interaction. Each of these contributes to the total free energy of the magnetic system and therefore the equilibrium magnetic state is a function of all four factors.

The exchange interaction may be thought of as the driving force behind magnetic ordering.[5] This is a short range, isotropic quantum mechanical interaction which causes the magnetic moments to align in a ferromagnet. The strength of the exchange interaction is to a good approximation proportional to the number of near neighbours that a magnetic moment has. This has important consequences for magnetic moments at surfaces or in thin films because they have a reduced number of near neighbours.

Entropy is an abstract concept of statistical mechanics which reflects the tendency of matter to seek a state of disorder. This tendency increases with temperature and eventually destroys the magnetism by encouraging the moments to randomly align. It is the relative strength of the exchange and entropy terms which defines the transition temperature at which the magnetism is destroyed. This temperature is called the Curie temperature for ferromagnets and the Neel temperature for antiferromagnets.[6] Above this temperature the entropy dominated paramagnetic phase of random magnetic moment orientation occurs.

The dipole interaction describes the electromagnetic interaction between individual magnetic moments and the magnetic field generated by all the other moments in the material.[6] This is a long range interaction, indeed it is the same interaction that aligns a compass needle in the geomagnetic field. The dipole interaction is often called the demagnetising interaction because it encourages the individual moments to align in the opposite direction of the other moments, reducing the total magnetisation.

The dipole interaction also leads to what is called the shape anisotropy. This refers to the fact that the dipole interaction is sensitive to the macroscopic shape of the magnet. As discussed in section 1.1 the dipole interaction energy is minimised when the magnetic moments align themselves parallel to the surface of a magnet. This explains for example why magnets are manufactured in the shape of a bar and not a sphere. In thin magnetic films the shape anisotropy plays an important role in defining the magnetic properties because the surface is a significant portion of the total magnetic system.

The final important magnetic interaction is the magnetocrystalline interaction.[7] This is an interaction between the magnetic moments and the crystal lattice, which causes the moments to align along certain crystalline directions. This is the result of spin orbit coupling, an electromagnetic interaction between electron spin and electron angular momentum mediated by the presence of the charged atomic cores. For itinerant magnets like Fe and Ni this interaction may be thought of in terms of the spatial relationship between the d bands and the crystalline lattice.

Together the shape anisotropy and the magnetocrystalline anisotropy determine the easy axis of magnetisation of the material, the direction along which the magnetisation will align in the absence of any externally applied magnetic fields. This represents a minimum in the sum of the shape and magnetocrystalline anisotropy free energy terms.

Magnetic Interactions at Surfaces

In a ferromagnet, the direction of the magnetisation is determined by the relative strengths of the demagnetising and magnetocrystalline anisotropy free energies. Near a surface both the demagnetising and magnetocrystalline anisotropies are very different than in the bulk.

The demagnetising shape anisotropy is very sensitive to the presence of the surface because on the vacuum side of the surface there is no magnetic material. The vacuum has a near zero magnetic permeability compared to the material. This means that it costs much more energy to propagate magnetic fields in the vacuum than in the magnetic material. As a result of this, the magnetic moments at the surface tend to point along the surface to minimise the field penetration into the vacuum.

The magnetocrystalline anisotropy is significantly larger at the surface as a result of the broken translational symmetry which occurs when the crystal is terminated at the vacuum. This change in the anisotropy is usually expressed as a surface anisotropy term which reflects the overall change in the anisotropy near the surface. In many materials, the surface anisotropy term favours an easy axis of magnetisation which is perpendicular to the surface. However, at surfaces which are the termination of a bulk material the demagnetising anisotropy energy is much larger and forces the magnetic moments into the surface plane.

Magnetic Interactions in Ultrathin Films

At several atomic layers thickness or less an ultrathin film is two dimensional as far as the conduction electrons are concerned. Mermin and Wagner have shown that a two dimensional isotropic (or Heisenberg) magnet does not order at finite temperatures.[8] However, if anisotropy is introduced to the system, magnetism is expected (and indeed is observed) above 0 K. Therefore magnetocrystalline and shape anisotropies are essential to the existence of ultrathin film magnetism.

Magnetic interactions in ultrathin films are mediated by the same factors as bulk and surface magnetism, except that the relative importance of the terms can be significantly different. A magnetic thin film can be thought of as a system with two surfaces, one of which is terminated by the vacuum and another which is terminated by the substrate material. Therefore surface effects are very important. The demagnetising anisotropy energy is greatly reduced in an ultrathin film because it is a function of the square of the total magnetisation of the material. The surface anisotropy term is significant in ultrathin films because the fraction of the film which is at or near the surface is large.

At very low film thicknesses, the easy axis of magnetisation of an ultrathin film may be perpendicular to the surface of the film. If a perpendicular easy axis is assumed, the anisotropy energies may be expressed as: [9,10]

$$K_{eff} = K_v + \frac{2K_s}{d} - 2\pi M^2 \tag{1}$$

Where K_{eff} is called the effective perpendicular anisotropy energy but is actually the difference in energy between the perpendicular and in plane orientations of the magnetisation. The convention is that positive K_{eff} signifies perpendicular anisotropy so the shape demagnetisation term $2\pi M^2$ is negative. M is the total magnetisation of the system and K_v represents the bulk contribution to the anisotropy energy. K_s is the surface contribution, and d is the thickness of the film.

The bulk and surface anisotropy terms may be positive or negative depending upon the material, the structure of the film and the crystalline orientation of the surface. The factor of two in the surface anisotropy term reflects the fact that there are two surfaces in an ultrathin film. This, however should not be taken too seriously because there is no reason to expect that the anisotropy at the vacuum interface is the same as the anisotropy at the substrate interface.

From equation (1) it is apparent that a sufficiently thin film with a positive surface anisotropy term may have a perpendicular easy axis of magnetisation if the demagnetising and bulk anisotropy terms are overcome. Equation (1) also suggests that there may be a critical film thickness at which K_{eff} becomes negative and the easy axis rotates into the plane of the film. This phenomenon is called a spin reorientation transition and is a subject of current interest in the research community.[10]

The thickness at which K_{eff} becomes zero is also of particular interest because according to the Mermin Wagner theorem, the magnetisation should go to zero because there is no anisotropy. However, there will always be other 'higher order' anisotropy effects present in the films which are likely to stabilise the magnetism. Therefore, the study of films near the reorientation thickness will allow for the study of these higher order effects.

Another important factor which determines the magnetic properties of ultrathin films is structure. If the film growth is pseudomorphic it may have a structure that is different than in the bulk. The example already given is Fe which can be grown as a fcc film under certain conditions. Calculations predict ferromagnetic, antiferromagnetic and zero magnetic coupling for fcc Fe, depending upon the lattice spacing.[11,12] Experiment has confirmed these predictions for fcc Fe grown on Cu(100) and Co(100) where ferromagnetic, non-magnetic and antiferromagnetic behaviour has been observed (to be precise, the ferromagnetic phases have a face centred tetragonal structure).[11-16] The most important parameter which governs the magnetic coupling is the spacing between the atoms in the crystal. In most ultrathin film systems the atomic spacing changes as a function of thickness so a thickness dependence of magnetic coupling is expected.

The magnetocrystalline anisotropy for ultrathin films can be very different than that for the bulk material, either because the film has assumed a different crystal structure or the same structure but with different atomic spacing. Changes to the magnetocrystalline anisotropy caused by changes in atomic spacing (or strain) are referred to as the magnetoelastic anisotropy.[9] The magnetoelastic anisotropy is of particular interest in the study of ultrathin magnetic films because the strain can be a strong function of film thickness.

In an ultrathin film the interfaces between the vacuum and the substrate play important roles in determining the magnetic properties. At both the vacuum and the substrate, the electron band structure changes dramatically. At the vacuum the bands must terminate and therefore have much different spatial properties at the surface than in the bulk. This is the origin of the surface anisotropy term K_s in equation (1). Because the surface is a profound uniaxial anisotropy in the crystal structure, it is manifested as a uniaxial magnetocrystalline anisotropy which often favours a perpendicular magnetisation.

The presence of the substrate may also have important consequences for the magnetocrystalline anisotropy and the magnetic coupling. At the interface between two metals, the conduction electrons move freely from one substance to the other. This means that the conduction bands at the interface must be continuous and this leads to band hybridisation. For materials such as Fe, this hybridisation can be very important because the nature of the magnetism is dependent upon the d bands. If hybridisation occurs between the d bands and the non-magnetic bands of the substrate the magnetism at the interface may be destroyed.

Another important consequence of the interfaces on the band structure is that the two dimensional nature of the ultrathin films tends to make the d bands more 'atomic-like' because crystalline translational symmetry is broken at the surfaces. The result is narrower bands which support a larger magnetisation than the bulk value.[17]

Section 1.4

The Fe/Ni(111)/W(110) Ultrathin Film

The magnetic properties of Fe/Ni(111)/W(110) films should be very interesting because many of the phenomena discussed in the previous section should be present in this system. Studies of the similar Fe/Cu(111) system indicate that at low coverages the Fe assumes the fcc structure of the substrate.[18] Because the Cu(111) and Ni(111) surfaces are very similar, the same is expected in the Fe/Ni(111) system.

The Fe/Ni(111) system is also a prime candidate for a spin reorientation transformation. This is because the Fe(111) surface is expected to have relatively weak positive surface anisotopy term.[9] Therefore if a reorientation transformation occurs it will likely take place at a low Fe film thickness where the structure of the film is best characterised. An interesting complication is that ultrathin Ni(111) films are known to have a negative surface anisotropy term.[9] Therefore the nature of the surface anisotropy of the Fe(111)/Ni(111) interface could be one of weak total anisotropy, ideal for the study of higher order anisotropy effects.

Chapter Two

The Design, Construction and Operation of an Electron Energy Analyser for Spin Polarised Electron Spectroscopy

Section 2.1
Introduction to Electron Energy Analysis

This chapter of the thesis contains a description of the design and construction of a spherical deflector electron energy analyser (SDA) and associated electron optics. The SDA was coupled to an existing electron spin polarisation analyser to create a state of the art instrument for the structural and magnetic study of surfaces and thin films.

In this chapter the fundamental principles of electron energy analysis will be introduced. This is followed by a brief description of the spin analyser and the experimental motivation for the addition of a SDA. Finally design of the SDA will then be presented.

Electron Energy Analysis

When a metallic or semiconductor surface is illuminated with a beam of radiation a large number of electrons are emitted into the vacuum. A wealth of information about the surface is contained in the kinetic energy distribution of these electrons. A number of experimental techniques have been developed to measure this energy distribution.[19]

One of the most common methods of measuring the electron kinetic energy distribution is a band pass kinetic energy filter coupled with an electron counter.[20] A schematic representation of a typical experimental set-up is shown in figure 2-1. A beam of radiation strikes the surface of a sample and electrons are emitted. Some of these electrons are collected in a band pass kinetic energy filter. Only electrons with kinetic energy within a specified range (or band) may pass through the filter, all other electrons

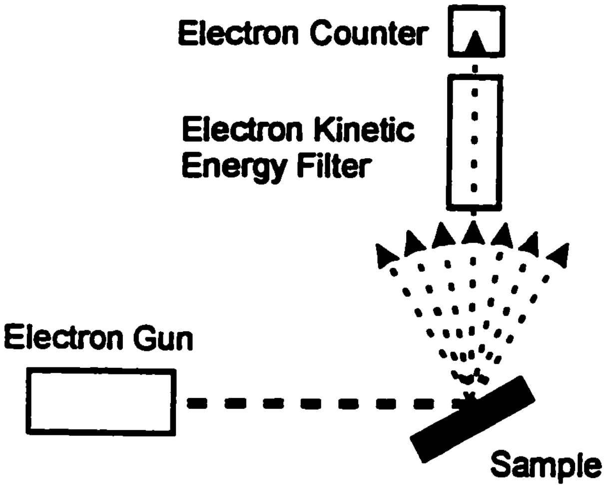

Figure 2-1
An idealised electron spectroscopy experiment.

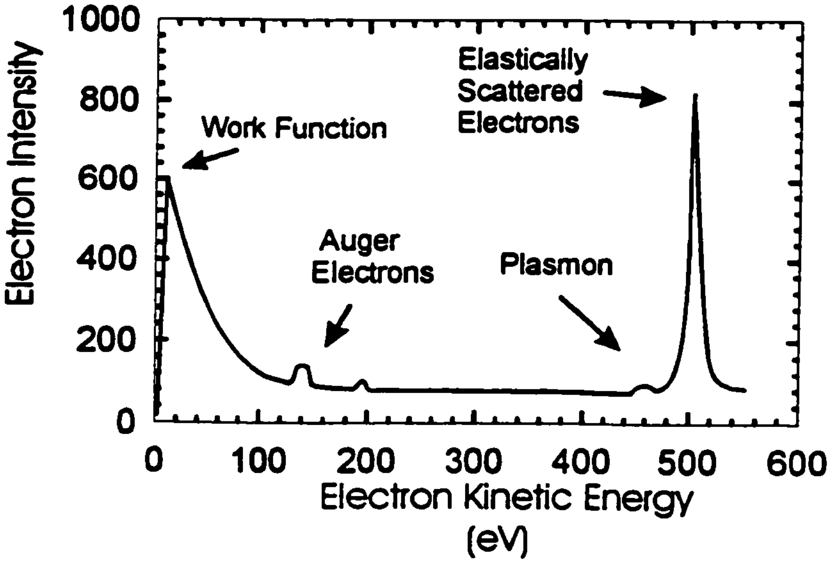

Figure 2-2
Idealised Electron Kinetic Energy Spectrum.

are rejected. After the filter, the counter determines how many electrons per second pass through the filter.

The following idealised experiment will describe a typical measurement using a band pass filter electron energy analyser. A metallic surface is illuminated with a 500 eV electron beam and the apparatus illustrated in figure 2-1 is used to study the emitted electrons. The energy resolution of the filter is set at 5 eV (Er=5 eV). The selection energy (Es) is ramped from 0 to 550 eV in 5 eV steps. At each Es value the electrons are counted for one second.

Figure 2-2 shows an idealised plot of the number of electrons counted in one second as a function of the selection energy Es. This data shows the intensity of the emitted electrons as a function of kinetic energy and is usually referred to as an electron energy spectrum.

In figure 2-2 several features have been schematically included in the kinetic energy spectrum to highlight important phenomena. The large peak at 500 eV is caused by the elastic scattering of the incident 500 eV electron beam. Immediately below the elastic peak is the signature of a plasmon excitation. Here incident 500 eV electrons have lost energy by creating electron oscillations in the metal. The energy of these oscillations is quantised, and thus only fixed values of energy loss are observed. Also represented are Auger electrons which are emitted from atoms which have been excited with radiation (ie the beam of 500 eV electrons). Each element in the periodic table emits a distinct spectrum of Auger electrons and Auger electron spectroscopy is a powerful tool for determining the elemental composition of a surface.

The large background structure which grows at lower energies is the secondary electron spectrum. The 500 eV electrons collide with the resident electrons as they pass through the material. The resident electrons may gain substantial amounts of energy from these collisions and go on to collide with other resident electrons, which in turn gain energy. This process is called a secondary electron cascade, in which one incident 500 eV electron can impart kinetic energy to thousands of resident electrons, many of which are ejected from the material.

The secondary electrons carry magnetic information about the sample material. If the material is magnetised, the resident electrons will have a non-zero spin polarisation. This spin polarisation is preserved (and sometimes enhanced) during the ejection process. Thus the magnetic properties of a material can be studied by measuring the spin polarisation of the secondary electrons.[21]

The sharp cut off in secondary electrons at low energy represents the minimum amount of kinetic energy that an electron must have to escape from the material. This minimum energy is called the work function and is a highly dependent on the structure and composition of the atoms at the surface. Work function measurements are also an important tool of surface science.[19]

Electron Kinetic Energy Analysis Techniques

Over the past one hundred years many different techniques of electron energy analysis have been developed. Because the electron is a charged particle, most of these techniques involve the deflection of a beam of electrons by electric and/or magnetic fields where the degree of deflection is a function of the electron kinetic energy. These techniques are too numerous and varied to be reviewed it this work. The reader is directed to the comprehensive review of Roy and Carette.[20]

Electrostatic Electron Kinetic Energy Analysis

In the electron kinetic energy range of several meV to several keV the most common methods of high resolution energy analysis employ electric fields which reflect or deflect the electron beam.[22] Electrostatic analysers are popular because they are of simple design, using electric fields which are simple to generate and to model. Because no magnetic fields are required, electrostatic energy analysis is the only method used when spin polarised beams of electrons are studied.

Two important principles apply to all electrostatic analysers:[22] The energy resolution increases linearly with the pass kinetic energy. This leads to the principle of 'pre-retardation', by which the energy resolution may be improved by reducing the kinetic energy of the electrons before energy analysis. Also, the energy resolution decreases as the physical size of the analyser is increased. This is because the resolution is dependent upon the spatial dispersion of the electron beam.

Section 2.2

The Experimental Apparatus Before The Addition of Energy Analysis

When the author arrived in January of 1992 the experimental apparatus was contained within a spherical ultra-high vacuum (UHV) chamber. The chamber was equipped with a commercial combination rear-view LEED (low energy electron diffraction)/retarding grid electron energy analyser.[23]

A polished single crystal of tungsten serves as the sample. The sample crystal is mounted on a manipulator arm which allows for linear translations in three directions as well as two angular degrees of freedom, rocking and azimuthal. The tungsten crystal may be annealed and cleaned by electron bombardment heating from a filament mounted behind the crystal in the sample holder.[24]

Thin films of magnetic materials such as iron, cobalt and nickel may be deposited on the tungsten sample crystal using one of three electron bombardment evaporation sources.[25] The structural properties of these thin films may be studied using LEED and Auger electron spectroscopy. These techniques will be discussed elsewhere in this thesis.

The magnetic properties of the thin films were studied using the electron spin analyser. This instrument, described in detail by Sawler and Venus, measures the spin polarisation of a low energy (20 eV to 200 eV) electron beam after scattering from the sample film.[23] The magnetisation of the sample may be changed by creating a magnetic field with two sets of Helmholtz coils mounted on the sample holder.

The original spin analyser was used to study the intensity and spin polarisation of electrons specularly diffracted from the sample crystal. These measurements will be referred to as SPLEED (spin polarised low energy electron diffraction) experiments. In these measurements a beam of electrons with zero spin polarisation is directed at the surface and the diffracted beam is analysed. During the scattering process the specular beam becomes spin polarised by two distinct processes, spin orbit coupling and, if the surface is magnetic, the exchange interaction. Two SPLEED measurements were made: the rotation curves, and magnetic switching.

In a magnetic switching experiment, magnetic field pulses, alternating in direction are applied to the sample. Between pulses, in zero field, the polarisation of the specular beam is measured. If the magnetic pulses are sufficient to flip the direction of the magnetic moments, the magnetic contribution to the spin polarisation of the specular beam will reverse while the spin orbit contribution will remain the same. This magnetic switching is the signature of a magnetic surface and may be used to determine the magnetic properties of thin films.[26]

The rotation curve is a sensitive probe of both the structure and magnetic properties of the surface. When low energy electrons (20 to 200 eV) interact with a surface they typically undergo several scattering processes before they are re-emitted into the vacuum. When this occurs at a crystalline surface, the intensity and spin polarisation of the specular beam is a strong function of the spatial relationship between the electron beam and the surface net. The sample is rotated about the surface normal and the intensity and spin polarisation of the specular beam is measured. Important information about the structural and magnetic properties can be extracted form the intensity and spin polarisation data.[27]

Limitations of the Existing System

The original spin analyser was designed to determine the spin polarisation of electrons elasticity scattered from the sample crystal using retarding grids at the electron detectors. The retarding grid system is ideal for measuring the spin polarisation of elastically scattered electrons because, as illustrated in figure 2-2, no electrons are expected with kinetic energies above the elastic peak. Although the retarding grid system could be modified to measure the electrons below the elastic peak, this would be difficult to implement and would not result in an instrument with good energy resolution. The ability to measure the spin polarisation of electrons as a function of kinetic energy would greatly improve the capability of the instrument and is the major motivation for the addition of an energy analyser.

The electron spin analyser can only measure two of the three components of the electron spin polarisation: the two components of transverse polarisation.[28] The spin analyser is unable to measure the third, longitudinal component. Magnetic switching and rotation curve experiments were therefore unable to probe the third longitudinal component of spin polarisation. The desire to measure the complete spin polarisation of the electron beam was a motivation for the addition of an energy analyser.

Section 2.3

The Addition of a 90° Deflector Energy Analyser

A common way to select the energy of an electron beam is to deflect the beam using a pair of electrodes. To facilitate the measurement of the complete spin polarisation of the electron beam a 90° deflection is required as illustrated in figure 2-3. In this figure the electrons emitted at the sample crystal are gathered by an electron lens, transported to a 90° deflector, and then transported to the spin analyser.

The spin polarisation of the electron beam as it emerges from the sample is shown at the left of figure 2-3. After the 90° deflection, the original component of longitudinal polarisation (P_L) is changed to a transverse polarisation and may be measured. One of the original components of the transverse polarisation remains transverse (P_{TN}) after the deflection and also can be measured. The other component of the transverse polarisation (P_{TP}) has been converted to a longitudinal polarisation. To measure this third component the polarimeter and analyser must be rotated by $\rho = 90^\circ$ about the initial momentum of the scattered electron beam as illustrated at the top of figure 2-3. Therefore a complete determination of the spin polarisation of the electron beam can be made in two measurements.

The 90° SDA Analyser

Several analyser types may be used to deflect an electron beam through 90°. These include the cylindrical mirror analyser (CMA), the cylindrical deflector analyser (CDA) and the spherical deflector analyser (SDA).[22]

The electron optical properties of the energy analyser are important design criteria because as illustrated in figure 2-3, the output of the energy analyser is coupled to the spin analyser. The SDA has the appropriate electron optical properties because it has three dimensional focusing in the Gaussian approximation.[29] This means that the SDA can be easily coupled to electrostatic lenses which also have three dimensional focusing.

The SDA is also the most space efficient 90° analyser, offering the best energy resolution in the limited space available in the vacuum chamber.

Experimental Design Criteria

Before the 90° deflector analyser could be designed, a survey of possible experimental applications was made to define a set of design criteria for the instrument. The important design criteria are energy and momentum resolution and the range of electron kinetic energies over which the instrument can operate.

Four major experimental applications were identified:

Original SPLEED Experiments:

The addition of the energy analyser should enhance the ability to perform SPLEED experiments. These experiments require the analysis of electrons with kinetic energies between 30 and 200 eV with an energy resolution of 2.0 eV fwhm.[23]

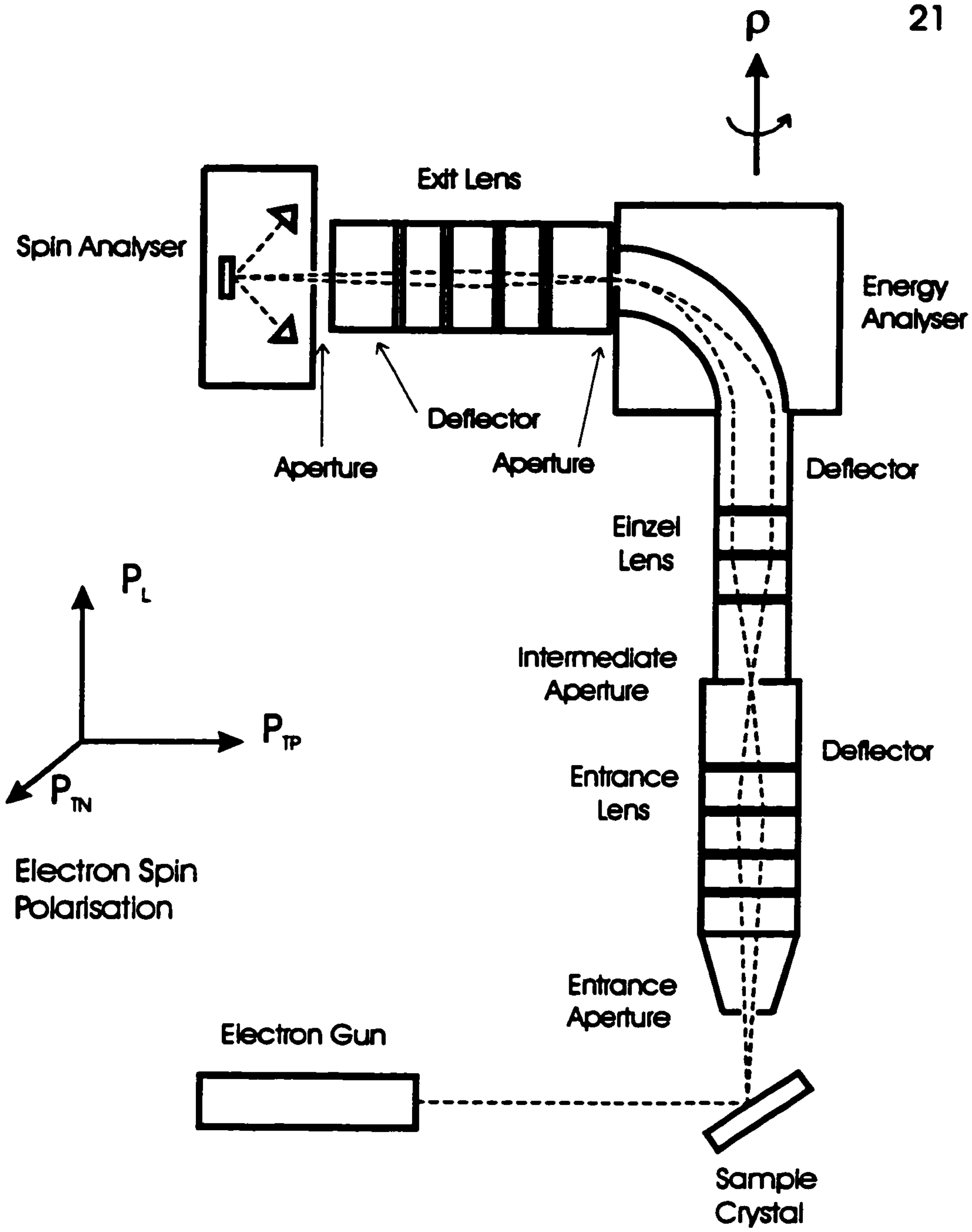

Figure 2-3
Showing the electron optics after the addition of the energy analyser and the three components of electron spin polarisation discussed in the text.

Secondary Electron Magnetometry

These measurements require the analysis of electrons with kinetic energies between the work function (several eV) and 150 eV with an energy resolution of 0.5 eV fwhm at the low energy□end to 2 eV at the high energy end.

Auger Electron Measurements

These measurements require the analysis of electrons with kinetic energies between 30 and 1000 eV with an energy resolution of 2 eV fwhm at the low energy end to 5 eV fwhm at the high energy end.

Spin Polarised Electron Energy Loss Experiments

These measurements require the analysis of electrons with kinetic energies of about 50 eV with an energy resolution of 0.7 eV fwhm.

In all cases an angular resolution of ±2° is appropriate.

The SDA Analyser and Associated Electron Optics

To fulfil the above requirements the following system was designed:

(1) An electron optical input lens which collects electrons from the sample and transports them to an electrostatic energy analyser.

(2) An electrostatic electron energy analyser which has two primary functions:

- (i) To select the kinetic energy of electrons passed to the electron spin analyser.
- (ii) To deflect the electron beam 90°.

(3) An electron optical exit lens which focuses the energy selected electrons from the energy analyser to the spin analyser.

The lens/analyser system is shown in figure 2-3 along with a schematic representation of a typical electron trajectory. A beam of electrons strikes the sample and electrons are scattered and emitted from the surface. These electrons are gathered by the entrance lens and focused to a point at the intermediate aperture. The einzel lens focuses the point source of electrons at the intermediate aperture to a parallel beam at the energy analyser. The energy analyser selects the energy of the electrons and focuses the beam to a point at the exit aperture. Finally the exit lens transports the beam to the spin analyser.

To fully understand the principles behind the design it is prudent to begin with the optical properties of the SDA analyser and work outwards, first towards the sample and then towards the spin analyser.

The 90° SDA Electron Energy Analyser

The SDA used in this design is a 90° quarter hemisphere and consists of inner and outer spherical electrodes separated by a gap, through which the electrons pass. A schematic of the SDA electrodes is shown in figure 2-4.

The operation of the SDA is based on the equation of motion of a particle in a 1/r potential.[30] The general equation of motion is either an ellipse or a parabola with one focus at $r = 0$. When an electron is injected into the region between the inner and outer electrodes it assumes an orbit which is a function of the initial position and momentum of the electron. The potentials placed on the inner and outer electrodes V_{in} and V_{out} may be chosen such that electrons which enter tangentially in the gap at a radius R_0 with kinetic energy K_0 assume a circular orbit. These electrons will emerge 90° away and exit tangentially at a radius R_0. All other electrons will assume elliptical or parabolic orbits. Energy selection is achieved by placing a small aperture at R_0 at the exit of the SDA. This will only allow electrons within the small energy range $K_0 \pm \Delta K$ to pass.

The 90^0 SDA may be thought of as an electrostatic lens with very severe chromatic aberration. For electrons with K_0 kinetic energy the SDA behaves like a lens with one focal point at the exit and the other focal point at infinity in front of the entrance. Therefore a parallel beam of electrons will be focused to a point at the exit as shown in figure 2-3.

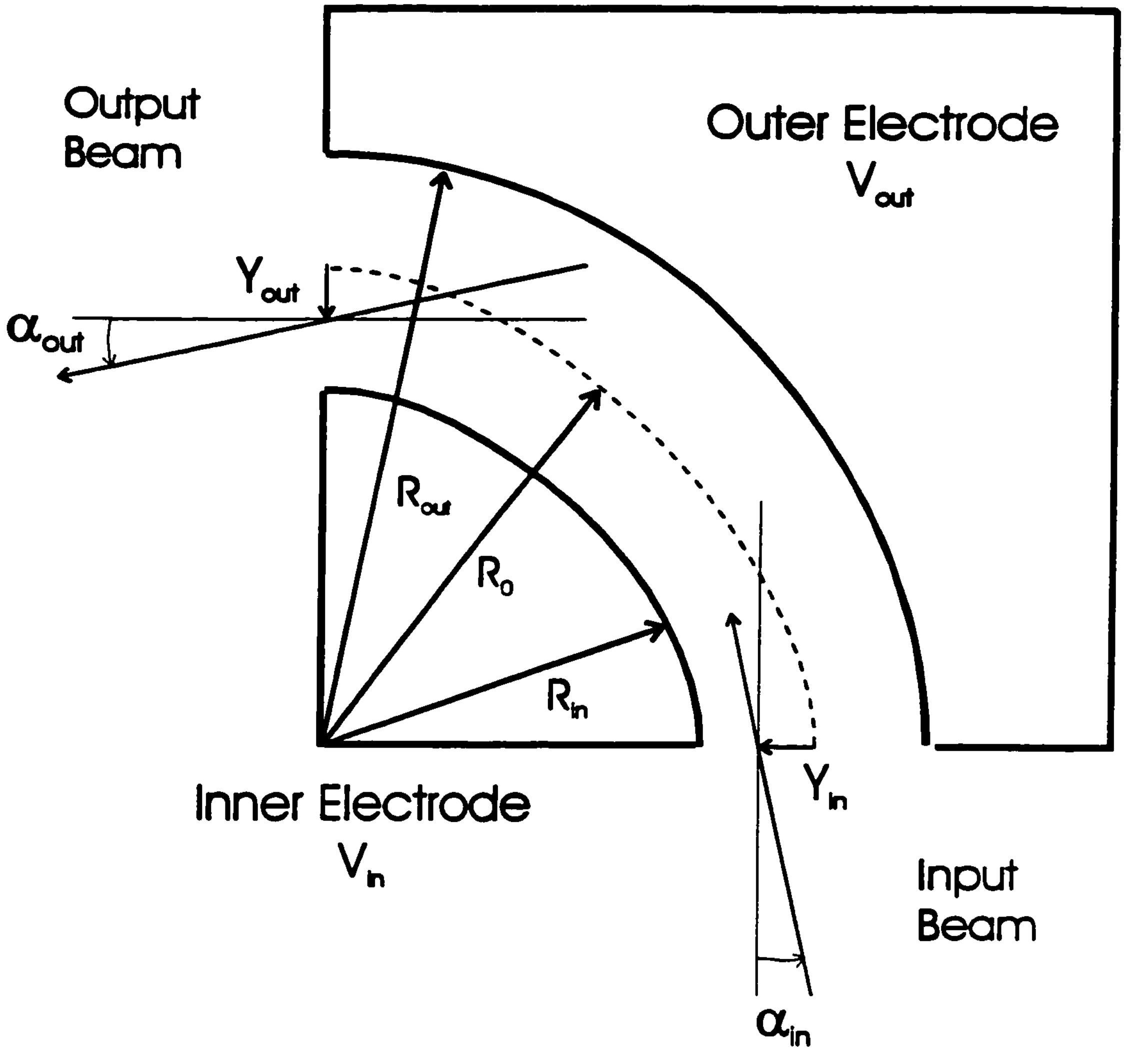

Figure 2-4
Schematic drawing of the SDA showing electrode voltages, radii, and electron optical parameters discussed in the text.

The energy resolving properties of the 90° SDA may be derived from the lens equations, shown truncated after second order.[29]

$$\frac{Y_{out}}{R_0} = \alpha_{in} + \frac{\Delta K}{K_0} - \left(\frac{Y_{in}}{R_0}\right)^2 \qquad (1)$$

$$\alpha_{out} = \frac{-Y_{in}}{R_0} + \frac{\Delta K}{K_0} \qquad (2)$$

Where α_{in} and α_{out}, are the angular divergences from a tangential orbit at the entrance and exit of the analyser and Y_{in} and Y_{out} are the entrance and exit radial divergence from R_0 the pass radius. All of these parameters are illustrated in figure 2-4. ΔK is the deviation in electron kinetic energy from K_0.

If an exit aperture of radius r is assumed, the full width at half maximum energy resolution (fwhm) may be calculated using equations (1) and (2):

$$\Delta K_{fwhm} = C \cdot K_0 \qquad (3)$$

$$C = \alpha_{in} + \frac{r}{R_0} + \frac{1}{2}\left(\frac{Y_{in}}{R_0}\right)^2 \qquad (4)$$

The full calculation is given in Appendix 1.

Equations (3) and (4) suggest two important design principles for achieving a small ΔK_{fwhm}. Equation (3) suggests the kinetic energy of the electrons should be reduced as much as possible before energy analysis. This is the pre-retardation principle. Equation (4) suggests that the pass radius R_0 should be as large as possible.

The optical properties of the SDA may also be deduced from equations (1) and (2). In the Gaussian approximation (to first order, with $\Delta K = 0$) the lens equations are:

$$\frac{Y_{out}}{R_0} = \alpha_{in} \qquad (5)$$

$$\alpha_{out} = \frac{-Y_{in}}{R_0} \tag{6}$$

From (5) it is apparent that a parallel beam at the entrance ($\alpha_{in} = 0$) will be focused at a point at the exit aperture with an angular divergence of given by equation (6).

The 90° SDA requires a parallel beam as input. This is provided by an einzel lens shown in figure 2-3. An einzel lens focuses the electron beam but does not change the electron kinetic energy. The electron lens is operated with one focal point F_1 at the intermediate aperture, and the second focal point at infinity. The lens equations of the einzel lens are similar to that of the SDA and in the Gaussian approximation are given by:

$$\frac{Y_{out}}{F_1} = \alpha_{in} \tag{7}$$

$$\alpha_{out} = \frac{-Y_{in}}{F_1} \tag{8}$$

Where the Y and α parameters are similar to those defined in figure 2-4.

Recalling that the input of the analyser is the output of the einzel lens, equations (3) and (4) may be written as.

$$\Delta K_{fwhm} = \left(\frac{Y_{in}}{F_1} + \frac{r}{R_0} + \frac{1}{2}\left(\frac{\alpha_{in} \cdot F_1}{R_0} \right)^2 \right) K_0 \tag{9}$$

Where Y_{in} and α_{in} refer to the input parameters of the einzel lens. Equation (9) shows that ΔK_{fwhm} will be small when the electron beam at the entrance to the einzel lens is defined by an aperture which restricts Y_{in}.

Because the einzel-SDA system acts like a lens with two finite foci, it is convenient to think of the two as a unit, with an entrance and exit aperture. Equations (5) through (8) can be combined to define the overall lens equations for the einzel/SDA system:

$$M \equiv \left| \frac{Y_{out}}{Y_{in}} \right| = \frac{R_0}{F_1} \tag{10}$$

Where M is the linear magnification and:

$$M\alpha \equiv \left|\frac{\alpha_{out}}{\alpha_{in}}\right| = \frac{F_1}{R_0} \qquad (11)$$

Where M_α is the angular magnification.

For optimum energy resolution, the pass radius of the energy analyser must be as large as possible. In the practical design the available space in the vacuum chamber limited the radius to two inches. Once this parameter was set, the entrance and exit apertures of the einzel-lens system were set at one sixteenth of an inch.

The einzel lens is a three element lens suggested by Harting and Read (A/D = 0.5 and G/D = 0.1).[31] The first and third electrodes are set at the same potential and the second electrode is set at twice this potential, resulting in a focal length of 3.7 inches. This gives an energy resolution of:

$$\Delta K_{fwhm} = \left(0.048 + 1.71\alpha_{in}^2\right)K_0 \qquad (12)$$

Where α_{in} refers to the einzel lens input parameter.

The magnifications are given by:

$$M = 0.54 \qquad (13)$$

$$M_\alpha = 1.85 \qquad (14)$$

It is important to note from equation (12) that an angular divergence of 3° at the entrance of the einzel lens results in a 10% increase in ΔK_{fwhm}. This suggests that a suitable upper limit for the angular divergence at the einzel-SDA entrance is:

$$\alpha_{in} \leq 3^\circ \qquad (15)$$

The Four Element Entrance Lens

To analyse electrons with energies between 0 and 1000 eV, a electrostatic lens must be employed to accelerate the electrons from the emission kinetic energy at the sample to pass kinetic energy at the einzel-SDA. The need for acceleration is most acute during the analysis of high energy Auger electrons (1000 eV). If $\alpha_{in} \equiv 0$ in equation (12) a pass kinetic energy of about 100 eV is required to achieve an energy resolution of 5 eV fwhm. The input lens should therefore be capable of an acceleration ratio of 1/10. For the measurement of low energy secondary electrons (5 to 10 eV) an increase in the kinetic energy is needed to avoid deflection from magnetic fields. An acceleration ratio of 8/1 is suitable for this application.

When operating over this wide range of acceleration ratios the position of the two foci must remain constant at the sample and at the entrance to the einzel-SDA. The magnification of the lens should be controllable to ensure that the angular divergence of the beam is not greater than 3° at the einzel-SDA entrance.

The four element entrance lens shown in figure 2-3 has three degrees of freedom (three potential ratios). One degree of freedom is used to set the acceleration ratio, the second to fix the focal points. The third degree of freedom may be used to control the magnification.

Martinez *et al* have published a number of four element lens designs based on calculations using a charge density method.[32] In these calculations the focal points and one magnification (linear or angular) are kept constant. Operating parameters are found for a range of acceleration ratios for which the Gaussian approximation is valid.

The Martinez lens 'design 5' was chosen. This is the same lens design that was used in the original spin analyser, and therefore is well understood. Martinez provides operating parameters for acceleration ratios (V_4/V_1) between 1/7.7 and 7.7/1, with the linear magnification fixed at 1. The angular magnification may be found using the Helmholz-Lagrange relation: [33]

$$M \cdot M_{\alpha} = \sqrt{\frac{V_1}{V_4}} \tag{16}$$

Where V_1 and V_4 are the electric potentials on the first and fourth lens elements.

Although Martinez *et al* do not present operating parameters for acceleration ratios above 1/7.7, the lens has been successfully operated at ratios of 1/8.5 and 20. The operating parameters were obtained using the ray tracing package SIMION.[34]

Another function of the input lens is to define the electron beam at the einzel-SDA entrance. Much of this definition is done by an entrance aperture (see figure 2-3) which allows for an angular divergence of 1.8° at the lens entrance. From equations (16) the angular divergence at the einzel-SDA entrance is:

$$\alpha_{out} = 1.8^\circ \cdot \sqrt{\frac{V_1}{V_4}} \tag{17}$$

Combining equations (12) and (17), the energy resolution may be expressed as:

$$\Delta K_{fwhm} = \left(0.048 + 0.0017 \cdot \sqrt{\frac{V_1}{V_4}}\right) \cdot K_0 \tag{18}$$

Now that the parameters of the energy resolving portion of the system have been defined, it will be shown that this design satisfies a majority of the design criteria:

Original SPLEED Experiments:

If the 30 to 200 eV electrons are analysed at a pass kinetic energy of 40 eV, energy resolutions between 1.9 and 2.2 eV fwhm are expected. These fwhm values are suitable for SPLEED applications.

Secondary Electron Magnetometry

For the analysis of 5 eV electrons at a pass kinetic energy of 10 eV, an energy resolution of 0.5 eV fwhm is expected. For the analysis of 150 eV electrons at pass kinetic energy of 30 eV an energy resolution of 1.5 eV fwhm is expected. These fwhm values are suitable for secondary electron measurements.

Auger Electron Measurements

For the analysis of 30 eV electrons at a pass kinetic energy of 30 eV an energy resolution of 1.5 eV fwhm is expected. For the analysis of 1000 eV electrons at pass energy of 100 eV an energy resolution of 6.5 eV fwhm is expected. At the low energy limit the fwhm goal is met. At the high energy limit 6.5 eV is larger than the target of 5 eV fwhm, but is not unacceptable.

Spin Polarised Electron Energy Loss Experiments

50 eV electrons would be analysed at a pass kinetic energy of 10 eV with an acceptable energy resolution of 0.53 eV fwhm.

The Four Element Exit Lens

When the electron beam exits the SDA, it must be transported efficiently to the spin analyser and meet input criteria defined by Sawler and Venus:[23] The electrons must have a kinetic energy of 104.5 ± 2.0 eV with respect to the analyser crystal. The pass kinetic energy at the exit of the analyser is between 10 and 200 eV and so the lens must operate at acceleration ratios between about 1/2 and 10. The angular divergence of the electron beam should be no greater than 2.0° at the analyser crystal. The lateral size of the electron beam at the spin analyser crystal must be small enough (0.125 inch diameter) to avoid aperture effects at the four channeltron entrances.

The Martinez four element lens 'design 5' was chosen because it had performed well in the original spin analyser. As well, using the same design for both the entrance and exit lenses greatly simplifies the operation of the instrument. The lens is shown in figure 2-3.

The angular magnification of the exit lens may be expressed as:

$$\alpha_{out} = \alpha_{in}\cdot\sqrt{\frac{V_1}{V_4}} \tag{19}$$

Equation (19) may be combined with equations (17) and (14)

$$\alpha'_{out} = 1.8^\circ\cdot\sqrt{\frac{V_1}{V_4}}\cdot 1.85\cdot\sqrt{\frac{V'_1}{V'_4}} \tag{20}$$

Where α'_{out} is the divergence at the spin analyser crystal, V_1 and V_4 are the potentials on the entrance lens and V'_1 and V'_4 are the potentials on the exit lens. As $V_4 = V'_1$ and V'_4 is always 104.5 eV, equation (20) may be written as:

$$\alpha'_{out} = 0.326\cdot\sqrt{V_1} \tag{21}$$

Where α'_{out} is given in degrees for V_1 in eV. α'_{out} is less than 2° for V_1 less than about 40 eV. For V_1 greater than 40 eV the angular criterion may be met by reducing the radius of the entrance lens aperture from the current 0.0625 inch radius. This would reduce the electron throughput of the instrument.

Overall, the polarimeter is working in a more than satisfactory manner at V_1 values between 30 and 100 eV. Therefore in the near future an angular acceptance of 1.8° at the entrance lens will be used.

The exit lens is operated with a linear magnification of 1 which means that in the Gaussian approximation the radius of electron beam will be 1/16 inch at both the SDA exit aperture and the spin analyser crystal. This is the same radius used by Sawler and Venus in the original spin analyser design.

Deflectors

Deflectors must be incorporated into the electron optics to compensate for misalignment of the electron beam by stray magnetic fields. The general rule calls for a quadrupole deflector before each internal aperture: A deflector in the entrance lens for the intermediate aperture, a deflector in the einzel lens for the SDA exit aperture, and a deflector in the exit lens for the spin analyser entrance aperture. The location of these deflectors is shown in figure 2-3. The deflector in the einzel lens it is not currently used. The deflector in the entrance lens appears to provide sufficient compensation for stray magnetic fields.

Section 2.4

The Physical Realisation of the Instrument

The addition of an energy analyser to an existing ultra high vacuum (UHV) instrument imposes severe restrictions on the physical dimensions of the analyser and the materials used in construction. The operation of the instrument will involve low energy electrons which are easily deflected by geomagnetic fields, therefore magnetic shielding of the energy analyser must be considered.

The Physical Environment

The original spin analyser was housed in a spherical UHV chamber. To accommodate for the addition of an energy analyser, a UHV tee section was purchased. The spherical chamber and tee are shown in figure 2-5. The tee is mounted on a differentially pumped rotatable flange and is free to rotate about the vertical axis.

The sample crystal is located at the centre of the spherical chamber. The electron gun is contained in a LEED/Auger apparatus located on a eight inch flange at the left of the sample. Evaporation sources for depositing magnetic material and a magneto optic Kerr effect (MOKE) apparatus are mounted on various 45° ports (not shown).

The SDA analyser is mounted on the eight inch flange at the top of the tee section. The einzel lens and the entrance lens are attached to the SDA and hang down into the spherical chamber. The spin analyser is mounted on an eight inch flange at the left end of the horizontal tee section. The exit lens is attached to the spin analyser. The exit lens is not attached to the SDA.

The important design limitations imposed by the chamber are apparent in figure 2-5. The distance from the sample to the centre of the tee intersection and the distance from the centre of the tee intersection to the spin analyser crystal define the focal and physical lengths of the lenses. Finally, the inside diameter of the tee, limits the diameters of the lenses and more importantly the space available for the SDA and associated magnetic shielding.

Design Details

A design project of this size requires the careful consideration of hundreds of components, the description of which is not appropriate for this thesis. In this section the important details of the design will be discussed and several technical drawings will be presented.

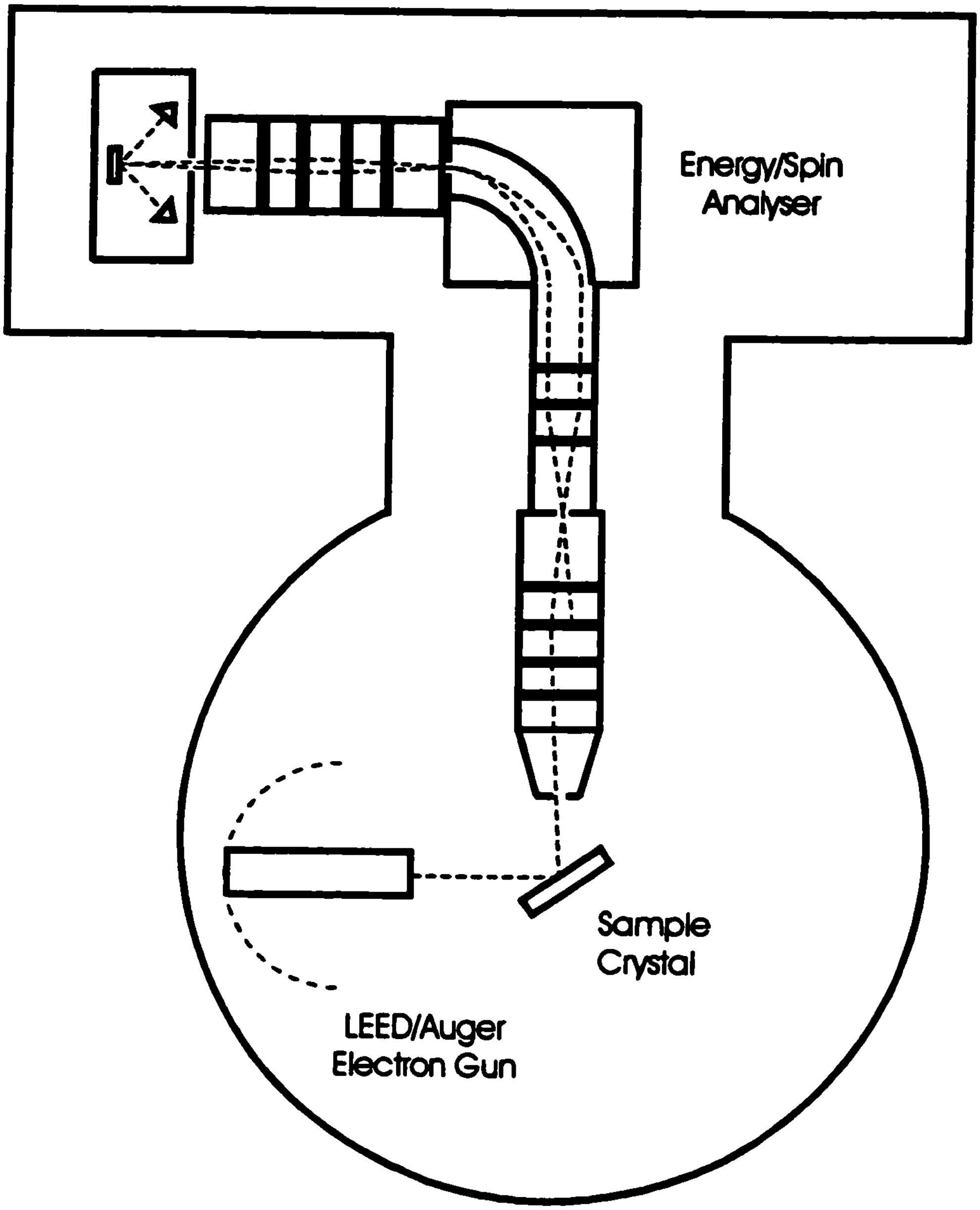

Figure 2-5
Showing the energy analyser in the UHV chamber.

90° SDA:

The principal physical dimensions of the SDA are a 2.0 inch pass radius, a 2.25 inch outer electrode radius and a 1.75 inch inner electrode radius. A cut away view of the SDA is shown in figure 2-6, and all the important components are labeled. The electrodes were machined from blocks of aluminum. The gap between the electrodes is maintained by aluminum side and face plates. The plates are fastened to the electrodes with stainless steel screws and electrical isolation is maintained with ceramic washers The gap between plate and the electrode is maintained with sapphire balls. The face plates have apertures for the entrance and exit of electrons.

A 'lips' and 'tongue' arrangement is employed at the exit of the SDA to try to eliminate rapid changes in the potential where the 1/r potential of the SDA is terminated at the exit face plate. This rapid change can degrade the electron optical and energy resolving properties of the SDA. To make this transition more gradual the fringing corrections suggest by Jost were implemented.[35]

The gap between the inner and outer electrodes at the exit is terminated by electrodes at three potentials. If G is the distance between the electrodes, the outer (inner) G/6 of the gap is terminated with a lip electrode at the outer (inner) electrode potential. A 'tongue' electrode protrudes in from the exit face plate to fill G/6 of the space between the lip electrodes. The exit aperture is at the centre of the tongue, and the hole in the exit face plate is beveled to avoid electrons scattering as they pass through the hole. The entrance aperture of the SDA was designed to be as large as possible to accommodate the parallel beam from the einzel lens so the Jost corrections could not be applied to the input side.

A vertical channel is bored through the outer electrode, along the axis of the input electrons. An electron detector is mounted at the end of the channel. This 'straight through' mode was added for diagnostic purposes, allowing the user to ensure that the input optics are operating properly before the energy analysis is performed. The straight

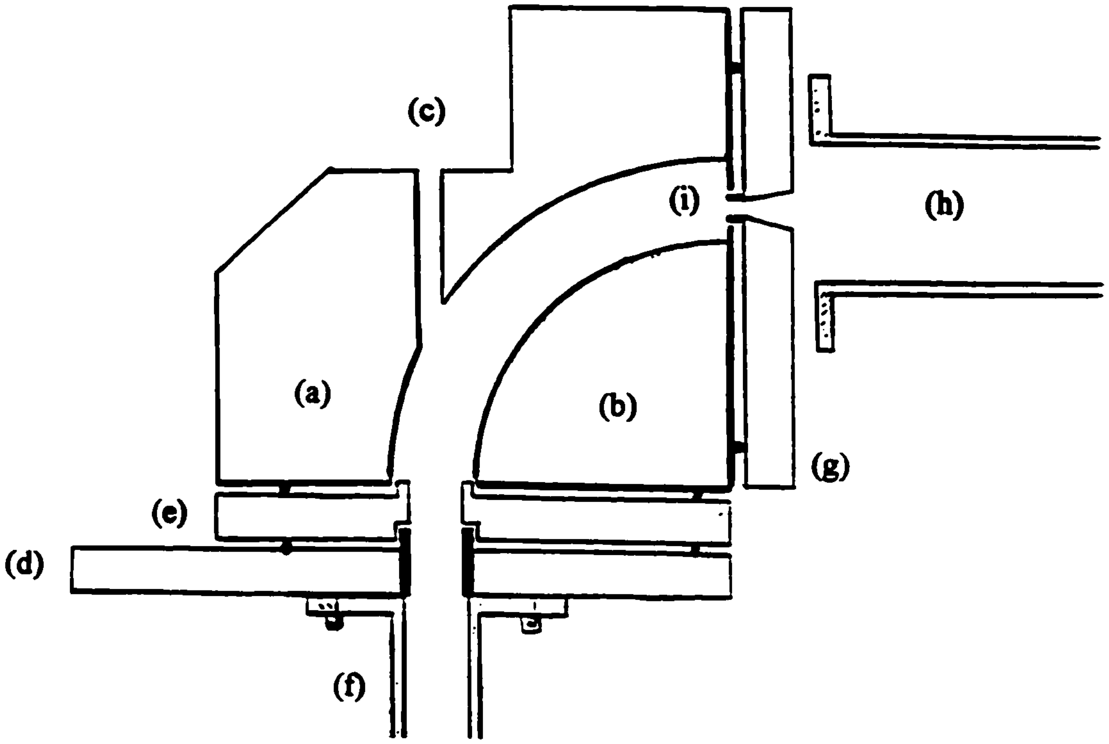

Figure 2-6
Drawing of the assembled energy analyser showing:
(a) Outer spherical electrode, (b) Inner spherical electrode, (c) Straight through passage, (d) Base plate, (e) Entrance plate, (f) Einzel lens, (g) Exit plate, (h) Exit Lens, (i) Exit aperture tongue and lips.

through mode has also be used to perform energy versus intensity LEED studies (I-V curves).

The SDA is mounted on a base plate which hangs rigidly from an eight inch UHV flange. As shown in figure 2-6 the base plate also serves as a mount for the einzel lens. The base plate is electrically isolated from the entrance plate with sapphire balls.

The Einzel Lens

A three element einzel lens with a 0.5 inch inside diameter, and a 3.6 inch object focal length was constructed. A drawing of the einzel lens is presented in figure 2-7. The image focal length is infinite and the physical length of the lens from the intermediate focal point to the entrance of the SDA is 5.6 inches.

The lens consists of 4 cylindrical sections or 'blanks' and an electrostatic quadrupole deflector. The bottom blank is the first electron optical element of the lens, the centre blank the second optical element. The top blank along with the deflector and the drift tube blank compose the third optical element.

The blanks and deflector quadrants are fastened together with threaded rod and electrical isolation is maintained by ceramic washers and spacers. Because the ceramic spacers may be charged by stray electrons a tongue and groove design is employed at the interface between blanks to ensure that stray electric fields will not perturb the electron beam.

The top blank of the entrance lens fastens to the bottom blank of the einzel lens and the two blanks are at the same electric potential. The intermediate aperture is attached to the einzel lens at the interface of the two lenses.

The Entrance Lens

A four element lens with a 1.25 inch inside diameter, and 3.8 inch object and image focal lengths is connected to the bottom of the einzel lens. The physical length of the lens

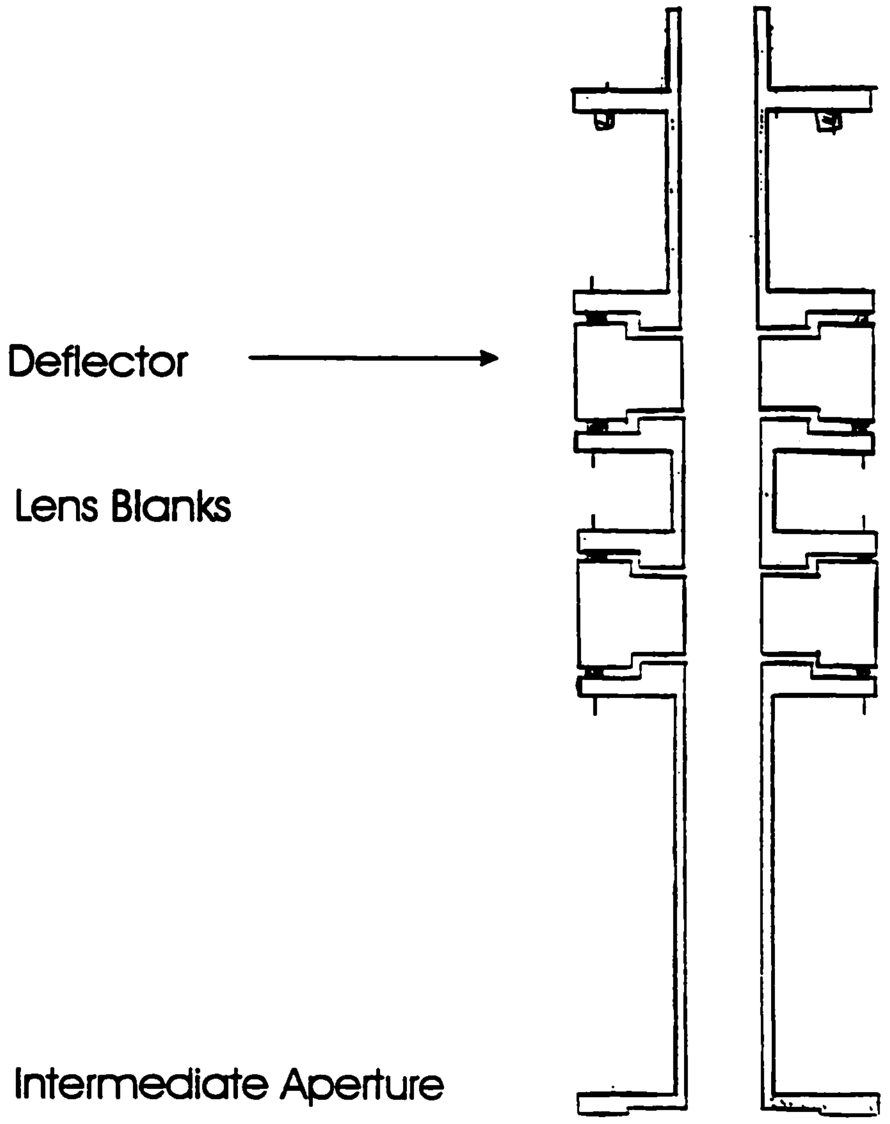

Figure 2-7
Drawing of the einzel lens showing the lens blanks and the location of the intermediate aperture and quadrupole deflector.

from the entrance aperture to the intermediate aperture is 5.6 inches. A drawing of the entrance lens is shown in figure 2-8.

The lens consists of 5 blanks and 1 quadrupole deflector. The bottom three blanks are the first three elements of the lens. The fourth element consists of the deflector and top blank. The lens is fastened together with threaded rod and ceramic washers and spacers. A tongue and groove interface between blanks is also used.

The bottom lens blank is tapered and is fitted with the entrance aperture. The entrance aperture is 2.0 inches above the sample crystal. For a 1/16 inch radius aperture an angular acceptance of ± 1.8° is expected.

SDA Mounting Flange

The einzel-SDA and entrance lens are suspended by a tripod from a specially designed eight inch mounting flange. The flange has eight high voltage BNC connectors and two 10-pin electrical connectors. All electrical connections for the einzel-SDA and entrance lens are made through this flange.

The Exit Lens

The exit lens is attached to the spin analyser and has a 1.1 inch inside diameter and a 3.3 inch object and image focal lengths. Figure 2-9 shows a drawing of the exit lens. The lens consists of 4 blanks and 1 quadrupole deflector. The first three blanks from the bottom are the first three lens elements. The final blank and the deflector constitute the fourth lens element.

When the instrument is assembled in the tee, the entrance to the lens is separated from the SDA exit aperture by a 1/16 inch gap. At this interface the electron beam may have as little as 5 eV kinetic energy. Such a beam is very easily perturbed so the entrance of the lens is large and flared to avoid the penetration of stray electric fields into the gap.

The lens is attached to the spin analyser using the original stainless steel lens adapter (labeled 'spin analyser entrance aperture' in figure 2-9). The exit lens is very

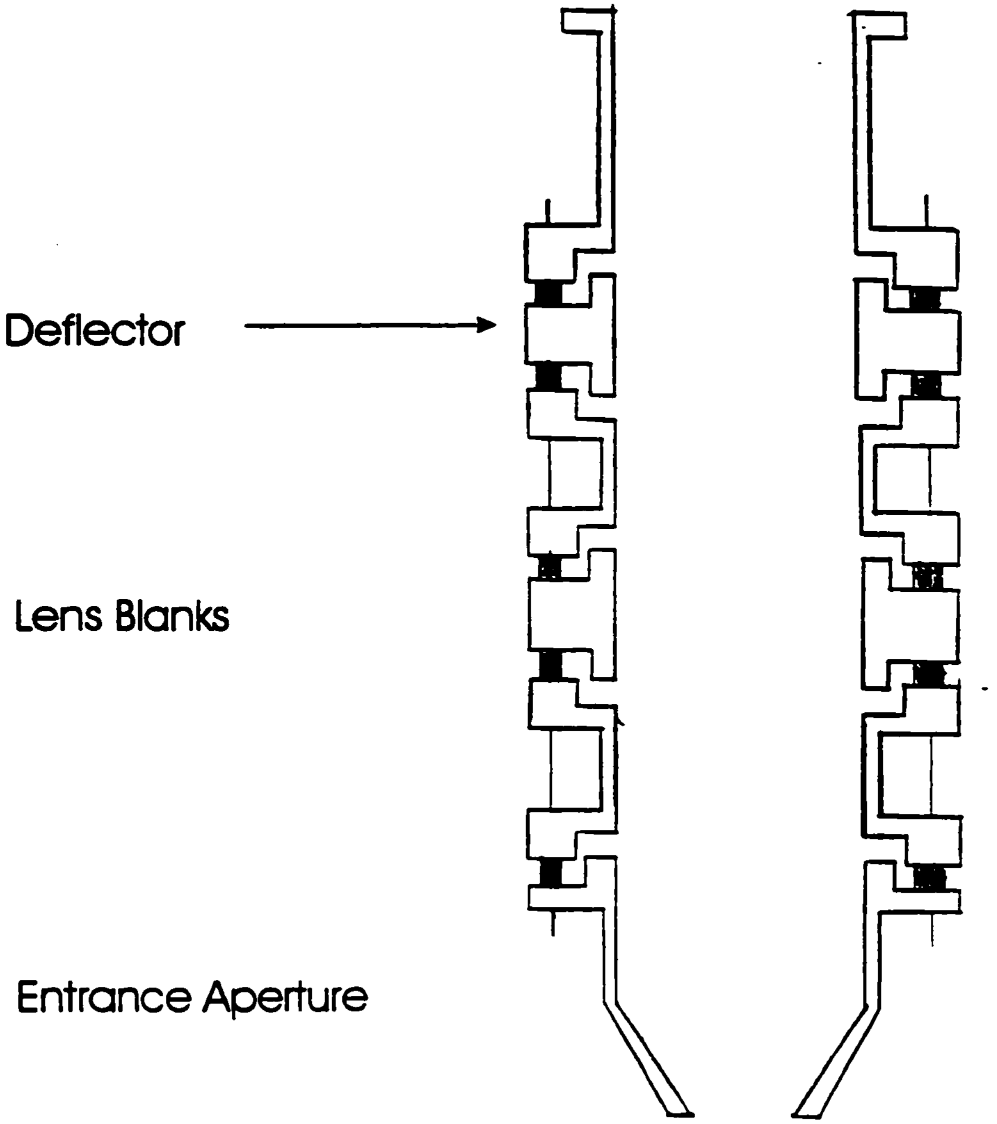

Figure 2-8
Drawing of the entrance lens showing the lens blanks and the location of the entrance aperture and quadrupole deflector.

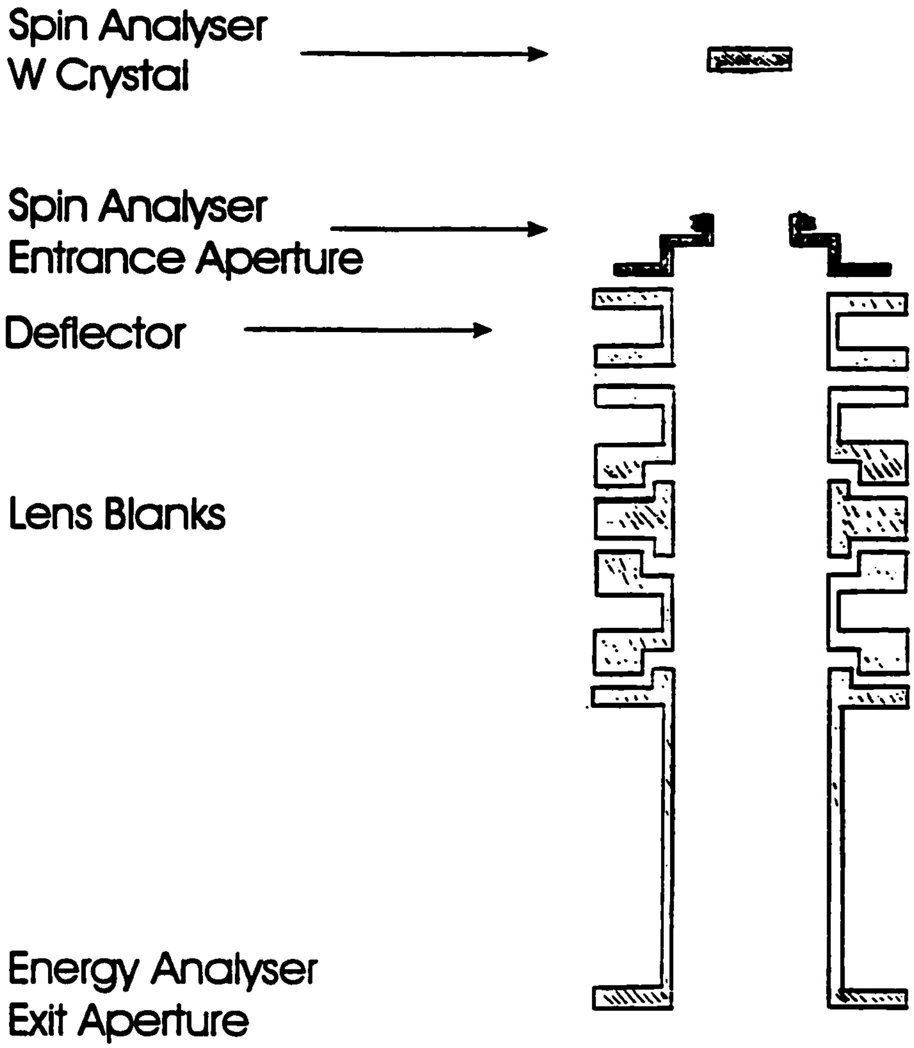

Figure 2-9
Drawing of the exit lens showing the lens blanks and the location of the energy analyser exit aperture, quadrupole deflector, spin analyser entrance aperture and the spin analyser crystal.

similar to the lens used in the original design so the existing electrical connections at the spin analyser mounting flange are used.

The lens is fastened together with threaded rod and ceramic washers and spacers. A tongue and groove interface between blanks is used, except for the deflector because at this point the electron beam will always have an kinetic energy of 104.5 eV and is not easily perturbed by stray electric fields.

UHV and Electron Optical Compatible Materials

In an ultra high vacuum environment great care must be taken to avoid contamination by choosing the appropriate construction materials. The materials must be robust at elevated temperatures as part of the UHV pumping process involves heating of the entire chamber to 150° C for several hours. Magnetic materials must be avoided because low energy electrons are easily deflected by stray magnetic fields.

All of the conducting electrodes are aluminum, a strong, light weight, UHV compatible and non-magnetic metal which is easy to machine. Unfortunately aluminum surfaces quickly oxidise, creating electrode surfaces with uneven electric potentials. To eliminate this problem, all aluminum surfaces which are exposed to the electron beam are coated with graphite, in the form of the commercially available aerosol Aerodag.[36]

All fasteners used in construction are stainless steel or copper. Some stainless steel may be magnetic so before installation all stainless steel fasteners were surveyed with a Hall probe (magnetic detector) to ensure that they were not (or only slightly) magnetic. All insulators used were ceramic, and Macor [37] machinable ceramic was used for custom parts. Electrical connections were made with bare tantalum and tungsten wire, as well as copper wire insulated with a UHV compatible varnish.

Magnetic Shielding

To analyse low energy electrons the SDA must be shielded from the geomagnetic field. An upper tolerance for the magnetic field can be estimated by defining a maximum allowable magnetic deflection. The low energy electron path length through the einzel drift tube and the SDA has a path length of 5.4 inches. It is reasonable to expect that a magnetic deflection of one aperture radius (0.062 inches) could be corrected with deflectors without and serious degradation of the energy resolution or electron optics. This deflection sets a limit of about 10 milligauss, a factor of 50 reduction in the magnitude of the geomagnetic field

Originally, the geomagnetic field was nulled by surrounding the entire UHV chamber with three sets of square Helmholz coils. This is effective at nulling fields at the centre of the chamber but physical limits on the maximum size of the coils causes the nulling effect to drop off rapidly away from the centre of the chamber.

To achieve the 10 milligauss target, the portion of the tee which contains the electron optics was lined with mu-metal, an iron alloy with a very high magnetic permeability.[38] The energy of the geomagnetic field is minimised by concentrating field lines into regions of high permeability, and magnetic shielding is achieved by 'conducting' field lines around a region by surrounding it with mu-metal.

Tubes 5.75 inches OD were rolled out of Conetic AA mu-metal[39] (0.01 inch thick). The tubes are two ply, and were spot welded to prevent unraveling. A hole was cut in the vertical tube and one end of the horizontal tube was tapered so that the tubes mated properly at the tee intersection. Extra material was included at the intersection to ensure complete shielding. A mu-metal cap was made for the top of the vertical tube. The vertical tube extends into the spherical chamber to within 5.4 inches of the sample crystal.

In situ Hall probe measurements made before the analyser was installed showed that the magnetic field in the crucial tee intersection region was 10 milligauss or less. These measurements were made with the Helmholz coils on.

Section 2.5
Operation of the Energy/Spin Analyser

Although the operation of the SDA is relatively simple, great confusion may occur when the novice (and sometimes the experienced) attempts to set the SDA potentials. This usually occurs when the user confuses the potential and kinetic energies of the electrons. In this work the kinetic energy of the electron will always be represented with a capital K.

The operating principles of the instrument are best illustrated with electron kinetic and potential energy diagrams. Figure 2-10 shows the kinetic energy of the electrons as they pass through the three principal electrostatic potentials of the instrument: The sample potential (SAMPLE), the einzel-SDA potential (PASS), and the spin analyser potential (L_4).

The example shown in figure 2-10 is a pre-retardation mode in which the kinetic energy of 170 eV Auger electrons is reduced to 50 eV before energy analysis. The entrance lens must reduce the electron kinetic energy by 150 eV. This done by setting the einzel-SDA potential at -120 V with respect to the sample.

After the 50 eV electrons emerge from the SDA they must be accelerated to a kinetic energy of 104.5 eV at the spin analyser. This done by accelerating the electrons 54.5 eV by setting the potential at the spin analyser at +54.5 V with respect to the SDA.

Modes of Energy Analysis

To obtain an electron kinetic energy spectrum it must be possible to scan through a range of kinetic energies with the analyser. In their comprehensive review article, Roy and Tremblay identify two fundamental modes of operation; constant acceleration and constant relative resolution.[22]

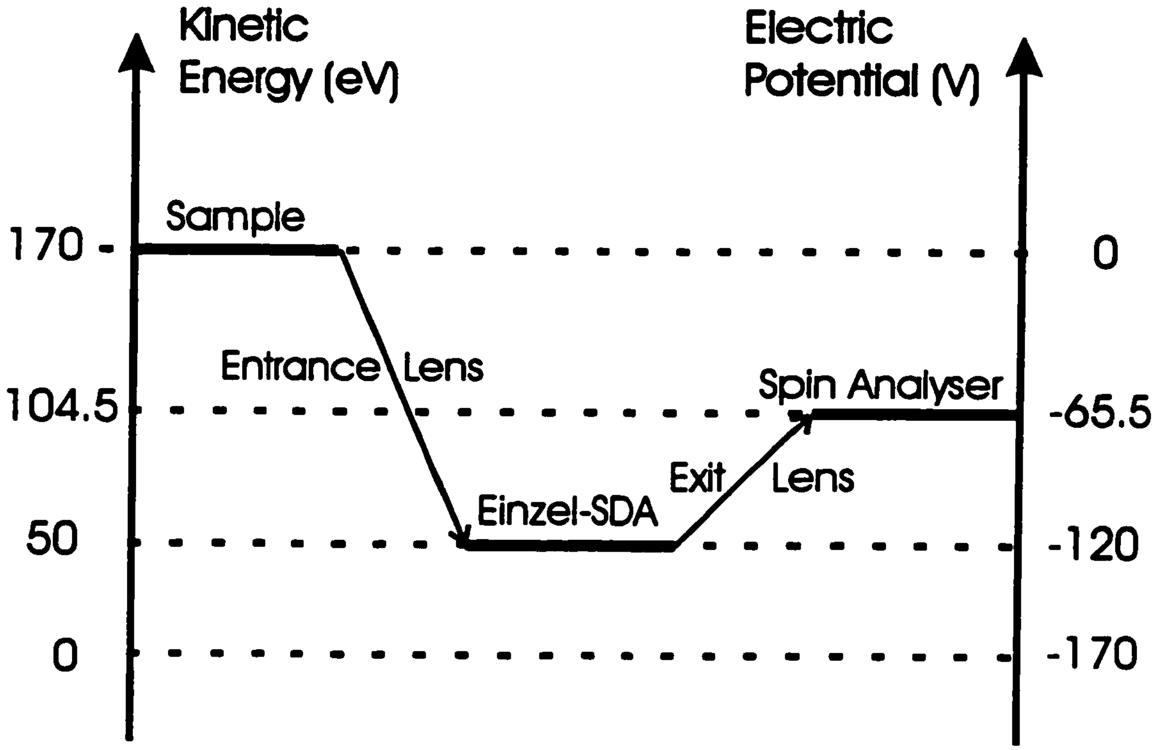

Figure 2-10
Electron kinetic and potential energy diagram showing the three principle energies discussed in the text.

The Constant Acceleration or Constant Resolution Mode

In this mode of operation the accelerating potential between the sample and the SDA is kept constant. The selection energy of the SDA is varied by changing the potential difference across the spherical electrodes. This technique is most appropriate when there is no input electron optics and the entrance aperture of the SDA simply views the sample. If there are entrance and exit optics (as in this design) this mode is difficult to implement because the varied kinetic energy of the input and output beams introduces complicated focusing problems. As suggested by the title, the energy resolution of the SDA in this mode remains constant as the potential difference across the spherical electrodes is scanned.

The Constant Relative Resolution Mode

In this mode the potential difference across the SDA electrodes is kept constant and the accelerating potential between the sample and the SDA is varied. The kinetic energy of the passed electrons remains constant (it is defined by the potential difference across the SDA electrodes.

In this instrument the constant relative resolution mode is used exclusively because in this mode it is easier to achieve good focusing of the input lens during an energy scan. This mode is best described by referring again to the example in figure 2-10 which shows the system retarding 170 eV electrons to a pass kinetic energy of 50 eV. To perform an energy scan between 150 and 190 eV the potential at the einzel-SDA is varied between -100 and -140 V. When -100 V is applied at the SDA, 150 eV electrons will have 50 eV kinetic energy at the SDA. When -140 V is applied at the SDA 190 eV electrons will have 50 eV kinetic energy at the SDA.

Because the electrons always emerge from the SDA with 50 eV kinetic energy, the potential difference between the SDA and the spin analyser remains fixed during the scan. Data taken using the above settings is discussed near the end of this chapter.

A Detailed Description of the Operation of the Instrument

The electronics which supplies the many potentials required to operate the instrument was designed and built by Marek Kiela in consultation with the author and David Venus. Because this instrument was built in stages the electronics is of varied design, the newer components having both manual and computer control modes and the older components having only manual control.

Figure 2-11 shows all of the electric potentials used in the instrument. This is a more detailed representation of the same pre-retardation mode shown in figure 2-10. In the figure various potentials are connected to others with arrows. This indicates that the potential at the head of the arrow is referred to the potential at the tail of the arrow. The following are the principal potentials:

SAMPLE: The sample potential

Under most circumstances, the sample is held at ground. This defines the initial kinetic energy of the electrons. The aperture and first element of the entrance lens are also normally set at SAMPLE.

P_1: The Retarding Potential

P_1 is a negative voltage which is usually applied via a connection to the Spectaleed LEED power supply. P_1 may be manually or computer controlled. As indicated in figure 2-11, PASS and all other potentials except P_2 and P_3 float on P_1.

When the Spectaleed LEED power supply is used P_1 can be set between 0 and -1000 V.

PASS: The Selection Energy:

This is the potential which defines the kinetic energy of the electrons which enter the einzel-SDA. PASS is referred to P_1 and may be manually or computer controlled. Under normal operating conditions P_1 is used as a retarding reference potential. In figure 2-11 P_1 is set at - 170 V so that when PASS is set at + 50 V the pass kinetic energy is 50 eV.

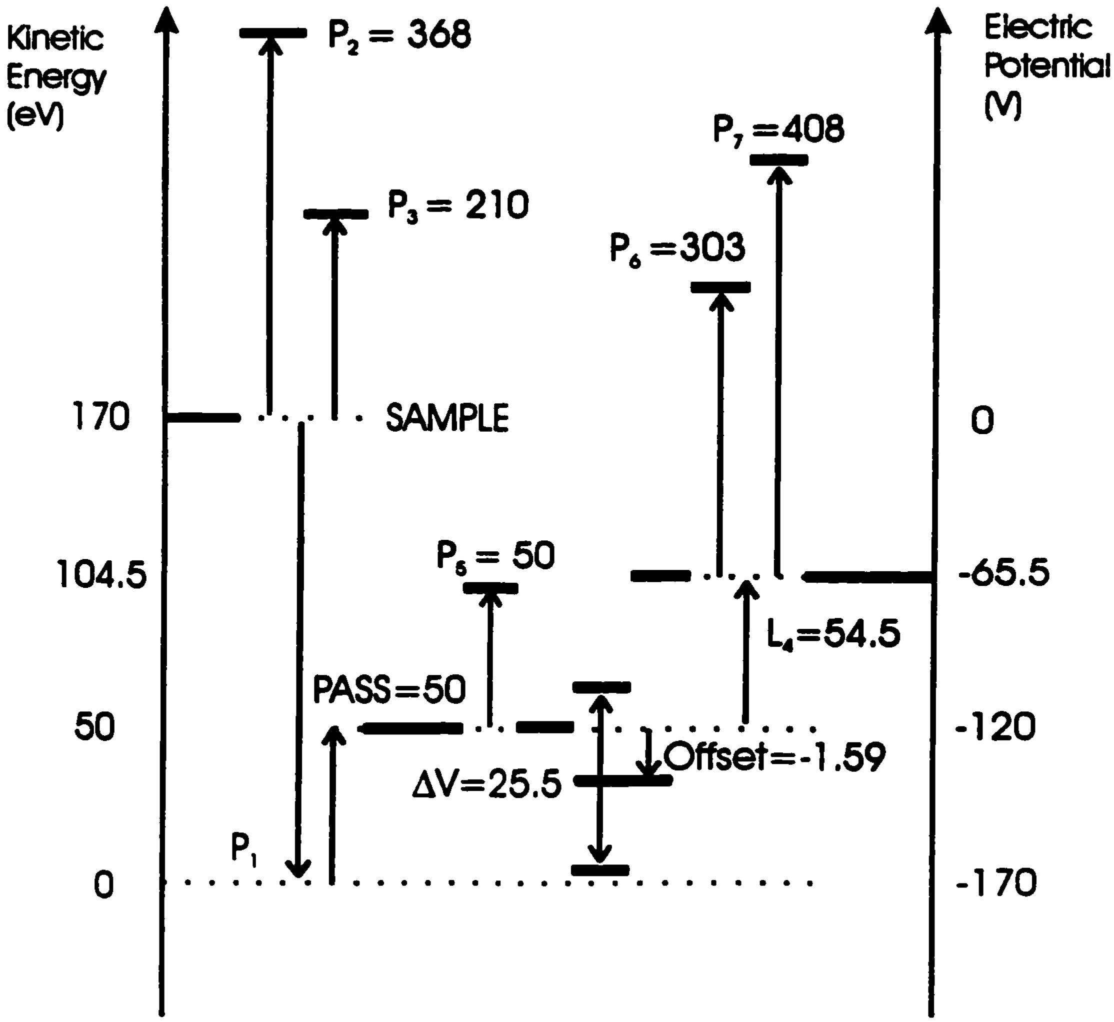

Figure 2-11
Electron kinetic and potential energy diagram showing all potentials used in the energy analyser. All electric potentials at the head of an arrow are with respect to the potential at the tail of the arrow. The example given is the same as that in figure 2-10.

The first and third elements of the einzel lens, the base plate, the entrance and exit face plates, the side plates and the first element of the exit lens are all set at PASS. The PASS potential can vary between 0 and 1000 V.

L_4: The Spin Analyser Energy:

This defines the electron kinetic energy at the spin analyser (which always is set at 104.5 eV). L_4 is referred to PASS. L_4 may only be manually controlled in the range ± 100 V.

There are numerous intermediate potentials which will also be defined:

P_2 and P_3

These two potentials constitute the second and third lens element of the input four element lens. They are referred to ground and may be manually or computer controlled between ± 1000 V.

P_4 through P_7:

Currently P_4 is not used. It was designed to be connected to the fourth element of the entrance and the first element of the einzel lens. In this mode, the three element lens could be used as an accelerating lens. P_5 is the potential set on the second element of the input three element lens. P_6 and P_7 set on the second and third lens elements of the exit lens. Potentials P_4 through to P_7 are all referred to PASS and may be manually or computer controlled. They may be set between 0 and 1000 V.

Currently there are two sets of quadrupole deflector potentials: D_1 and D_2 connected to the quadrupole deflector in the entrance lens and D_3 and D_4 connected to the quadrupole deflector in the exit lens.

Setting the SDA Potentials

The SDA consists of two spherical electrodes set at different electrostatic potentials: V_{in} on the inner electrode and V_{out} on the outer electrode. These two degrees of freedom define the electron optical properties of the SDA. The pass kinetic energy K_0, and the pass radius R_0 are related by: [22]

$$K_0 = \frac{e \cdot (V_{in} - V_{out}) \cdot R_{in} \cdot R_{out}}{2 \cdot R_0 \cdot (R_{out} - R_{in})} \qquad (21)$$

Where R_{in} (R_{out}) is the radius of the inner (outer) electrode and e is the charge on the electron. For ease of design the pass radius is set at the mean radius:

$$R_0 = \frac{R_{out} + R_{in}}{2} \qquad (22)$$

From equations (21) and (22) and the physical dimensions of the SDA give in section 2-4:

$$V_{in} - V_{out} = \Delta P = (0.5079) \cdot K_0 \qquad (23)$$

The analyser controller provides two potentials:

$$V_{in} = PASS + \frac{\Delta P}{2} + P_{off} \qquad (24)$$

$$V_{out} = PASS - \frac{\Delta P}{2} + P_{off} \qquad (25)$$

Where P_{off} is an offset potential which is used to set the potential at R_0. The potential between the gap is not a linear function of the radial position. The potential at R_0 is given by P_0:

$$P_0 = V_{in} - \left(V_{in} - V_{out}\right) \cdot \left(1 - \frac{2 \cdot R_{in}}{R_{in} + R_{out}}\right) \cdot \frac{Rout}{Rout - Rin} + P_{off} \qquad (26)$$

P_0 is the electric potential at the pass radius and is therefore the SDA potential. The electron beam enters the SDA at the pass kinetic energy K_0, defined by the PASS potential. To avoid acceleration upon entry of the SDA, P_{off} is used to set the potential P_0 at PASS. For our SDA :

$$P_{off} = -0.03175 \cdot P_0 \qquad (27)$$

It is important to note that in figure 2-11 and on the energy analyser power supply $\Delta P = 2 \bullet \Delta V$, as the electronics provide $\pm \Delta V$ to the inner and outer electrodes.

Section 2.6

Testing and Characterisation of the Instrument

To ensure that the instrument meets the experimental criteria defined in section 2.2 a series of test measurements were made. These measurements are representative of the modes of operation of the instrument and will serve as a guide for future users.

The energy resolution of the instrument will not be discussed for the representative measurements. Rather a comprehensive characterisation of the resolution as a function of pass kinetic energy will be presented at the end of this chapter.

SPLEED Experiments

Shortly after the instrument was completed the author performed SPLEED magnetic switching and rotation curve experiments. More recently, graduate student Stephen Cool has used the instrument to study clean and Ni covered W(110) surfaces with rotation curves. Cool has obtained a series of rotation curves at energies between 30 and 100 eV. The quality of the data is high, with the contrast in intensity and polarisation showing significant improvement over the original instrument. This improvement is attributed to the superior energy and momentum resolving capabilities of the SDA.

An example of Cool's work is given in figure 2-12. This is a rotation curve of the clean W sample using 30 eV incident electrons and a pass kinetic energy of 100 eV. The sample crystal is rotated about the surface normal, and 0° in the figure corresponds to the W<011> surface direction being in the scattering plane. The measurements at the top of the figure were made with the rotating flange in the same configuration as shown in figure 2-1. In this configuration the component of transverse spin polarisation normal to the scattering plane (P_{TN}) is measured along with the longitudinal spin polarisation (P_L) which Cool labels P_n and P_k respectively. The spin polarisation data is represented by the error bars resulting from counting statistics, with the lines given by explicit symmetrization or antisymmetrization of the data about the origin. These lines demonstrate that the measured polarisation has the expected rotation (anti)symmetry.[28] The thin solid line is the measured intensity of the specular beam. The measurements at the bottom of the figure were made

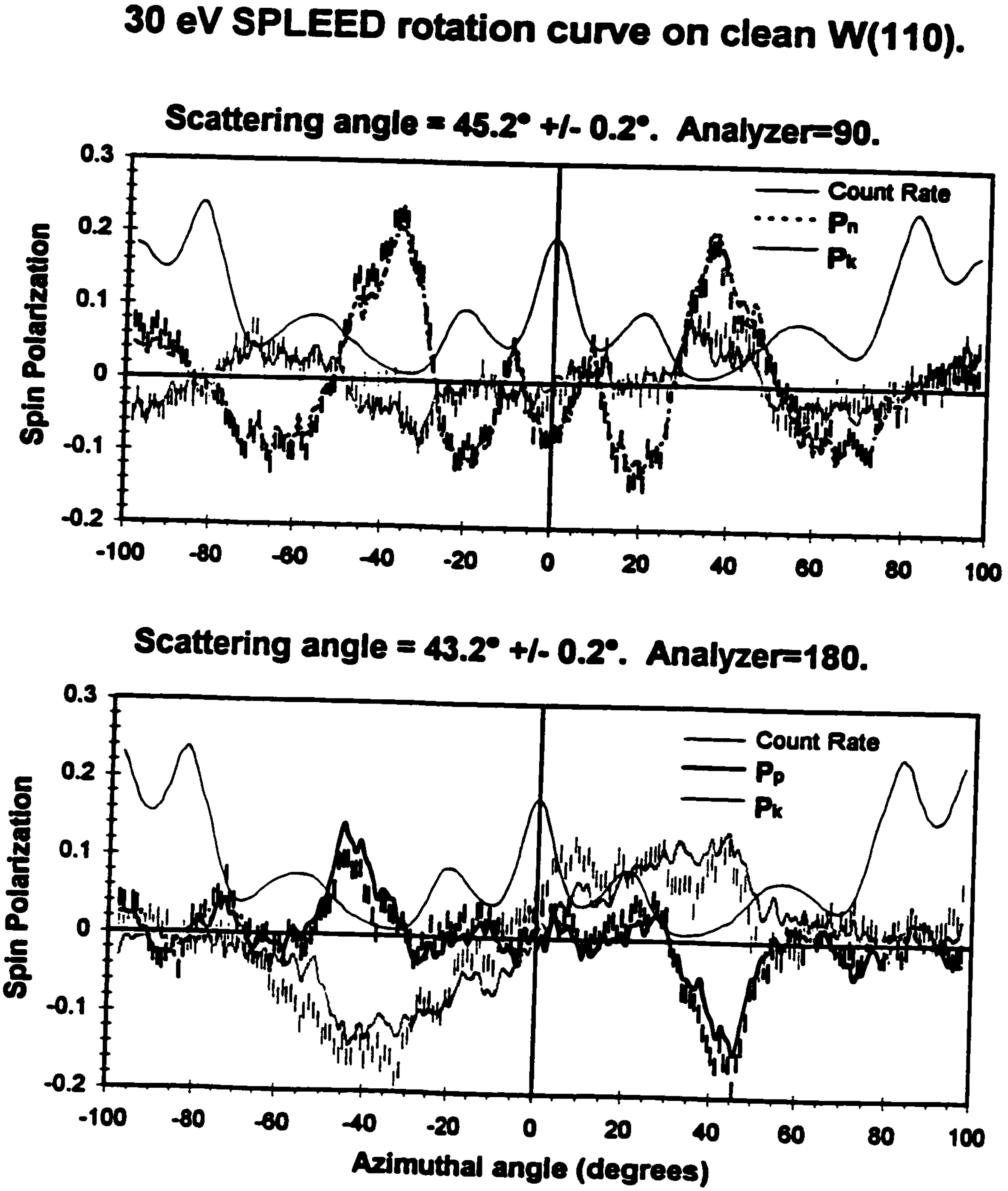

Figure 2-12
Intensity and spin polarisation data obtained from a 40 eV SPLEED rotation curve on a W(110) surface.

with the analyser rotated by 90°, so that the third polarisation component is now detected. All three components of spin polarisation could not have been measured with the original instrument. Note that the scattering angle has changed by 2° so that the components P_k measured in the top and bottom panels are not equivalent, although they are similar. The change in scattering angle was required for proper alignment of the spin polarimeter, and indicates that either the analyser apertures are no precisely aligned, or that the axis of rotation of the analyser is not precisely along the specularly scattered beam. Work is currently underway to correct this.

Secondary Electron Measurements

A series of secondary electron magnetometry measurements were made on Fe films grown on a W(100) substrate. This system was chosen because the magnetic properties had already been characterised in this laboratory using SPLEED techniques and were well understood.[26] Figure 2-13 shows the spin polarisation of 30 eV secondary electrons emitted from a 6 monolayer (ML) Fe film. The sample was illuminated with a beam of 200 eV electrons. Magnetic field pulses were applied parallel to the surface along the <110> direction. Between pulses, in zero magnetic field the transverse (along the <110> direction) components of spin polarisation were measured. The data shows that the Fe film is magnetic and that a 2.3 Oe magnetic field is required to reverse the direction of magnetisation.

Spin Polarised Electron Energy Loss Experiments

These measurements are a long term goal of the project. To date a spin polarised electron source, (essential to making these measurements) has not been available to test this mode. To ensure that the instrument is capable of obtaining electron energy loss spectra W plasmons were studied . The complete development of spin polarised electron energy loss experiments is left as a future project.

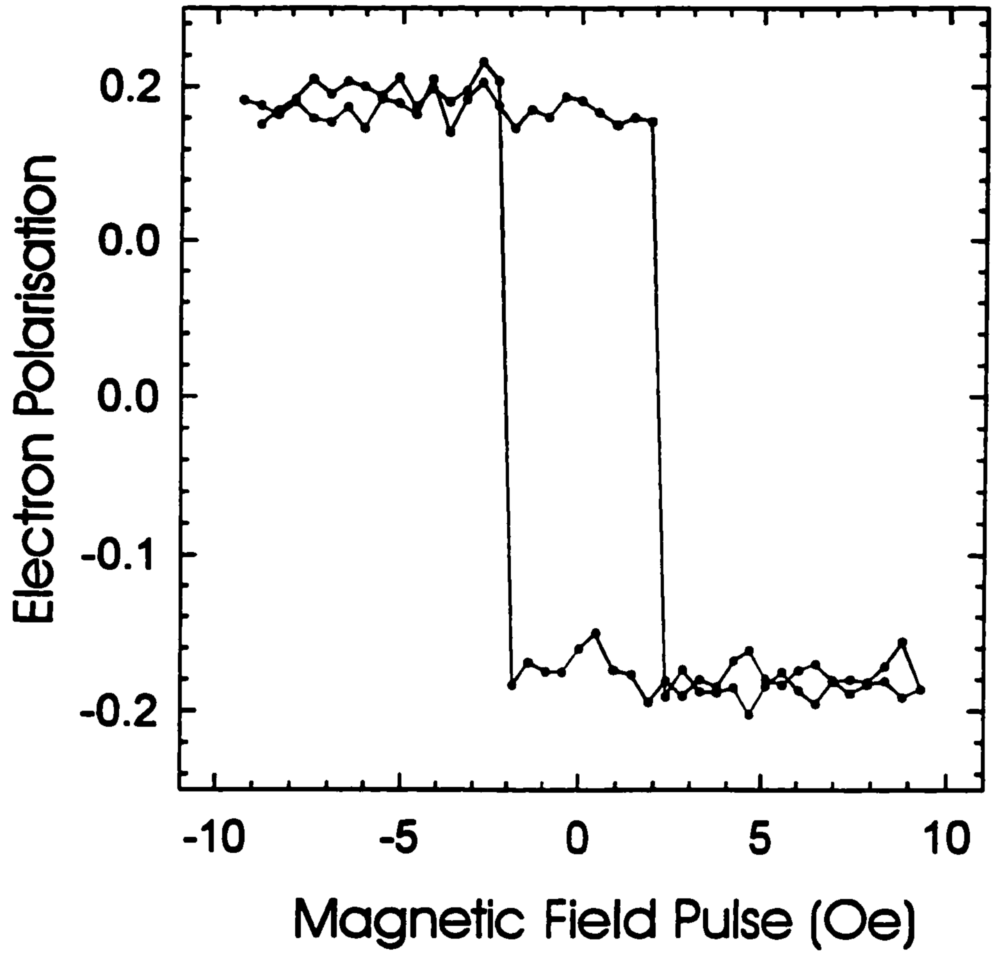

Figure 2-13
Secondary electron spin polarisation of 30 eV electrons emitted from a 6 monolayer Fe film. The substrate is W(100). The polarisation is plotted as a function of magnetic field pulse.

Figure 2-14 shows an electron energy loss spectra for the clean W (110) surface. A primary beam energy of 140 eV is used and the pass kinetic energy is 50 eV. The primary peak is seen at the far right, beginning to rise at about -4 eV. Two strong plasmons peaks are seen at -10.2 and -22.6 eV. These are identified as energy losses to surface and volume plasmons respectively in agreement with the work of Scheibner and Tharp.[40]

Auger Electron Measurements

Figure 2-15 shows two measurements of the series of W Auger electrons between 150 and 190 eV. The top spectrum is a measurement made with the instrument and the bottom spectrum is the same measurement made with a commercial retarding grid system. The data is presented in the customary differential mode. The Auger emission was induced with a beam of 2000 eV electrons and instrument parameters used to make this measurement were discussed earlier in this chapter.

Figure 2-16 shows a measurement of the 848 eV Ni Auger electron peak. The data was taken by illuminating a 3 ML film of Ni on W(110) with a beam of 2000 eV electrons. The energy analysis was done at a pass kinetic energy of 100 eV. The data is presented as electron intensity versus kinetic energy with the Auger peak at 5.9 ± 0.4 % of the background signal. This spectrum was taken in preparation for measuring the 848 eV Auger electron intensity as a function of emission angle. Angle resolved Auger emission spectroscopy is a powerful probe of the structure of the Ni film and will be discussed in great detail in the next chapter.

The Energy Resolution of the Instrument

In section 2.3 the energy resolution of the instrument was predicted to be:

$$\Delta K_{fwhm} = \left(0.048 + 0.0017\cdot\sqrt{\frac{V_1}{V_4}}\right)\cdot K_0 \qquad (28)$$

Where K_0 is the pass kinetic energy. The potentials V_1 and V_4 are a little more complicated to interpret. During the normal operation of the analyser:

$$V_1 \equiv |P_1| \qquad (29)$$

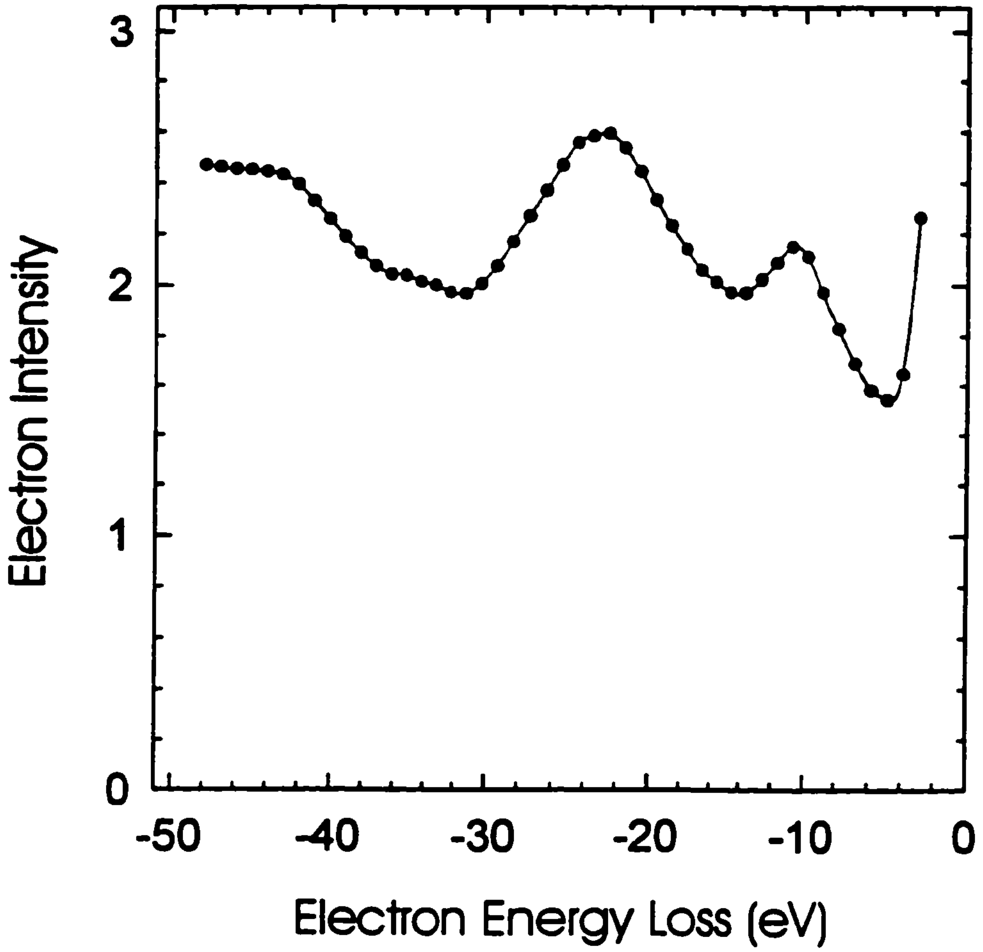

Figure 2-14
Electron energy loss spectrum for 140 eV electrons incident on a W(100) surface. The plasmon peaks discussed in the text are at -10.2 and -22.6 eV.

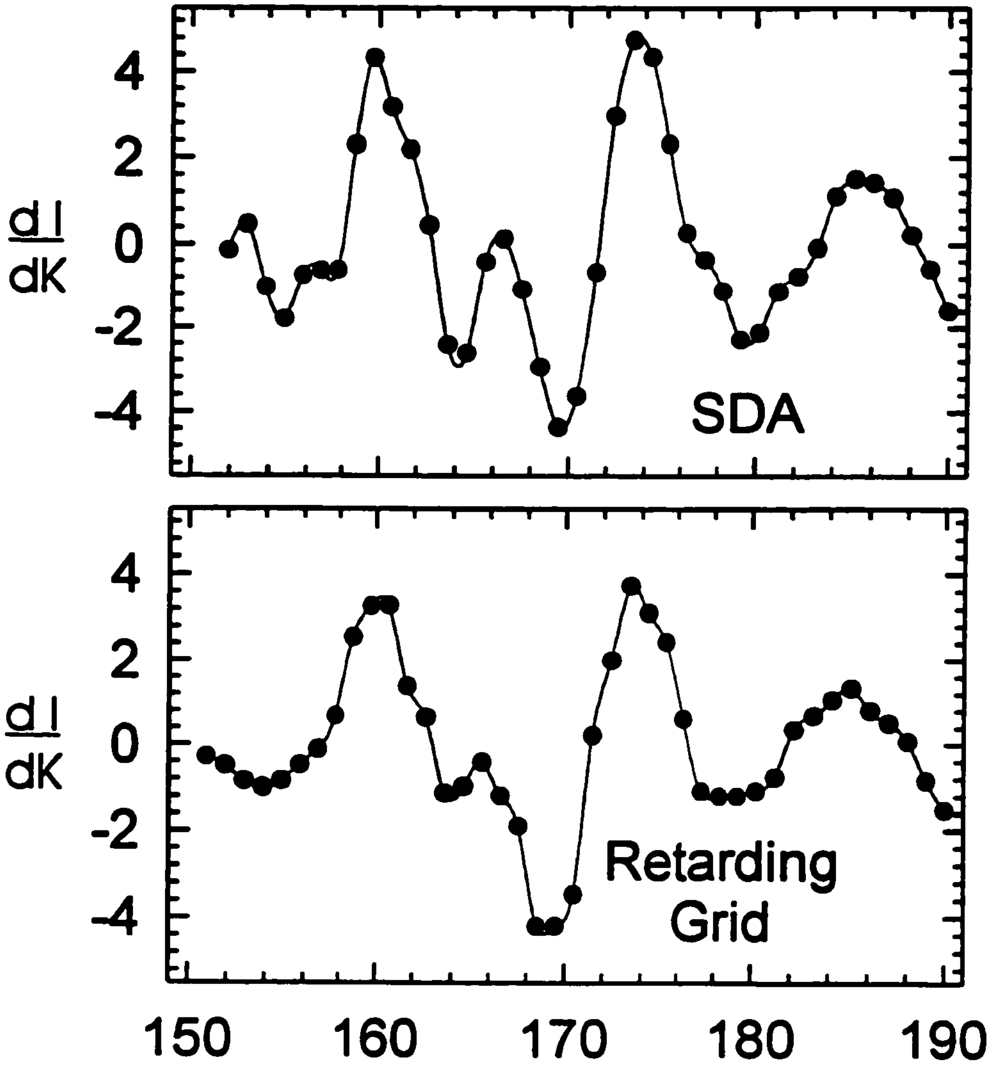

Electron Kinetic Energy (eV)

Figure 2-15
Auger electron spectra of a W(110) surface. The top plot shows data obtained with the SDA energy analyser. The bottom plot shows data obtained with a commercial retarding grid Auger electron spectrometer.

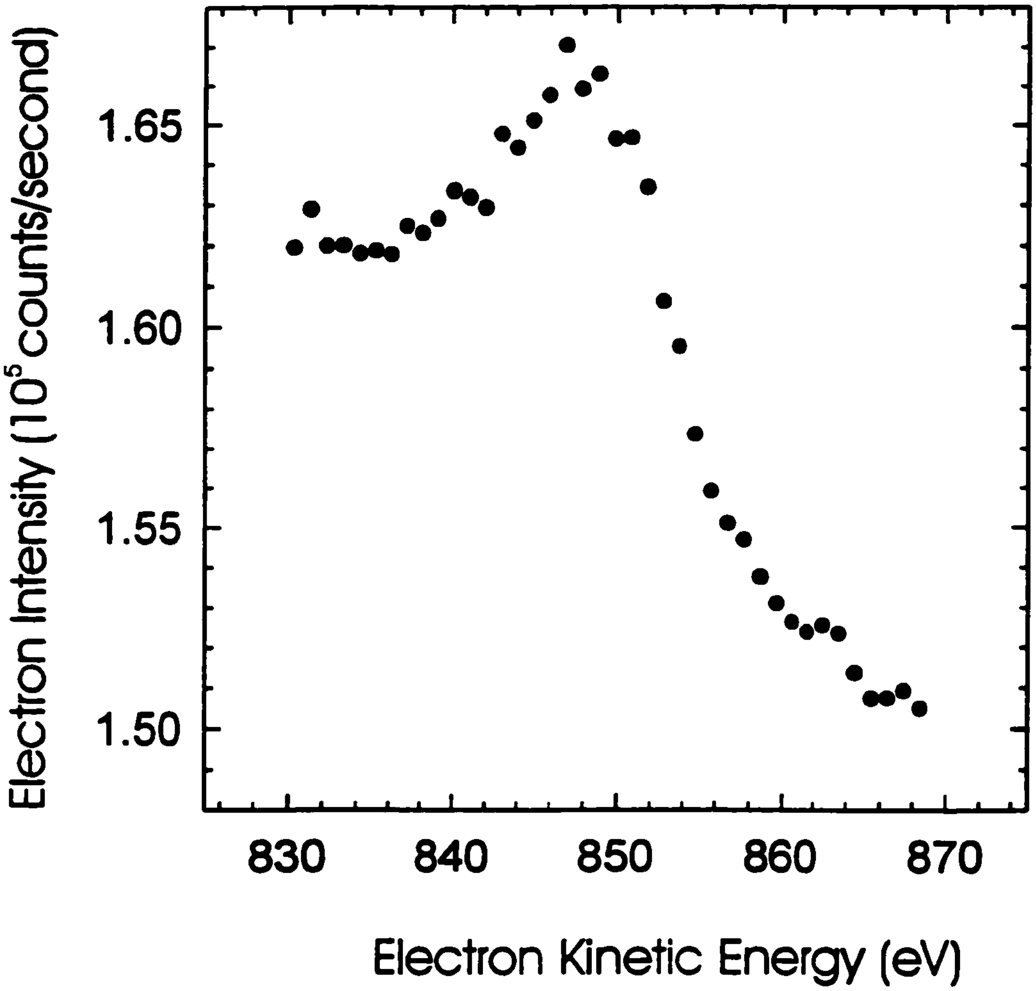

Figure 2-16
Secondary electron spectrum of 3 monolayers of Ni deposited on a W(110) substrate. The 848 eV Ni Auger electron peak is visible.

$$V_4 \equiv \text{PASS} \tag{30}$$

More precisely V_1 is the electric potential required to accelerate the electron from rest to the entrance kinetic energy and V_4 is the electric potential required to accelerate the electron from rest to the pass kinetic energy.

The energy resolution of the instrument was determined two ways, measuring the width of the elastic peak and the work function. In both of these measurements a natural energy width must be removed from the data to extract the energy resolution.

The Elastic Peak

When a beam of electrons interacts with a surface many of the electrons are reflected back into the vacuum with no change in kinetic energy. These electrons create a large elastic peak in the electron spectrum at the incident energy as shown in figure 2-2. The width of the peak is defined by the temperature of the filament of the electron gun. A typical elastic peak obtained by the instrument is shown in figure 2-17. To extract a peak position and full width at half maximum, a Gaussian distribution may be fit to the data.

If both the thermal spread of the electrons and the energy resolution are Gaussian and independent, the measured width of the elastic peak ΔK_{meas} is given by:

$$\Delta K^2_{meas} = \Delta K^2_T + \Delta K^2_A \tag{31}$$

Where ΔK_T is the thermal width and ΔK_A is the resolution of the analyser. ΔK_T should be independent of the pass kinetic energy and ΔK_A should be proportional to K_0. A plot of the square of ΔK_{meas} versus the square of K_0 should be a straight line with an intercept given by the square of ΔK_T.

Measurements for pass kinetic energies between 10 to 100 eV are shown at the top of figure 2-18. In this figure, the square of ΔK_{meas} is shown as a function of the square of K_0. The data at lower pass energies (circles) was obtained with an incident electron energy of 50 eV and the data at higher pass energies (squares) was obtained with an incident electron energy of 100 eV. Data was taken at these two energies to avoid large acceleration ratios.

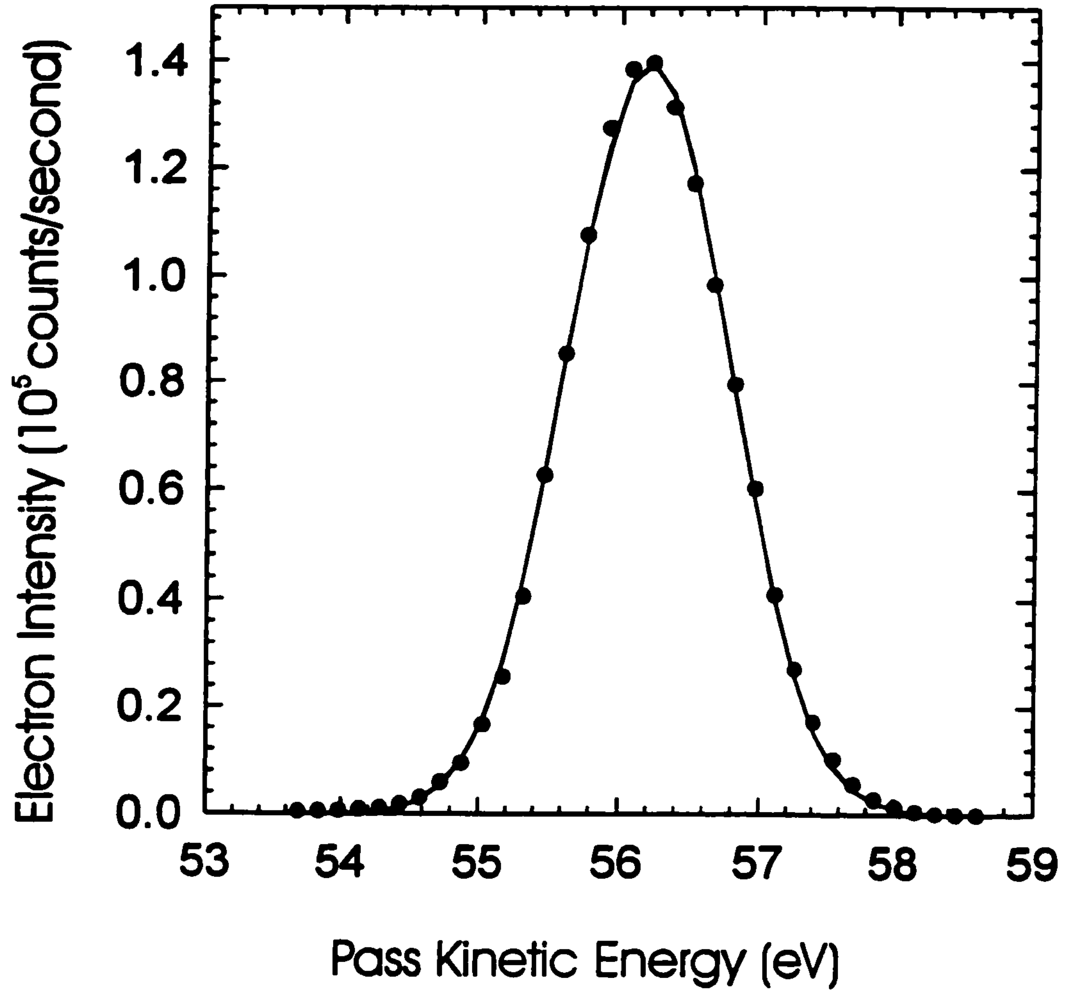

Figure 2-17
Electron kinetic energy spectrum showing the elastic scattering peak from 50 eV electons incident on a W(1 1 0) surface. The instrument was set to pass the 50 eV electrons at 56.2 eV. The circles are the data and the line is a Gaussian fit to the data.

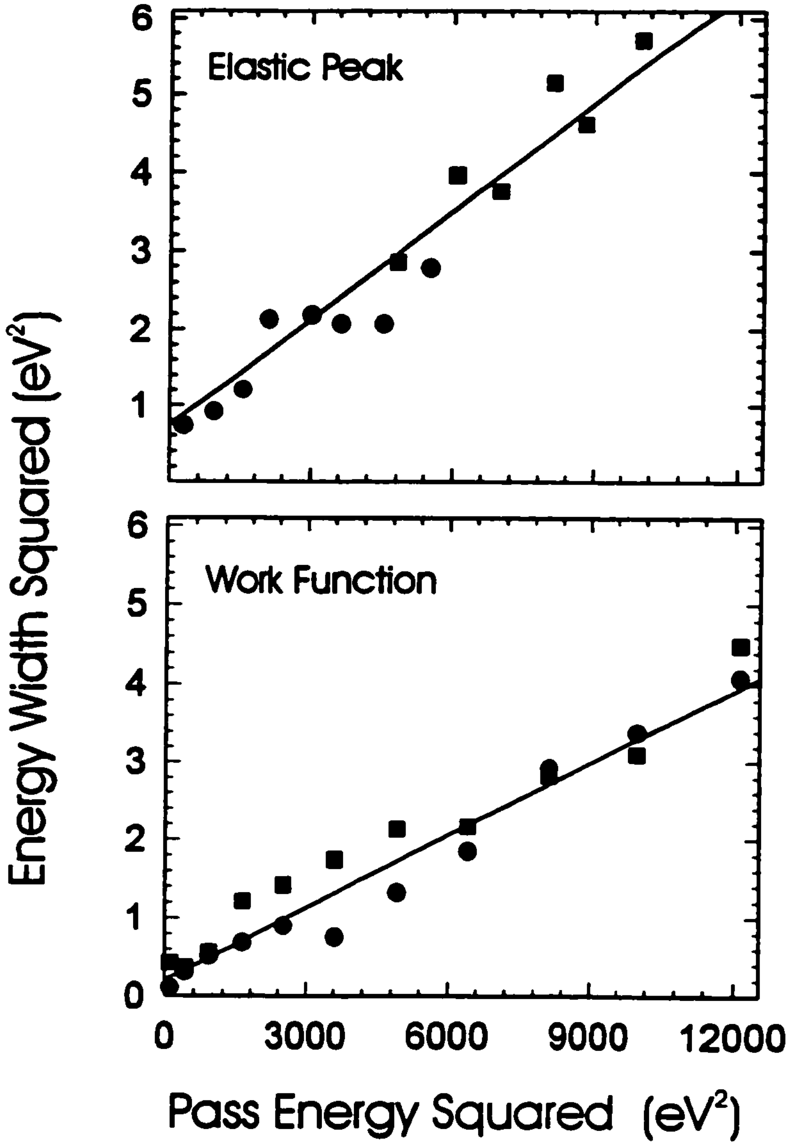

Figure 2-18

Determination of the energy resolution by plotting energy width squared versus pass energy squared. The top plot is of data extracted from elastic scattering peaks. The bottom plot is of data extacted from work function measurements as described in the text.

A linear regression was performed on the data and the following energy resolution and thermal broadening was obtained:

$$\frac{\Delta K_{fwhm}}{K_0} = 0.021 \pm 0.001 \qquad (32)$$

$$\Delta K_T = 0.8 \pm 0.2 \quad \mathrm{eV} \qquad (33)$$

The Work Function

The work function of a material is the kinetic energy required for an electron to pass through the surface, and emerge into the vacuum. A typical work function measurement obtained with the instrument is shown in figure 2-19, where it is clear that electrons with less than about 2.0 eV cannot escape from the surface The work function is dependant on the material, the crystalline orientation of the surface and the orientation of the electron momentum of the electron with respect to the surface.

To determine the energy resolution of the instrument, the width of the work function cut off was measured as a function of pass energy. To extract the FWHM it was assumed that the data is a step function resolved by a Gaussian. The electron intensity as a function of the pass kinetic energy is given by:

$$I(K) = \int_{-\infty}^{0} \frac{1}{\sqrt{2\pi}\sigma} \exp \frac{-\left(K_{work} - K\right)^2}{2\sigma^2} \, dK \qquad (34)$$

Where I(K), is the electron intensity at pass energy K, σ is the width of the Gaussian and K_{work} is the work function. If the energy axis is transformed such that K_{work} is at the origin, equation (34) may be written as in terms of the well known erf function:

$$I(K) = 1 - \mathrm{erf}\left(\frac{K}{\sigma}\right) \qquad (35)$$

The FWHM energy resolution is extracted from the work function by finding K at $I(K=0.5\sigma)$ and $I(K=\sigma)$. From tabulated values of the erf function I(0.5) = 0.31 and I(1) =

0.16 . Figure 2-19 shows the two K values at 0.5σ and σ. The FWHM is then extracted using the fact that for a Gaussian:

$$\Delta K_{\text{fwhm}} = 2.36\sigma \qquad (36)$$

The mean of the two ΔK measurements was taken as the FWHM value. For the data the deviation form a Gaussian can be measured as:

$$\frac{\overline{\left|\Delta K_{\text{fwhm}}(\sigma) - \Delta K_{\text{fwhm}}(0.5\sigma)\right|}}{\overline{\Delta K_{\text{fwhm}}}} = 0.02 \pm 0.01 \qquad (37)$$

and:

$$\Delta K_{\text{fwhm}}(\sigma) - \Delta K_{\text{fwhm}}(0.5\sigma) = -0.02 \pm 0.04 \ \text{eV} \qquad (38)$$

Equations (37) and (38) suggest that the work function is well represented by the model with small scatter in the two ΔK_{fwhm} values extracted from the data.

A plot of the mean fwhm value as a function of the pass kinetic energy is given at the bottom of figure 2-18. The data represented by circles was taken with an accelerating potential of -10 V on the sample crystal, and the data represented with squares was taken with an accelerating potential of -30 V. Fitting to a straight line gives:

$$\frac{\Delta K_{\text{fwhm}}}{K_0} = 0.018 \pm 0.001 \qquad (39)$$

$$\Delta K_T = 0.4 \pm 0.2 \ \text{eV} \qquad (40)$$

Discussion of the Energy Resolution

The first important feature of both the elastic and work function measurements is that the fwhm resolution is significantly smaller than that suggested by equation (28). In the derivation of equation (28), a triangular resolution function was assumed (the FWHM was taken as one half the base width of the triangle). Both figure 2-17 and the work function measurements strongly suggest that the resolution function is more like a Gaussian than a triangle. A Gaussian is more rectangular in shape and has a narrower

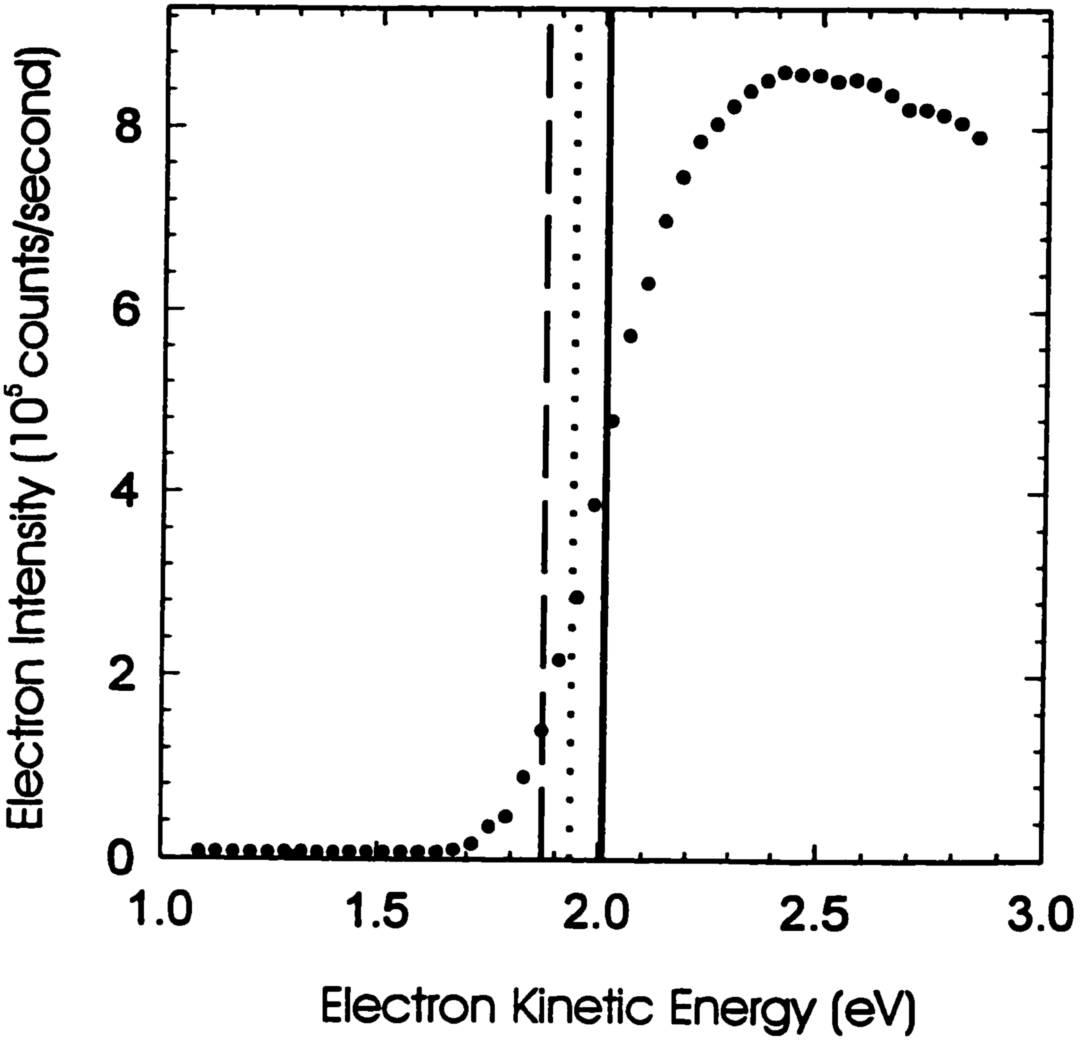

Figure 2-19
Electron kinetic energy spectrum showing the work function of the W(110) surface. The solid line is at the half-width of the cut off. The dotted line is at 0.5σ and the broken line is at σ as discussed in the text.

fwhm. This is likely the origin of the disagreement between the model and the measurements.

The elastic peak and work function fwhm parameters are close, but not within experimental uncertainty of each other. It is important to remember that the two measurements are very different in nature. In the work function measurement, electrons are emitted from the surface in all directions and the entrance aperture is used to define a beam of electrons for analysis. In the elastic measurement, a very well defined beam of electrons must be aligned with the entrance aperture and passed through the lens. This involves fine adjustment of the sample location and scattering angle and entrance lens deflectors. An initial geometrical or magnetic misalignment of the beam could be compensated with the deflectors. This might result in an beam which passes both input apertures, but is not parallel upon entering the SDA.

In equation (4) the fwhm parameter is linear in α_{in}, the angular deviation from a parallel beam at the SDA entrance. To account for the 0.003 difference between the fwhm parameters, a systematic 0.2° increase in the angular deviation of the elastic beam would be required. For example a misalignment of the beam between 0 and 0.4 during the elastic measurements would result in an increase of 0.003 in the fwhm parameter and an experimental uncertainty of 0.001. This gives a likely explanation for the difference in the fwhm measurements.

The thermal energy width at the electron gun filament is estimated to be about 0.75 eV, this agrees with the measured value for elastic data given by equation (33). For work function measurements, the intrinsic energy width given in equation (40) is much too large to be a room temperature energy width and is likely due to surface contamination on the W(110) crystal.

Conclusion

In general the instrument has shown that it meets all of the important design criteria. The energy resolution of the instrument is better than that originally estimated. At this point it was concluded that the instrument was sufficiently characterised to proceed with original experimental applications.

Chapter 3

The Growth and Structural Characterisation of Ultrathin Fe/Ni(111)/W(110) Films

Section 3.1

The Growth and Structure of Ultrathin Films

The most important task in an ultrathin film experiment is the characterisation of the structure and composition of the film. This may be done using a number of standard techniques which have been developed over the past 50 years. The optimum ultrathin film probe should only be sensitive to the film and the film interface and not sensitive to the bulk of the substrate. Low energy electrons have this property and are involved in most surface analysis techniques.

Low energy electrons are eminently suitable for the study of ultra thin films because they are sensitive to the structure of the surface. Electrons with kinetic energies around 100 eV have an attenuation length of 5 Å (~2 atomic layers in most metallic films). This means that most of the information carried in these electrons originates from the two top layers of the film.

Electrons of about 100 eV also have a de Broglie wavelength of about 1 Å, which is about the same distance as the separation between atoms in the film. When the wavelength of radiation is on the order of the lattice spacing in a crystalline solid, diffraction occurs and the resulting diffraction patterns and intensities give important structural information. LEED (low energy electron diffraction) is a well developed and sophisticated surface characterisation technique.[41] LEED analysis plays an important role in this thesis.

Other electron diffraction probes such as MEED and RHEED ('Medium' and 'reflection high' energy electron diffraction) are structural characterisation techniques which use higher energy electrons and are particularly suited for studying the growth of ultrathin films. These techniques were not used in this thesis.

Auger electron spectroscopy (AES) is another low energy electron probe which is perfectly suited for the study of ultrathin films. Auger electrons are emitted from atoms which have been excited with radiation (an electron or x-ray beam usually). Auger electrons are emitted at precise energies defined by three atomic energy levels and therefore each atom has a distinct Auger spectrum.

AES is particularly useful because the information is element specific so the composition of the surface may be analysed. Auger electrons have energies between about 30 and 1000 eV which corresponds to attenuation lengths between about 4 and 20 Å (~2 to 10 atomic layers). Therefore AES is a surface sensitive probe. AES was used extensively in this study and will be discussed in detail in chapters 3 and 4.

Other surface sensitive probes which use electrons include various electron microscopy techniques, work function measurements, photoemission and secondary electron spectroscopy. A good introduction to these techniques is presented by Modinos.[19]

Engineering the Crystalline Structure of Ultrathin Films

In many ultrathin films the crystalline structure of the film is determined by the structure of the substrate. This provides a unique opportunity to engineer materials with novel structures. This engineering is most successful with metals because metallic atoms tend to form very weak directional bonds in solids and therefore are more likely to adopt alternate crystal structures.

A classic example of this structural engineering is the growth of face centred cubic (fcc) Fe films on a Cu substrate. At room temperature Fe has a body centred cubic (bcc) crystal structure and undergoes a martensitic transition to a fcc structure above 1180 K. However, when ultrathin films of Fe are deposited on a fcc Cu substrate the Fe assumes a fcc or fcc-like structure for the first 3-20 layers at temperatures as low as 80 K. At greater thickness the film reverts to the bulk bcc structure. The thickness at which this occurs is highly dependent upon the cut of the Cu substrate crystal and the growth temperature.[18] Fcc Fe grows on the Cu substrate for several reasons, the most important being that the Fe and Cu atoms are both metals and are almost exactly the same size.

The term epitaxy is used to describe the growth of thin films and in particular the arrangement of the film atoms with respect to the substrate atoms (epitaxy means 'arrangement on'). There are several classes of epitaxy which are important in ultrathin metal films. One epitaxy which almost always occurs for very thin metallic films is pseudomorphism (pseuodmorph meaning 'false form'). Pseudomorphic films assume the crystal structure of the substrate and typically complete one to several atomic layers before strain forces the film to revert to the bulk structure. Examples of this are Fe and Ni grown on a bcc W(110) substrate. Ni completes one pseudomorphic bcc layer before reverting to a strained fcc structure. After several more layers the Ni reverts to the bulk fcc structure.[42] Fe is bcc in the bulk with a smaller crystal spacing than W. The first two layers of Fe on W(110) are pseudomorphic followed by a continuous contraction of the crystal spacing to the bulk Fe bcc structure.[43]

Another important aspect of epitaxy is the preferred orientational relationships which may occur between the film crystal lattice and the substrate crystal lattice.[44] In the case of Ni on W(110), the fcc Ni structure grows on the bcc W substrate in a well defined manner with the Ni fcc<011> lattice direction aligning with the W bcc<001> lattice direction. When Fe is grown on fcc(111) substrates similar orientational relationships occur once the Fe has reverted to the bcc structure. These relationships will be discussed in great detail in chapter 4.

Ultrathin Film Growth Modes

When atoms are adsorbed onto a flat crystalline substrate (with negligible diffusion into the substrate) three possible film growth modes are expected:[44] Layer-by-layer or Frank-van der Merwe (FM) growth occurs when the first atomic layer is completely finished before the second layer begins to grow; the second layer is completely finished before the third layer begins to grow and so on. Volmer-Weber (VW) , or island growth occurs when the atoms form three dimensional structures on the substrate. Stranski-Krastanov (SK) growth is an intermediate mode in which the growth begins as layer-by-layer, and after several atomic layers, island growth occurs.

Perfect FM growth is very rare because both entropy and random deposition favour three dimensional growth. FM growth is initiated by good wetting of the film on the substrate. After the completion of the first layer, near perfect FM growth would be expected if the growth face is the crystalline face with the lowest free energy.

For many metallic film/substrate systems SK is the most common growth mode. This mode occurs when the free energy of the film/substrate interface favours wetting, but away from the interface three dimensional growth occurs.

In the study of ultra-thin magnetic films, near layer-by-layer growth is desirable because this allows for precise determination of the film thickness and structure, both of these parameters being very important in defining the magnetic properties.

The free energy condition for the initiation of layer-by-layer growth is given by:[45]

$$(\sigma_f - \sigma_s) + \sigma_i + \sigma_e < 0 \qquad (1)$$

Where σ_f is the surface free energy density of the film, σ_s is the surface free energy density of the substrate, σ_i is the surface free energy density of the film/substrate interface, and σ_e is the strain free energy density.

Ultra-Thin Film Growth of Fe on Ni(111) and Cu(111): A Comparison

This work is concerned with the study of ultrathin fcc Fe(111) films. Others have studied the magnetic and structural properties of fcc Fe(111) grown on a Cu(111) substrate. Unfortunately, Cu has proven to be a poor choice of substrate for the growth of fcc Fe(111) as the Fe/Cu(111) system is plagued by strong interdiffusion between the Fe and Cu as well as three dimensional island growth.[18,46]

In Chapter 4 the motivation for studying the Fe/Ni(111)/W(110) system is discussed in the general context of magnetic and structural properties. In this section the nature of the Fe/Ni interface will be described in terms of surface free energies. Equation (1) will be evaluated using parameters for a fcc Fe film on both Ni(111) and Cu(111) substrates to show that the Fe/Ni(111) system is the better choice for fcc Fe growth.

In equation (1) the term $(\sigma_f - \sigma_s)$ is a measure of how much diffusion and/or three dimensional growth is expected at the film/substrate interface. If $\sigma_f < \sigma_s$ the film atoms are favoured to form the surface. If $\sigma_f > \sigma_s$ the substrate atoms are favoured to form the surface and the film atoms will either diffuse into the substrate or form three dimensional structures to maximise the substrate surface area. For Fe on Ni(111) and Cu(111):[47]

$(\sigma_f - \sigma_s)_{Fe\text{-}Ni} = -212 \text{ erg/cm}^2$

$(\sigma_f - \sigma_s)_{Fe\text{-}Cu} = 436 \text{ erg/cm}^2$

Therefore Ni is the better substrate with respect to this term. These values were calculated using experimentally measured polycrystalline surface energy densities. Energy densities for specific crystal orientations will differ, but the overall trend should be the same.

It is interesting to note that Ni is also a better choice of material for making layered 'superlattice' films where the deposited material alternates between Fe and Ni or Cu. For good superlattice growth σ_f and σ_s should have similar values. If σ_s is much larger than σ_f the substrate atoms (now also film atoms in alternate layers) would form three dimensional structures to try to minimise the surface free energy. Bauer and van der Merwe define the surface energy mismatch parameter:[48]

$$\Gamma_{fs} = 2\frac{|\sigma_f - \sigma_s|}{\sigma_f + \sigma_s} \qquad (2)$$

and suggest that for $\Gamma_{fs} \leq 0.5$ good superlattice growth should be expected. Using values provided by Bauer and van der Merwe:

$(\Gamma_{fs})_{Fe\text{-}Ni} = 0.217$

$(\Gamma_{fs})_{Fe\text{-}Cu} = 0.412$

Again, Ni is the better material with respect to this term.

The sign of the interface surface energy density σ_i can be deduced by considering the heat of mixing for a solution of Fe and Ni. The heat of mixing for bulk solutions is:[49]

$\Delta H_{Fe\text{-}Ni} = -6$ kJ/mol

$\Delta H_{Fe\text{-}Cu} = 60$ kJ/mol

An endothermic heat of mixing is unfavourable for good monolayer growth because it favours a minimisation of the Fe/Cu interface by islanding.[50] Thus for Fe/Cu, σ_i is expected to be positive. Conversely the exothermic $\Delta H_{Fe\text{-}Ni}$ should favour a maximisation of the Fe/Ni interface and thus good monolayer growth should occur, probably at the expense of some interdiffusion of Fe into the Ni substrate.

From bulk lattice parameters, the strain energy σ_e for the Fe/Ni system should be larger than that of the Fe/Cu system. For Fe/Cu the fcc Fe nearest neighbour distance is 2.0% larger than the bulk Ni nearest neighbour distance and 0.3% smaller than the bulk Cu nearest neighbour distance. However, in the Ni(111)/W(110) buffer the Ni film is inhomogeneously strained. This and the fact that the fcc phase of Fe is not the equilibrium phase at room temperature make the interpretation of the strain energy difficult.

From the above analysis is reasonable to conclude that Ni(111) is good candidate for the growth of near layer-by-layer fcc Fe(111) films. The only perceived problem being the exothermic heat of mixing for Ni and Fe which may lead to some diffusion of the Fe into the Ni substrate.

Section 3.2

Introduction to Auger Electron Spectroscopy for Ultrathin Film Structural Characterisation

This rest of this chapter is devoted to the development of two Auger electron spectroscopy techniques for the structural characterisation of ultra-thin films. The first technique uses Auger electron attenuation to determine the growth mode of ultrathin Fe films deposited on the Ni(111)/W(110) substrate. The second technique was made possible by the addition of the energy analyser and was implemented by the author.

Auger Electron Spectroscopy

Auger Electron Spectroscopy (AES) is an atomic spectroscopy concerned with the emission of orbital electrons from atoms in an excited state.[51] Radiation such as x-rays or an electron beam leaves the atom in a doubly excited state (two electrons are involved). This is followed by a radiationless transition to an ionised state and a free electron state. Because discrete atomic orbitals are involved, each element has a distinct Auger electron spectrum.

Auger electrons are a very powerful surface science tool because they provide element specific information about the surface. Occurring at energies between 30 and 2000 eV, Auger electrons also interact strongly with atoms at the surface, providing important structural information. In this chapter two AES structural probes will be discussed: AES intensity versus deposition time measurements, and angle resolved AES.

Section 3.3

AES Intensity Versus Deposition Time Measurements

This is a method of film growth analysis which is concerned with the change in attenuation of Auger electrons as the film is deposited.[44] The technique was first used in this laboratory by Trevor Jones, who employed rigourous statistical analysis to interpret the data.[52]

Auger spectra are taken as a function of deposition time as the film is grown. These spectra are measured using a commercial retarding grid Auger electron spectrometer. The spectrometer has a built in electron gun which supplies a 2000 eV electron beam to induce Auger emission. The electron beam evaporator used to perform the deposition has an integral flux monitor which assures a constant deposition rate.[25]

Auger spectra are taken at regular time intervals during the deposition. Figure 3-1 shows the intensity of 48 eV and 61 eV Auger electrons as a function of time. In this example Fe is being deposited on a Ni(111)/W(110) substrate. As the thickness of the Fe film increases, the Fe Auger signal increases and the Ni signal decreases.

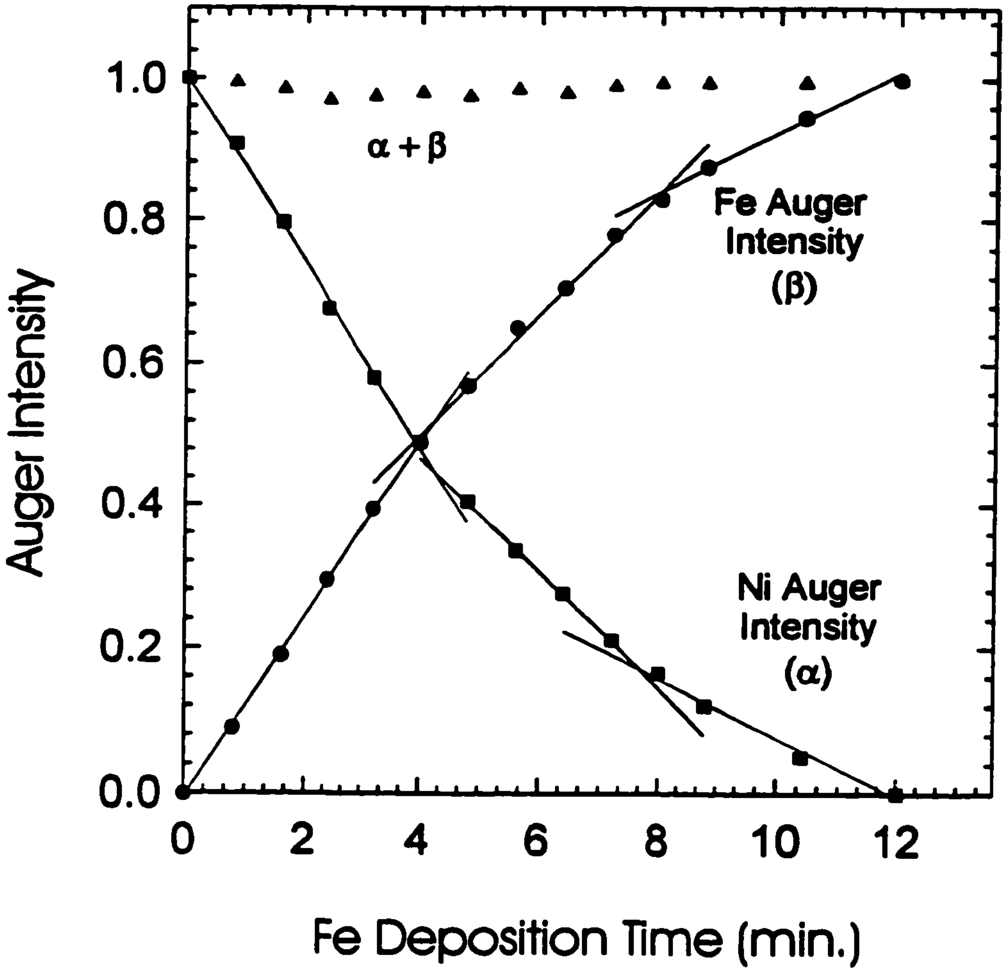

Figure 3-1
Auger electron intensity versus deposition data for the growth of Fe on a Ni(111)/W(110) substrate. Shown are the Fe 48 eV and Ni 61 eV Auger intensities. The linear segments are fitted to the data using the statistical analysis technique described in the text.

Film Growth Mode Analysis

In figure 3-1 the Ni Auger electron signal is attenuated by the Fe overlayer. The film growth mode may be determined by considering the nature of the attenuation curve. If the growth mode is perfect FM, the attenuation of the substrate by the first layer will be a linear function of the coverage:

$$\frac{A(\phi)}{A_0} = \phi\Omega + (1-\phi), \qquad 0 \le \phi \le 1 \tag{3}$$

Where $A(\phi)$ is the W Auger intensity at ϕ, the fraction of the substrate which is covered with the film material. A_0 is the Auger intensity at zero coverage and Ω is attenuation of the W Auger intensity by one atomic layer of material.

For the second and subsequent layers the attenuation is given by:

$$\frac{A(\phi_n, n)}{A_0} = \Omega^{n-1}\left[\phi_n\Omega + (1-\phi_n)\right] \qquad 0 \le \phi_n \le 1 \tag{4}$$

Where n refers to the layer. Equation (4) suggests that the W attenuation should be a linear function of deposition time during layer growth, with discontinuous changes in slope at the completion of the layers. The ratio of slopes for the n and (n+1) linear segments is given by:

$$\frac{M_{n+1}}{M_n} = \Omega = \exp\left(\frac{-d}{\Lambda}\right) \tag{5}$$

Where Ω may be expressed in terms of the thickness of the monolayer d, and the attenuation length Λ.

The signature of perfect FM growth is attenuation data which consists of equally spaced linear segments, where the ratios of the slopes of the successive segments are equal and are given by equation (5).

Extracting Auger Electron Intensities From the Data

Jones studied the growth of Fe on a W substrate by analysing the attenuation of W Auger electrons at energies between 150 and 170 eV.[52] This technique is not suitable for the study of the Fe/Ni(111)/W(110) system because the 2 ML Ni buffer already attenuates the W signal by a factor of 0.3. Therefore the slope of the first, second and third segment lines will be about 0.3, 0.2 and 0.1 of that measured by Jones (these estimates are based on attenuation of Auger electrons by Ni). These smaller slopes would be more difficult to resolve so an alternative method was devised.

Ni has an Auger electron at 61 eV and Fe has an Auger electron at 48 eV. The attenuation of the Ni Auger intensity and the build up of the Fe Auger intensity were both used to determine the growth mode of the Fe film. Figure 3-2 shows the Auger spectra for a Fe film grown on the Ni buffer at a 4.8 min deposition time. Also shown are the Auger spectra for the bare Ni buffer and for a 12 minute Fe film grown on the Ni buffer.

Although the Fe and Ni Auger peaks overlap, the respective signals can be extracted by using a least-squares fitting routine. The Auger spectra are fit to a linear combination of the bare Ni buffer spectrum and the 12 minute Fe spectrum. The following quantity was minimised for each deposition spectra.

$$\chi^2 = \sum_{K=35}^{70} \frac{\left[I_{data}(K) - \left(\alpha I_{Ni}(K) + \beta_{Fe} I(K) \right) \right]^2}{\sigma^2} \qquad (6)$$

Where $I_{data}(K)$ is an Auger spectrum taken during the deposition study, $I_{Ni}(K)$ and $I_{Fe}(K)$ are the basis function spectra for the Ni buffer and the 12 minute Fe Film, σ is the uncertainty in the data, and α and β are the fitting coefficients.The Ni and Fe Auger intensity coefficients (α and β) are shown in figure 3-1 as a function of Fe deposition time. The sum $\alpha + \beta$ was not constrained and is also shown in figure 3-1.

Determination of the Growth Mode

After the Auger intensities have been determined, the data are examined statistically to determine the growth mode. The data are subject to a least squares fitting procedure to several models. For attenuation data between 0 and 3 ML, two changes in slope (breakpoints) are expected at 1 and 2 ML. The models used in the fitting are; two

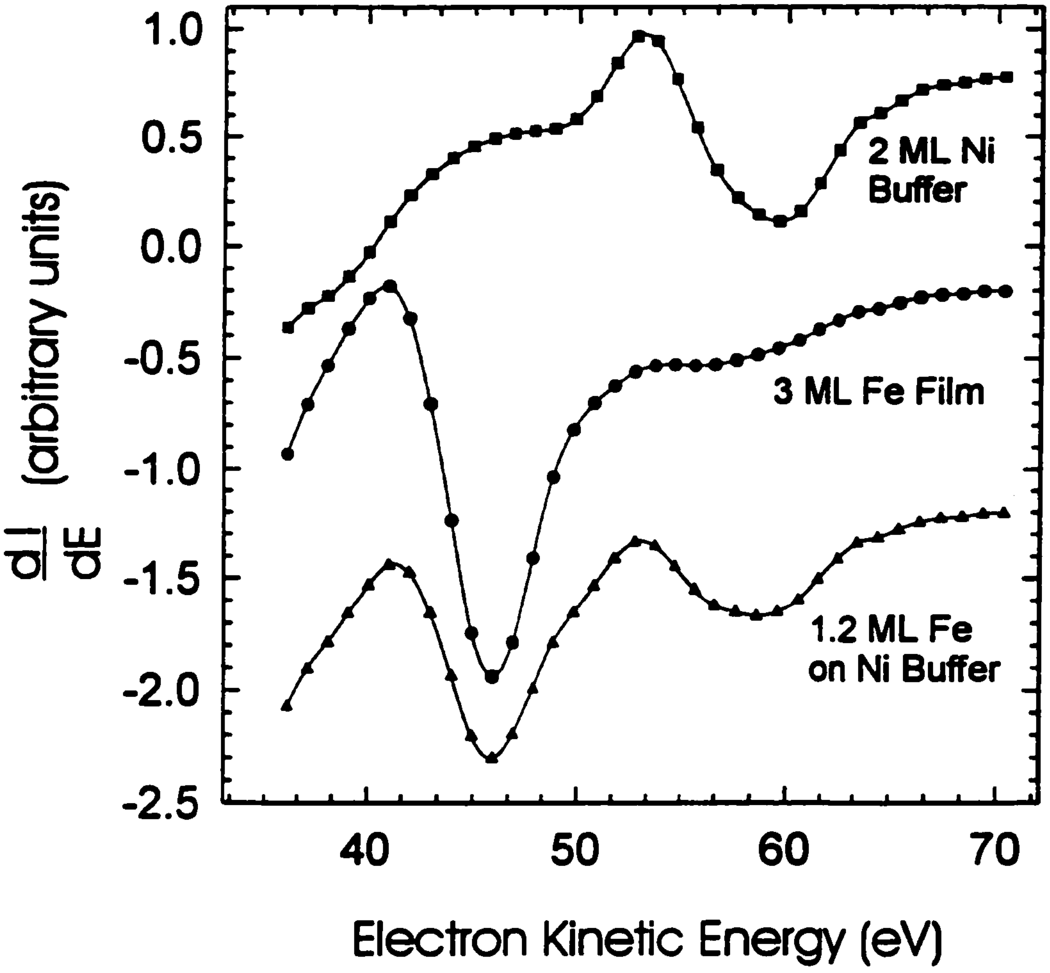

Figure 3-2
Auger electron spectra taken with a retarding grid electron energy analyser. The data are presented in the derivative mode and have been displaced on the vertical axis for clarity of presentation. Shown are spectra used to perform the Auger electron analysis discussed in the text.

linear segments, three linear segments and a decaying exponential. The free parameters in the linear fits are the slopes and intercepts of the lines and the position(s) of the breakpoint(s). For the decaying exponential the free parameters are the amplitude and decay constant.

The goodness of fit of these models was compared in a rigorous manner to decide which best describes the data. Because each model has a different number of degrees of freedom, great care must be taken in evaluating the goodness of fit.

The statistical 'f-test' is a method by which the goodness of fit for models with different degrees of freedom may be compared.[53]

$$f = \frac{\chi^2(\nu_a) - \chi^2(\nu_b)}{\chi^2(\nu_b)} \cdot \frac{\nu_b}{\nu_a - \nu_b}, \quad \nu_b \prec \nu_a \qquad (7)$$

Where $\chi^2(\nu_b)$ and $\chi^2(\nu_a)$ are the chi-squared values for models 'a' and 'b'. ν_b and ν_a are the degrees of freedom associated with the models. In general;

$$\nu_a = N - C_a \qquad (8)$$

where N is the number of data points and C_a is the number of parameters in the model. For the two linear segment, three linear segment and exponential fit respectively:

$C_2 = 5$, $C_3 = 7$, $C_{exp} = 2$

The 'f-test' answers the following question: Given a model with ν_a degrees of freedom, is the goodness of fit improved if a model with fewer degrees of freedom (ν_b) is used? Tabulated values of f are consulted to answer this question to within a degree of statistical certainty (i.e. to within 95% confidence the goodness of fit is improved etc.).

Two and three linear segments were fit to both sets of data and in both cases the three segment model was found to better describe the data with a confidence greater than 99%. A decaying exponential was also fit to the Ni data and the three segment model was found to better describe the data, again with a confidence greater than 99%.

The linear segments obtained in the fit are shown in figure 3-1, and the breakpoints are evident at the intersections of the linear segments. Both fitting procedures give similar breakpoint positions. For the Fe curve, breakpoints were found at $T_1 = 4.2$ min. and $T_2 = 8.0$ min. and for the Ni curve $T_1 = 4.3$ min. and $T_2 = 7.7$ min. The agreement between the analysis of the Fe and Ni curve and the fact that $\alpha + \beta \cong 1$ suggests that the linear combination model is reasonable.

This method was also used to determine the growth mode of Ni and Fe on W(110). These results are presented in the following chapter along with a discussion of the growth mode of the Fe/Ni(111)/W(110) films.

Section 3.4

Angle Resolved Auger Electron Spectroscopy (ARAES)

In this section, angle resolved Auger electron spectroscopy (ARAES) will be introduced as a structure sensitive AES. This is followed by a description of how the energy analyser is used to make ARAES measurements. Finally the interpretation of the ARAES data using a computer simulation program will be discussed. A complete ARAES study of the fcc to bcc structural transition in the Fe/Ni(111)/W(110) system will be presented in the next chapter.

Auger Electron Forward Focusing

In general Auger electron emission is directionally isotropic. However, if the Auger emitting atom is embedded in a crystalline lattice, the Auger electrons are focused along directions defined by the neighbouring atoms. This is a result of the scattering of the electrons by the positive atomic cores. The focusing effect is strongest when only one neighbouring atom is involved in the scattering process as multiple scattering tends to defocus the electrons.

If the emitting atoms are near the surface of a crystalline material, the scattering results in a forward focusing of the Auger electrons along directions defined by the crystal structure. A measurement of the Auger electron intensity as a function of angle gives important information about the structure and composition of the surface.[50]

Figure 3-3 shows an Auger emitting atom embedded in the second atomic layer of bcc(110) and fcc(111) surfaces. The direction normal to the plane of the page corresponds to the bcc<001> and fcc<011> directions respectively. For the bcc film Auger intensity enhancement is expected at ±45°, ±63° etc. For the fcc film the enhancement is expected at -19°,35°, 74°, -55°, -70° etc.

Structural Determination Using ARAES

As suggested in figure 3-3, the surface structure can be deduced from the ARAES peak positions. Figure 3-4 shows two typical ARAES measurements obtained with the energy analyser (the details of this measurement are described later in this section). The data is presented as Auger intensity as a function of emission angle. The data identified as Fe(110)/W(110) was obtained from a 2.5 ML Fe film deposited on W(110) using 702 eV Fe Auger electrons. The large peak at 45° suggests that the Fe film is bcc, in agreement with the observations of others.[43]

The data identified as Ni(111)/W(110) was obtained from a 2.0 ML Ni film deposited on W(110) using 848 eV Ni Auger electrons. The peaks at 35° and 55° suggests that the Ni film is multi-domained fcc, in agreement with the LEED pattern of the film and the observations of others.[42] The peaks at about 20° in both ARAES measurements are likely a combination of multiple scattering and diffraction effects which will be discussed later. In the Ni data there is also likely a contribution at 19° from regions of the film which have 3 ML coverage (see figure 3-3).

Growth Mode Determination Using ARAES

ARAES can also provide important quantitative information about the growth mode of a thin film. A perfectly flat 1 monolayer film of material 'f' on substrate 's' should not have any ARAES focusing peaks for the 'f' Auger electrons. If focusing peaks are seen, they indicate that some 'f' atoms are below other atoms. This could occur for

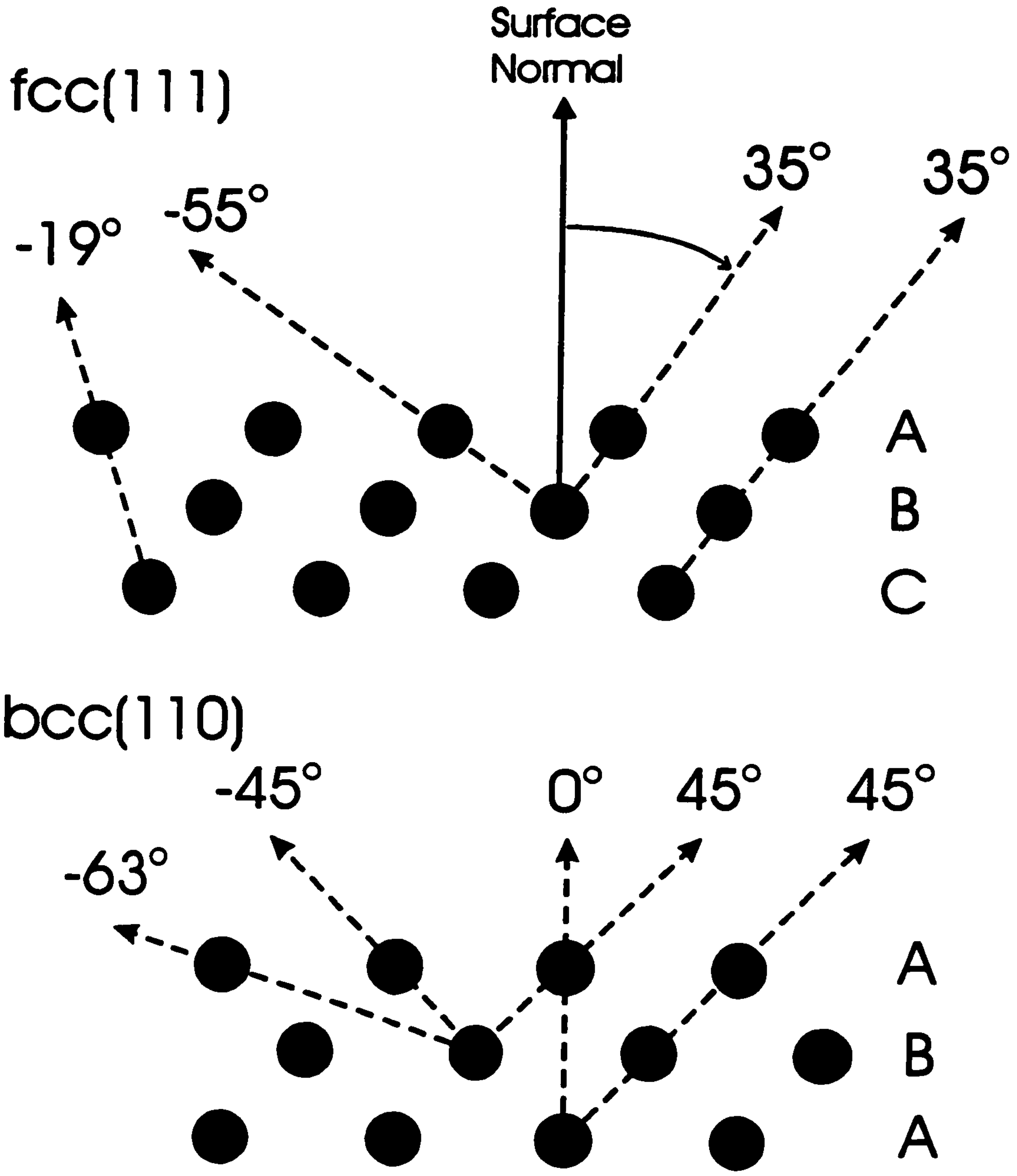

Figure 3-3
Schematic representation of ARAES focusing conditions at fcc(111) and bcc(110) surfaces. The top diagram shows the three layers A,B,C which constitute fcc stacking. The bottom diagram shows three layers of bcc stacking. The fcc<011> and bcc<001> directions are perpendicular to the plane of the page.

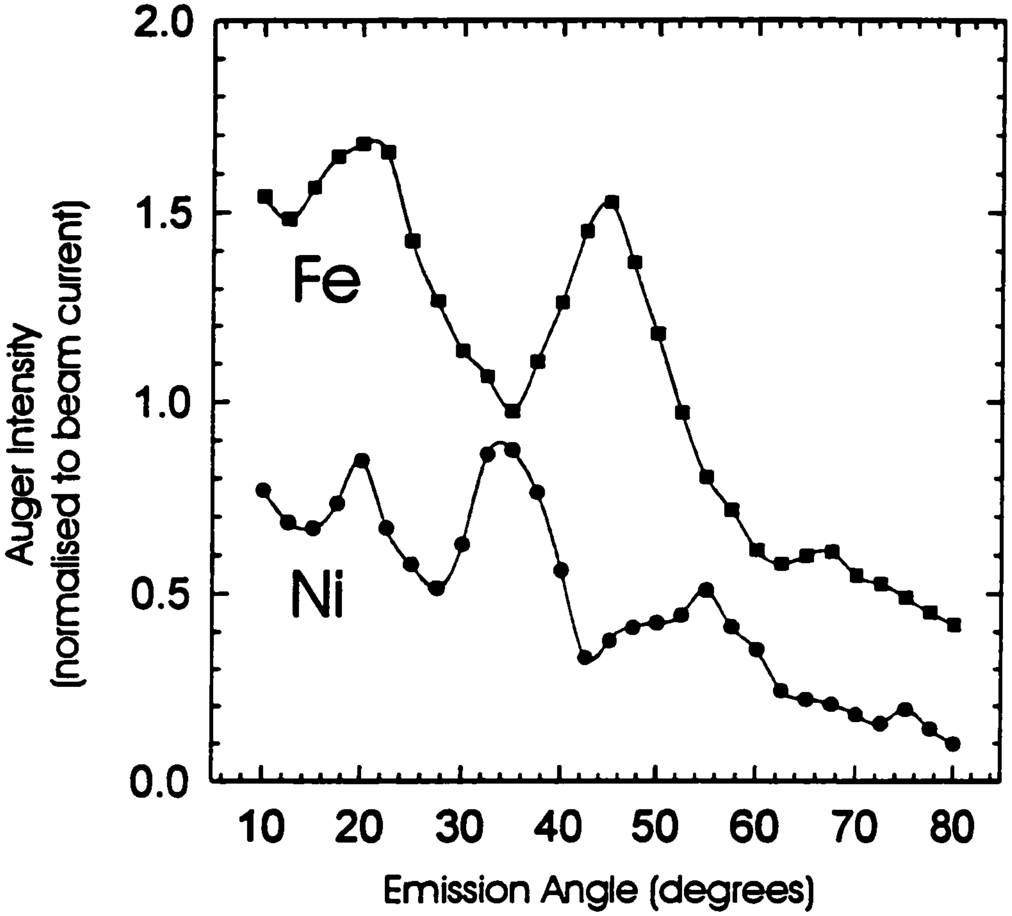

3-4
ARAES data for 2.5 ML Fe and 2.0 ML Ni deposited on a W(110) substrate. As discussed in the text, the data shows that the Fe film has a bcc structure and the Ni film has a fcc structure.

three reasons: 'f' is forming three dimensional islands on 's', 's' is not flat and has defects into which 'f' atoms have fallen and then are covered by subsequent deposition or, 'f' and 's' are intermixing to form an alloy.

The size of the ARAES effect is proportional to the number of covered 'a' atoms and this information may be extracted by comparing the data to computer simulations.[54] This technique will be discussed in greater detail later in this chapter.

Experimental Limitations of ARAES

ARAES is ideally suited for the study of films grown on a foreign substrate up to a thickness of 2 or 3 ML. For thicker films the ARAES data will still contain qualitative structural information in the peak positions but quantitative analysis of the growth mode is difficult because of the multiple scattering of the Auger electrons.

Figure 3-3 also shows focusing along chains of multiple atoms. Here, the first atom focuses the electrons but the subsequent atoms have a defocusing effect. The general result of this defocusing is that films thicker than about 3 ML show less ARAES structure than thinner films.[55] This is because electrons originating from deeper than 4 ML have been severely defocused, contributing more to the isotropic background than to the focusing peaks. The precise nature of this defocusing is complicated, being a strong function of the Auger electron energy and the atomic separation along the chains.[56]

Other multiple scattering effects and electron diffraction further complicate the ARAES structure, particularly for low energy Auger electrons.[50] Therefore ARAES measurements are usually performed with electrons with energies above about 400 eV.

The ARAES Measurement

ARAES data is collected by illuminating the sample with a 2000 eV beam of electrons to stimulate the emission of Auger electrons. The Auger electrons are analysed by the energy analyser and the spin analyser was used as an electron counter. The experimental arrangement is shown in figure 3-5. The angle between the incoming and

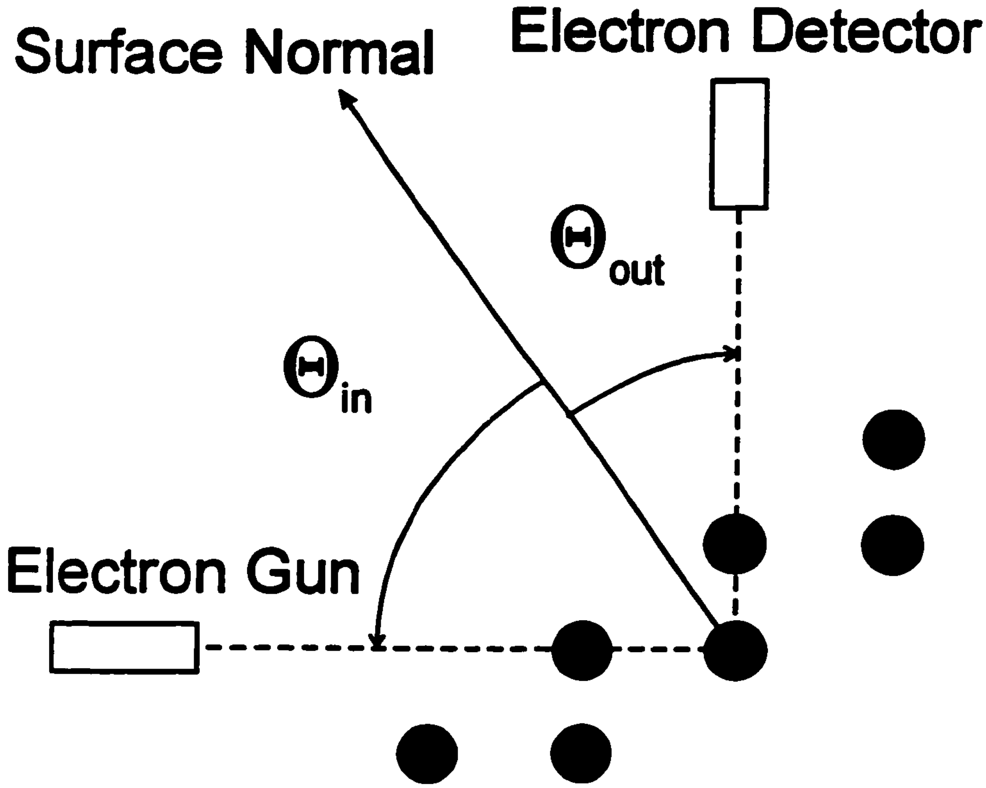

Figure 3-5
Shown is a schematic representation of the ARAES measurement. The angles associated with the incoming beam (Θ_{in}) and the outgoing beam (Θ_{out}) are shown.

detected electrons is fixed at 90° and the Auger electron intensity is measured as a function of the polar angle Θ by rocking the sample. The input lens of the electron energy analyser has a total angular acceptance of 3.6°. To ensure good angular resolution the Auger intensity was measured at 2.5° intervals for $10° \leq \Theta \leq 80°$.

Energy analysis is done at a pass kinetic energy of 100 eV with an energy resolution of about 2 eV. A typical energy spectrum for a 4 ML Fe film is shown in figure 3-6 with the Fe Auger electron peak at about 702 eV. Because we are only interested in the height of the Auger peak with respect to the secondary electron background it is not necessary to acquire an entire energy spectrum at each Θ. Instead, the electrons are counted at three energies (E_1 , E_2 and E_3). The signals E_1 and E_2 are used to extrapolate a background value at E_3. This background extrapolation is shown in figure 3-6 as the solid line through the data.

The Auger signal is extracted by subtracting the extrapolated background from the number of counts measured at E_3. This value (C_{aug} in figure 3-6) is then normalised to the beam current by dividing by the number of counts at E_2. Background extrapolation is important because quantitative analysis of ARAES data is only possible if all non-Auger effects are removed from the data.

The experimental data C_{aug} is in the form of Auger intensity normalised to the secondary electron background, which is a strong function of the emission angle Θ. The angular dependence of the background intensity (C_2 at E_2) is given in figure 3-7(a). The data comes from a number of ARAES experiments and is arbitrarily normalised. Over each experiment the 2000 eV electron intensity was kept constant to within a few percent. The solid line is the function B(Θ) a sixth order polynomial fit to the data.

This figure has the expected drop in intensity at higher angles but also has a broad peak at about 30°. The origin of this peak is not completely understood and may be the result of two geometrical effects. At low angles it is possible that the sample holder begins to obstruct the incident beam and the turnover is simply an aperture effect.

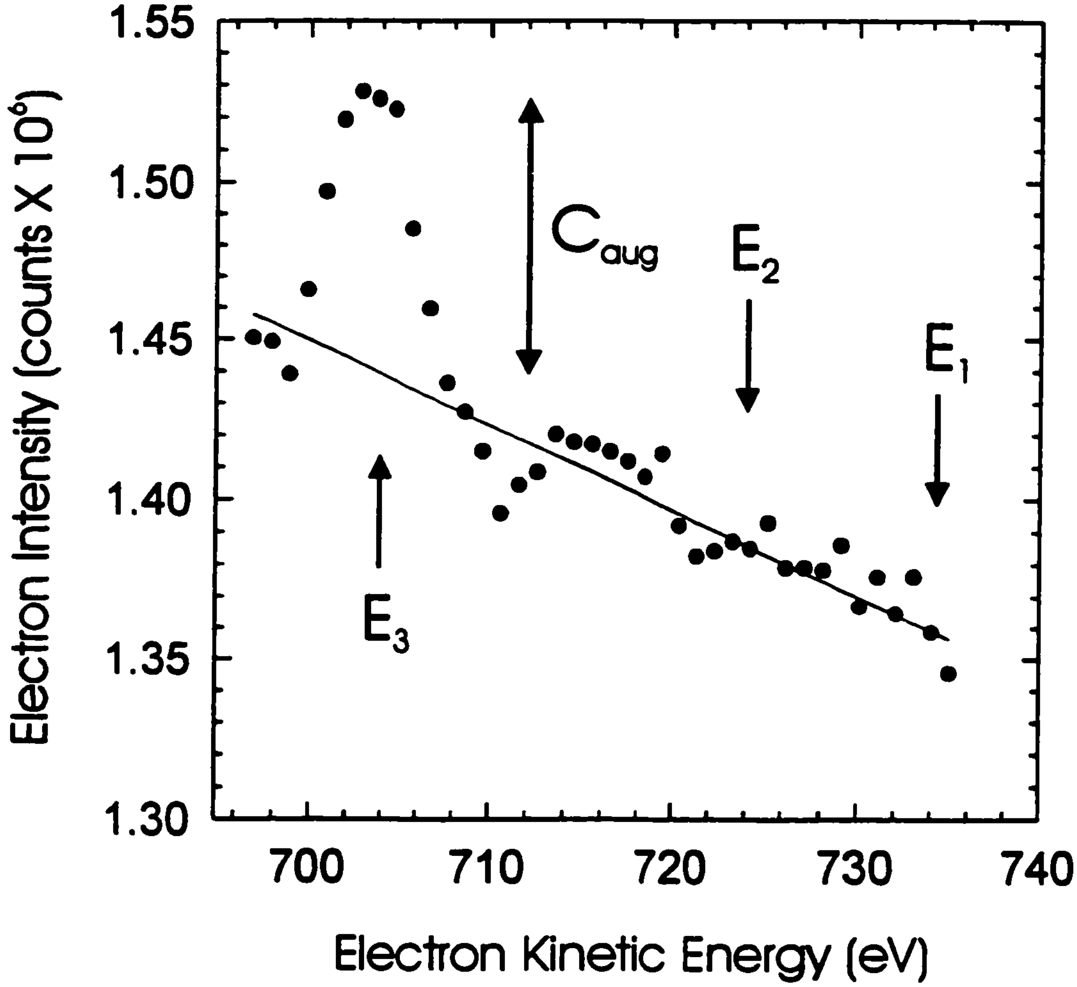

Figure 3-6
Electron kinetic energy spectrum of a 4 ML Fe film grown on the Ni(111)/W(110) substrate. The data shows the Fe Auger peak at 704 eV. The three energies used to perform the background subtraction discussed in the text are shown along with the Auger signal after background subtraction C_{aug}.

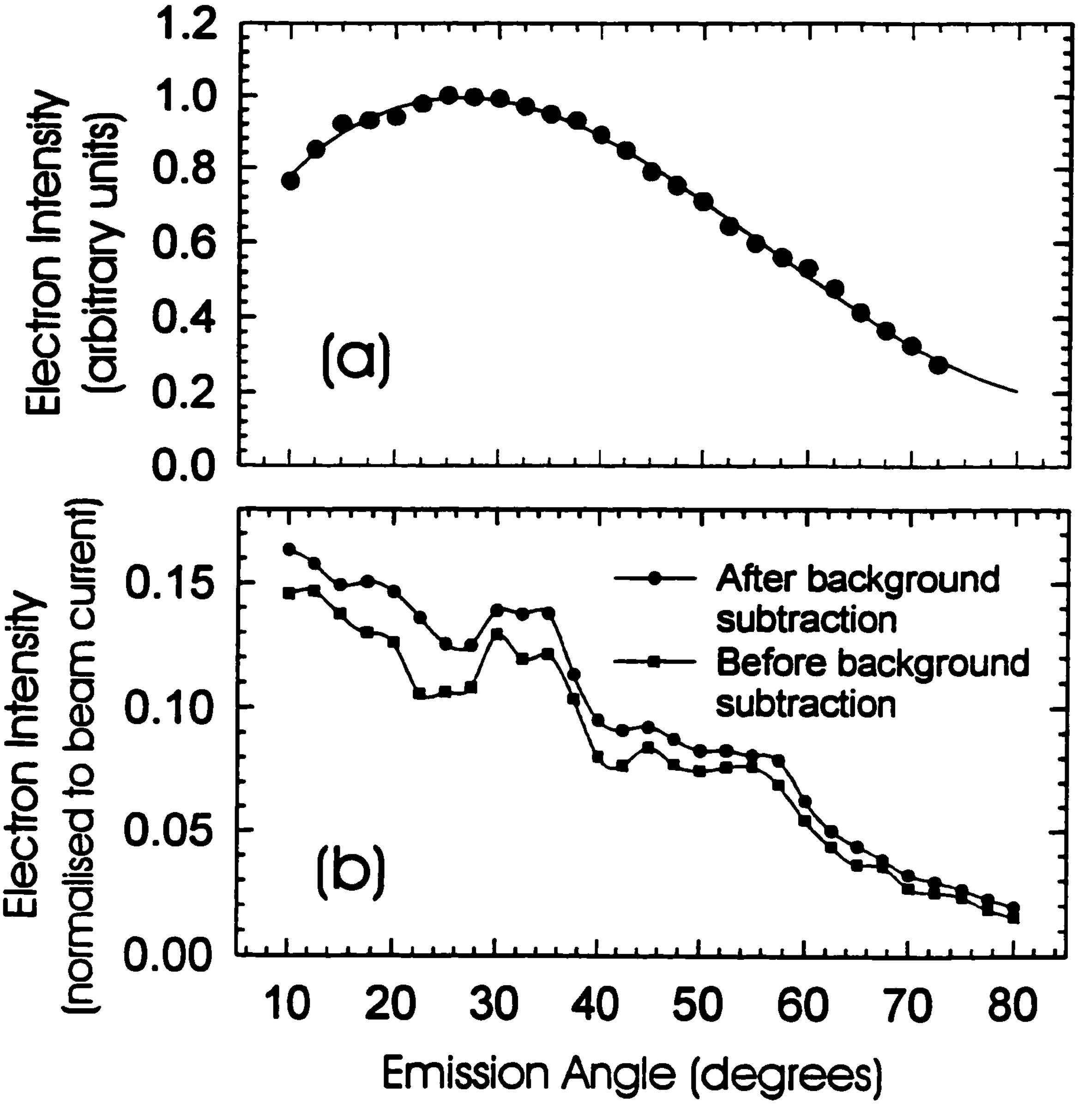

Figure 3-7

(a) Secondary electron intensity at 724 eV. The circles are the average of many measurements. The curve is a sixth order polynomial fit to the data.

(b) ARAES measurement of 4 ML Fe grown on the Ni(111)/W(110) substrate. The data before and after backgound subtraction is shown. The lines are guides for the eye.

Another explanation is that at low Θ values, the incident beam spot on the sample elongates and the energy deposited is spread out over a larger area. When this area becomes greater than the size of the entrance aperture the intensity of the detected electrons will drop.

This background function, $B(\Theta)$ is a measure of the background intensity per unit incident beam intensity. The ARAES data, $I_{data}(\Theta)$ is a measure of Auger intensity per unit background intensity and therefore the product:

$$I_{data}^{beam}(\Theta) = I_{data}(\Theta) \cdot B(\Theta) \tag{8}$$

gives the Auger intensity per unit incident beam intensity.

The difference between the three point extrapolated background subtraction and a two point measurement for a 4 ML Fe film is shown in figure 3-7(b). The data identified as 'before' is calculated as $(E_3 - E_2) / E_2$. The data identified as 'after' is calculated as C_{aug} / E_2. Both data sets have been normalised to the beam current using equation (8). The important difference between the two traces is the removal of the contribution of the slope in the secondary electron background.

Because the Auger signal is small with respect to the background (usually less than 10%) the measurements must be made with a constant current from the electron gun. Unfortunately the electron gun is unable to provide a constant current and tends to drift 5 to 10 % on a time scale of several minutes, the time interval required to measure the three points. Even if the current is constantly corrected by hand, effects of the drift are seen in the data.

To make accurate measurements possible, data was taken at a higher frequency to minimise the effect of gun drift. The instrument was cycled through about 60 read cycles where electrons were counted for about one second at each of the three energies. The total dead time per cycle required to change the pass energy was about 2.5 s giving a total time per cycle of about 5.5 s. This acquisition frequency was found to sufficiently limit the effect of the electron gun drift.

Experimental Uncertainties and Systematic Errors

One of the end uses of ARAES data is a comparison to computer simulations to determine the growth mode. To make a meaningful comparison, a complete understanding of all the experimental uncertainties and error is required.

The ARAES measurement is a counting experiment, where the number of electrons as a function of energy and angle is counted. The counting time is set to obtain about 10^6 counts at each energy. Applying counting statistics, an absolute uncertainty of about ± 0.3 % (normalised to input beam current) is estimated for the normalised ARAES signal after the background correction has been performed. The experimental variation in the data was determined by periodically returning to several chosen angles during data accumulation and repeating the measurement. This data suggests an upper limit in the uncertainty of ± 0.5 %, slightly larger than the error estimated from counting statistics but not unreasonable.

When an ARAES data point is obtained, the following tune-up algorithm is followed; the angle Θ is set and then the X and Y translation stages of the sample holder are adjusted to maximise the throughput. This adjustment is required because the centre of rotation of the sample holder does not lie along the centre of the 'good spot' on the sample. The Y value is adjusted over a range of about 5 mm over the course of an ARAES measurement in an effort to keep the electron beam on the same spot on the sample. Several systematic errors are possible during this measurement. For example, it is possible that as the measurement was made the electron beam wandered over the sample, although much effort was made to avoid this.

Another potential problem is an error in the angle Θ brought about by misalignment. The tune-up algorithm would be an acceptable way to proceed if the ARAES spectrum was flat. However, if the ARAES spectrum has strong peaks and valleys a problem arises. Suppose there is a minimum in the ARAES spectrum at 38° and a maximum at 35°. It is possible that when adjusting Y to maximise the throughput at 38°, a larger value of Y will be chosen because this would make the scattering angle closer to 35° and a larger signal would be obtained. This systematic error would tend to broaden the maxima and 'fill in' the minima in the ARAES data.

The distance between the sample and the input aperture is 100 mm. A three degree change in the ARAES angle would require a movement of 5mm in the Y direction. Although efforts were made to adjust Y in a systematic manner, an error of 5 mm is possible given the tune up algorithm which is biased towards the maximisation of the signal. The rate of change of Y goes as the cotangent of Θ and thus most of the translational correction was done at low angles (particularly below 20° where the rate of change is very large). At angles above about 50 degrees very little adjustment of Y was required.

Despite these experimental problems, the ARAES data appears to be reproduceable and well behaved.

Fitting Computer Simulations to the ARAES Data

The SSC Computer Simulation

To understand the growth mode of the FCC Fe monolayer, ARAES data were compared to computer simulations. The computer simulations were generated using the computer program ("SSC") originally developed by Friedman and Fadley for the purpose of calculating single scattering photo-electron diffraction for a cluster of atoms.[57] The program is provided with the spatial coordinates of a FCC cluster of atoms. One atom is chosen to be the emitter of a electron s-wave and the single scattering effects of all the other atoms in the cluster are calculated. To perform the calculation, material specific atomic scattering phase shifts are required at the Auger electron energy. These phase shifts were generated using a computer program developed by Rehr and co-workers.[58]

The output of the SSC program is the intensity of the scattered s-wave at infinity as a function of the polar and azimuthal angles. To simulate the ARAES measurements the azimuthal angle was set so the variation of the polar angle corresponds to rocking the sample about the fcc<011> direction as done in the laboratory. The program is also supplied with the attenuation length for the Auger electrons in the material and parameters to simulate the effect of a finite temperature on the peaks (Debye-Waller effect).

Because of the geometry of the experimental apparatus (both the electron gun and electron detector are fixed in the plane of the sample rotation) we must consider the effects of inward focusing of the 2000 eV electron beam which is used to stimulate Auger emission.[59] Figure 3-5 shows the experimental apparatus at an emission angle of 35°, where strong outgoing focusing is expected. At this angle the incoming beam should also be focused towards the emitting atom, resulting in greater Auger stimulation. Therefore the increased Auger intensity observed at 35° is a result of both incoming and outgoing effects.

The nature of the incoming focusing can be understood by applying a time reversal argument to the outgoing electron wave. The SCC program begins with a spherical wave at a lattice site and calculates the intensity of that wave in a solid angle at infinity after single scattering from all atoms in the cluster. This intensity can be interpreted as the probability that an emitted electron will be detected in a given solid angle. In the time reversal of this process the intensity may be interpreted as the probability that an electron incident at that solid angle will be focused to the emitting site.[60]

To correct for incoming focusing effects, the following scheme was followed.
(i) SSC was used to generate simulations for 2000 eV electrons and 702 eV electrons.
(ii) The polar angle for the incoming simulation was transformed to the complementary angle ($\Theta_c = 90 - \Theta$) and the simulations were multiplied together. To simulate the presence of both ABCA and ACBA FCC domains, the intensity data is then added to intensity data where the polar angle has been transformed by $\Theta_{ACBA} = 180^\circ - \Theta_{ABCA}$.

Figure 3-8 shows the SSC simulation for an emitter in the second layer of a 4 ML cluster of FCC Fe. Both the outgoing (702 eV) and the incoming (2000 eV) simulations are shown. Both simulations are similar, showing the expected focusing peaks at 35° and -55° degrees.

In the ARAES measurements the emission angle Θ is varied between 10° and 80° and peaks at both 35° and 55° are seen. This can be seen clearly in the ARAES data for 2 ML Ni on W(110) (figure 3-4) and 2 and 3 ML Fe on Ni(111) (chapter 4, figure 5). The presence of both peaks suggests that the film is multi-domained, with both ABCA and ACBA stacking domains present. This interpretation also agrees with the low energy electron diffraction (LEED) patterns of these films as discussed in chapter 4.

For the outgoing 702 eV simulation the 0 to 90° region will be defined as the AB stacking domain and the -90° to 0 region the AC stacking domain. For the incoming 2000 eV beam the complementary angle Θc must be considered in the proper geometry. For the AB stacking domain the 2000 eV region from -90° to 0 is transformed by Θc = Θ + 90°.

Figure 3-9 shows the outgoing 702 eV and the incoming 2000 eV simulations for the AB domain. For the AC stacking domain the 2000 eV region from 0 to 90° the transformation is Θc = Θ - 90°. This is also shown in figure 3-9. In these spectra the enhancement from the incoming beam is clearly seen, with the outgoing 702 eV focussing peaks at 35° and 55° enhanced by an 2000 eV incoming focusing condition.

The next step in the manipulation is to multiply the incoming and outgoing simulations together for each domain. The AB and AC products are shown in figure 3-10(a). The Θ axis for the AC domain has been transformed by 180°. These spectra now correspond to the expected contribution to the 702 eV auger electron yield from Fe electrons in the second layer in a fcc(111) film with AB or AC stacking. If it is assumed that the AB and AC domains are about equal in number, the contribution from the second layer is the mean of the two, shown in figure 3-10(b).

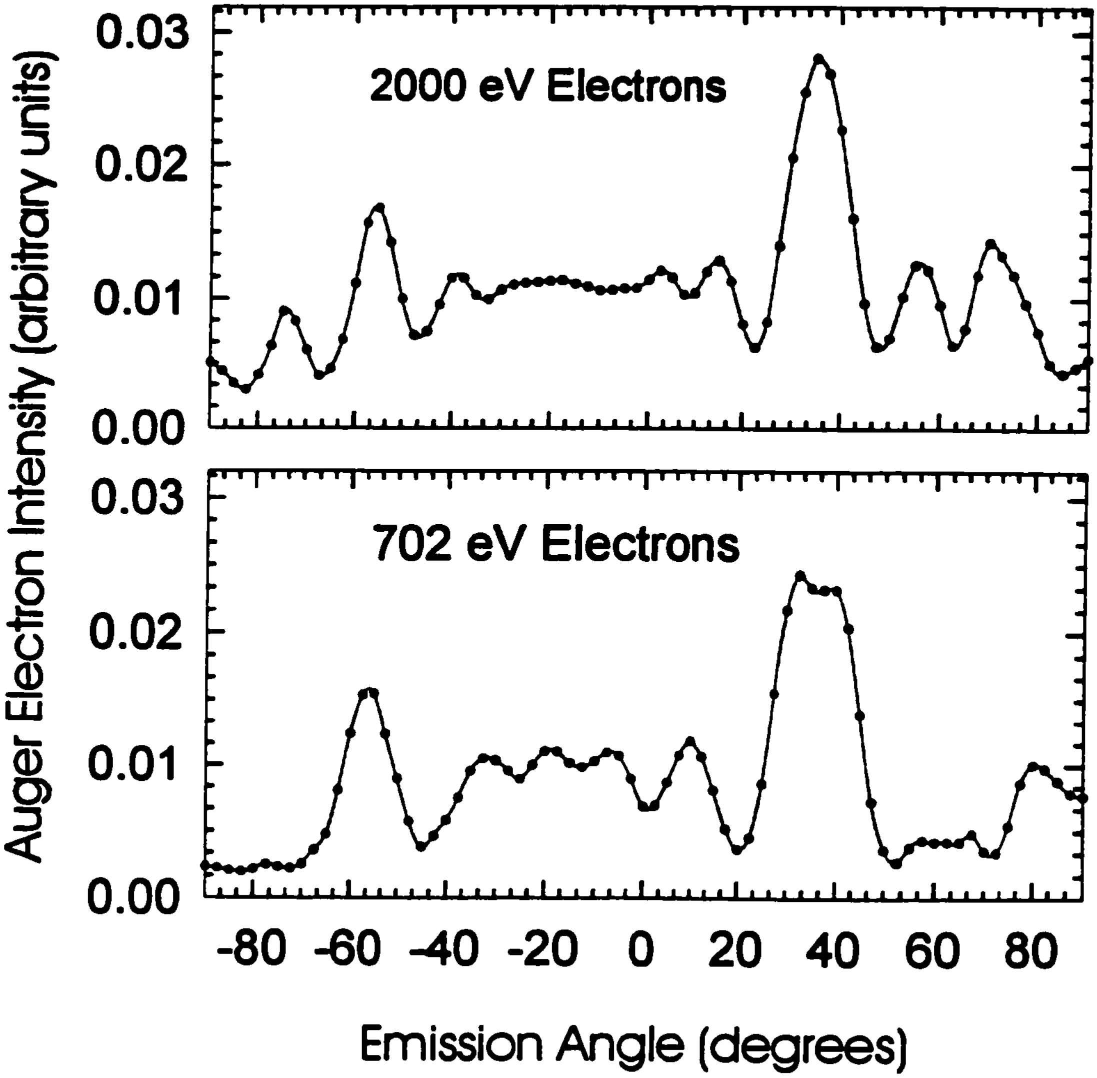

Figure 3-8
SSC simulations for 2000 eV and 702 eV Auger electrons. In both simulations a 4 ML thick fcc cluster is used and the electron emitter is in the second monolayer as described in the text. The ARAES focussing peaks at 35° and -55° are evident.

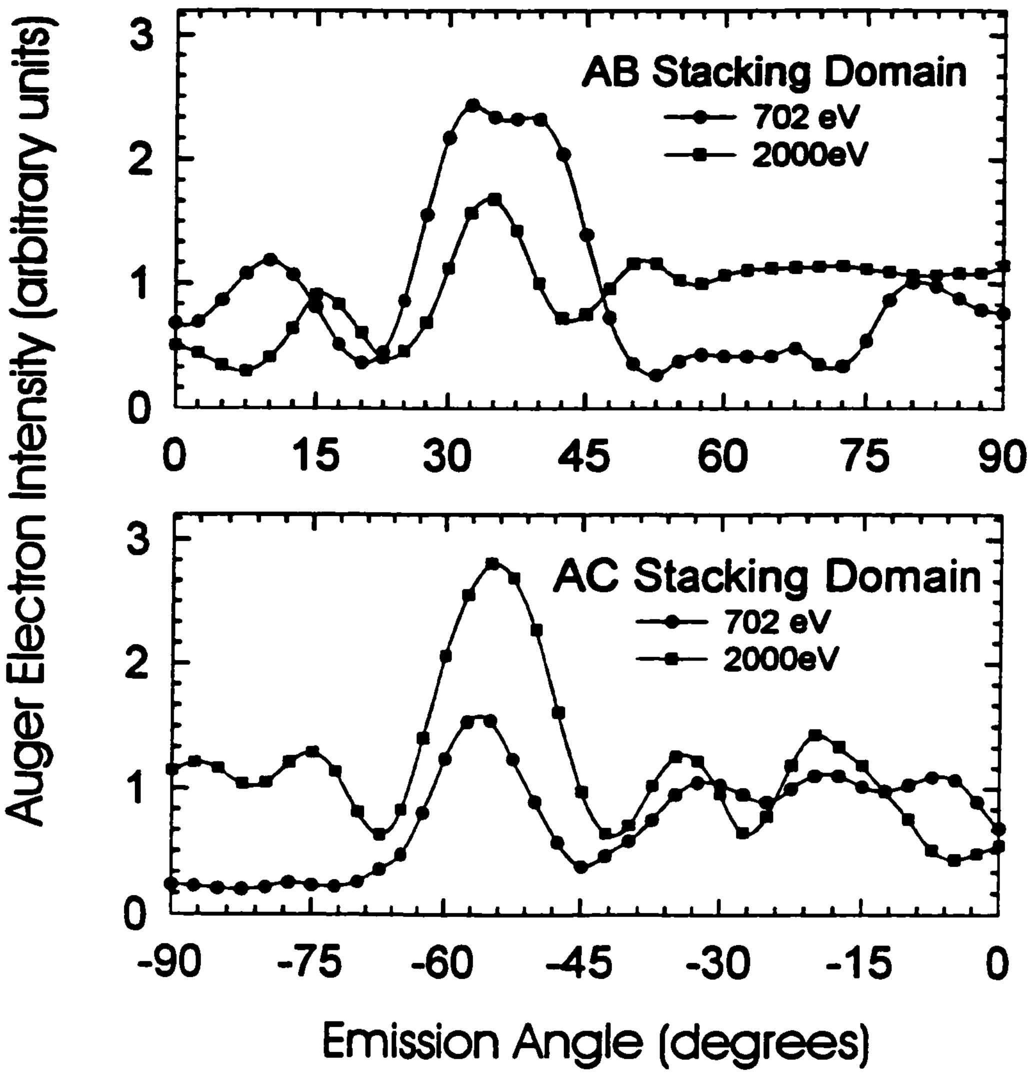

Figure 3-9
SSC simulations for 2000 eV and 702 eV Auger electrons showing the outgoing 702 eV peaks with the complementary incoming 2000 eV peaks. Both stacking domains descibed in the text are shown.

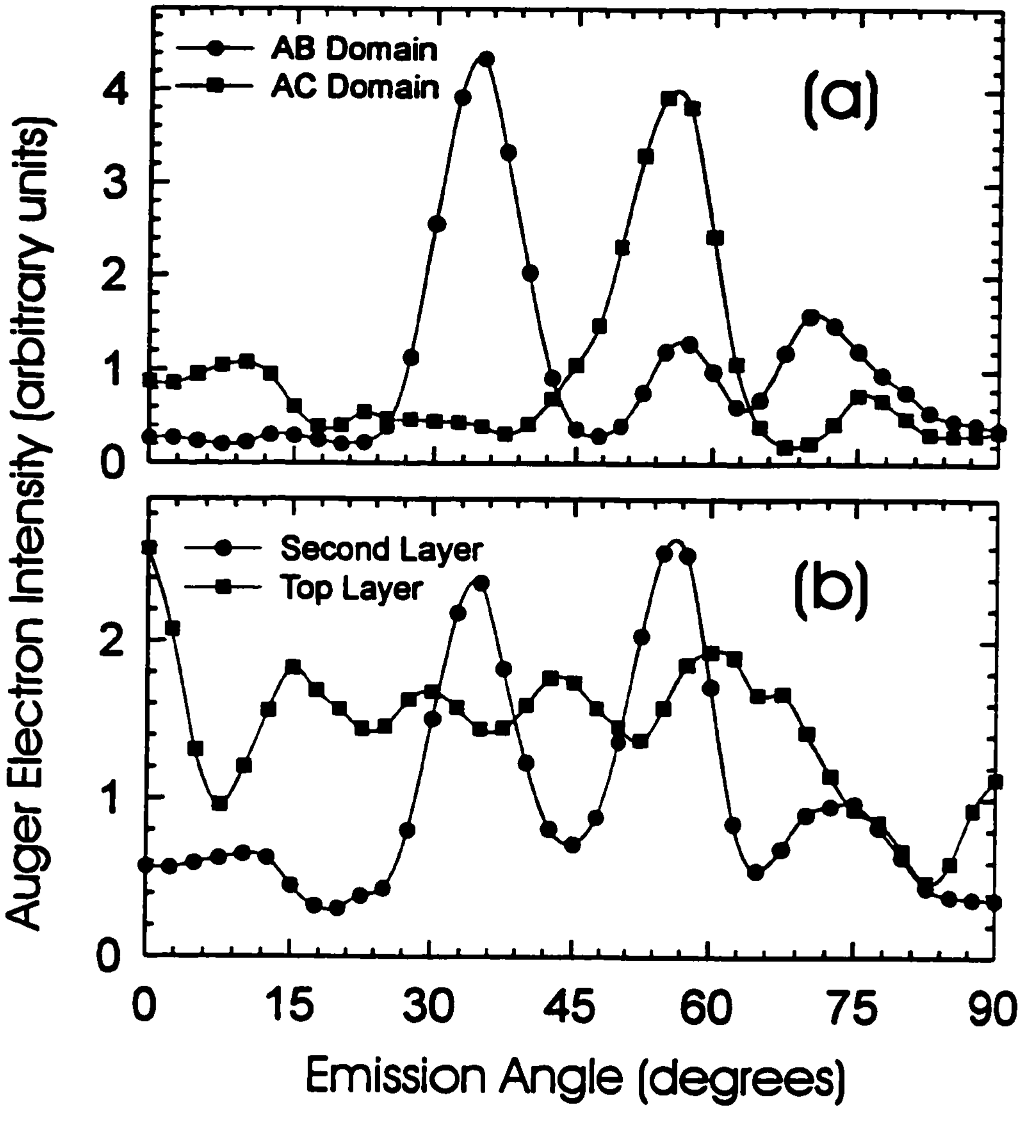

Figure 3-10
(a) Auger emission simulations for both fcc domains. The 702 eV and 2000 eV simulations have been multiplied together as described in the text. The emission angle for the AC domain has been transformed as discussed in the text.
(b) Auger emission simulations for emitters in the top and second layers of the fcc cluster. The contributions from both the AB and AC domains have been combined as described in the text.

The same procedure is followed for SSC simulations where the Fe emitter is placed on the surface of the 4 ML thick cluster. These simulations have less structure than the second layer simulations because there are no atoms above the emitter to focus the electrons. It is essential however, that these simulations be done, because they provide a normalised contribution from the atoms on the surface. This surface contribution is also shown in figure 3-10(b).

Auger emission is stimulated by 2000 eV electrons as they pass through an atomic layer. The Auger intensity from an atomic layer is proportional to energy deposited in the layer. The energy deposition is a function of the path length through the layer and the relative intensity of the beam at the layer.[59] If the atomic layer is d thick and Θ_c is the angle of incidence, the distance travelled in a layer is:

$$I(\Theta c) = \frac{\Pi}{d \cdot \cos(\Theta c)} = \frac{I_0}{\sin(\Theta)} \qquad (9)$$

The complementary angle (outgoing Θ) is used in the final definition and Π is a constant which has been absorbed into I_0, the intensity at $\Theta = 0$.

To reach an atomic layer, the 2000 eV must first travel through the preceding layers, where attenuation occurs. This is added to equation (9) by defining an attenuation length λ:

$$I(\Theta, n) = \frac{I_0}{\sin(\Theta)} \exp\left(-\frac{n \cdot d}{\lambda \cdot \sin(\Theta)} \right) \qquad (10)$$

Where n refers to the layer (n = 0 is the top layer). The attenuation length ($\lambda = 20$ Å) was estimated using the material dependent parametrisation suggested by Tanuma, Powell and Penn.[61,62] Figure 3-11(a) shows the top and second layer simulations after the angular and depth correction defined in equation (10) has been applied.

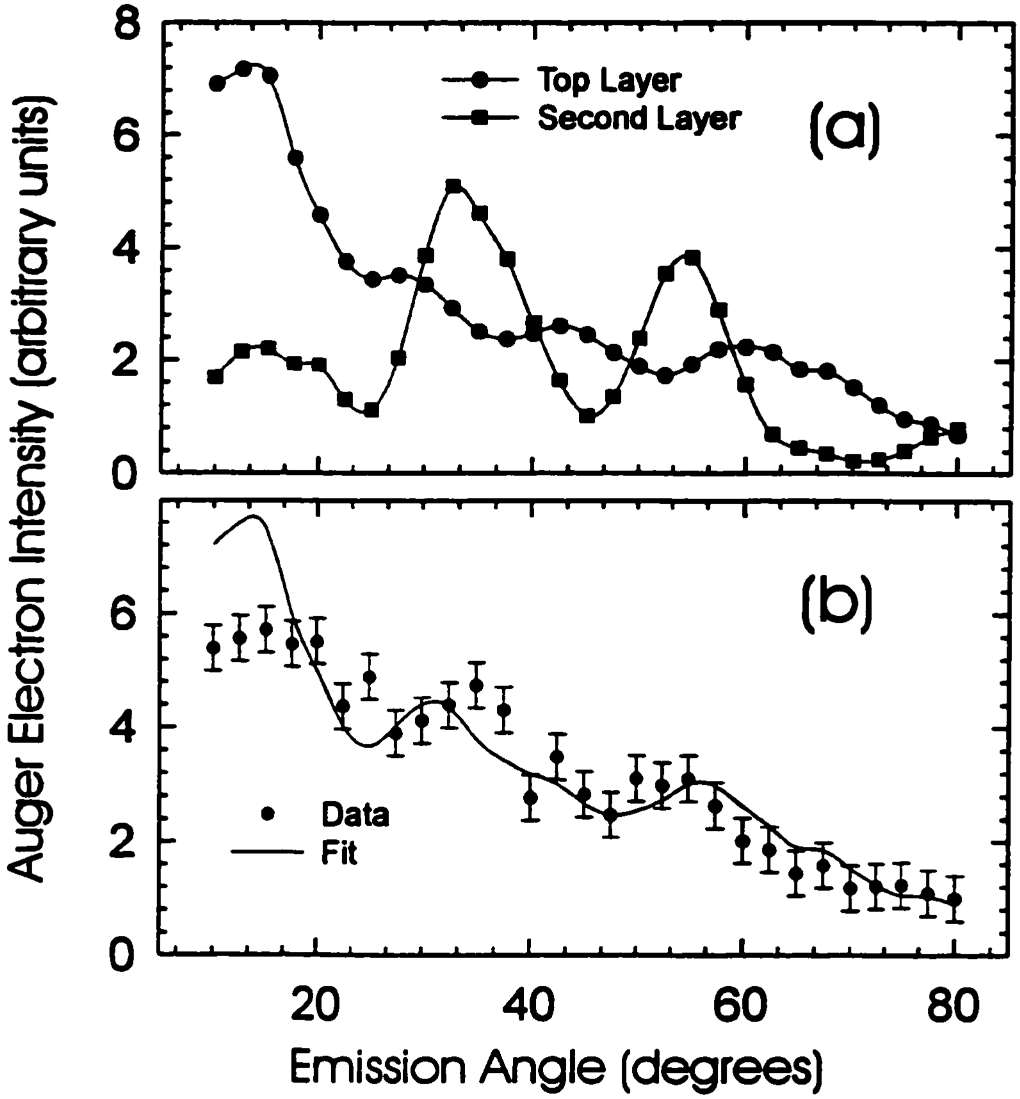

Figure 3-11
(a) Simulations for Auger emitters in the top and second layers. The angular corrections for the incident beam have been applied as discussed in the text.
(b) A least squares fit to the ARAES data from a 1 ML Fe film on the Ni(111)/W(110) substrate. The two simulations presented in part (a) of this figure were used as the basis functions in the fit. As discussed in the text, the data from 10° to 18.5° was not used in the fit.

The Chi-squared Fitting Routine

To determine how much of the Fe in a 1 ML film is in the second layer a chi-squared fit was performed. The ARAES data was analysed in a two parameter fit using the simulations in figure 3-11(a) as basis sets. The fitting parameters α and β were determined by the analytical minimistion of the chi-square sum:

$$\chi^2 = \sum_{\Theta} \frac{\left(I_{data}^{beam}(\Theta) - \alpha \cdot I_{top}(\Theta) - \beta \cdot I_{sec}(\Theta)\right)^2}{\sigma^2} \qquad (12)$$

Where $I_{top}(\Theta)$ and $I_{sec}(\Theta)$ are the simulations for an emitter in the top and second layers respectively and σ is the experimental uncertainty in the data.

The measure of the goodness of a chi-squared fit is the Q-factor, the incomplete gamma function $Q(\nu,\chi^2)$ where ν is the number of degrees of freedom in the fit (in our case $\nu = n-2$, where n is the number of ARAES data points) . The general rule is that if $Q \geq 0.1$ the fit is acceptable, if $0.001 \leq Q \leq 0.1$ the fit may be acceptable if the experimental uncertainties do not follow a normal distribution (an assumption of the chi-squared minimisation). Finally, if $Q \leq 0.001$, the fit is very likely unacceptable.[63]

The fit to the 1ML Fe data is shown in figure 3-11(b). For this fit an experimental uncertainty of ± 0.4 % was used. As indicated in the figure, data from 10° to 80° was available but only data from 20° to 80° was used in the fitting procedure, excluding the first four data points. These data points were excluded on the basis that the goodness of fit measure (Q) gave a value of 0.0002 for the 10° to 80° data. As data points were systematically excluded from the low angle side, the Q value rose to a value of 0.15 using data 20° to 80°.

This trend was observed when other data was analysed, suggesting that the model is sufficient to describe the data in the range of 20° to 80°, but fails at lower angles. There are two possible explanations for this. As discussed in the experimental errors section of this chapter, misalignment of the sample and the entrance aperture are most likely to happen at low angles. Also, the SSC simulation does not consider multiple scattering effects within and between layers. In similar experiments on Cu(111), Kief and Egelhoff report a significant energy dependant structure below 20° which they attribute to multiple scattering.[18] In our experiment this effect would likely be amplified by the enhanced Auger emission at low angles.

The fit presented in figure 3-11(b) gives the following parameters:

$\alpha = 1.0 \pm 0.2$

$\beta = 0.30 \pm 0.08$

This suggests that 24 ± 7 % of the Fe atoms are in the second layer of the film. The precise meaning of the above statement is that 24 % of the Fe atoms are below single atoms which focus the Auger emission.

A similar fit was performed to ARAES data for 2 ML Fe on Ni(111)/W(110) giving

$\alpha = 1.2 \pm 0.3$

$\beta = 0.8 \pm 0.2$

This suggests that 40 ± 14 % of the Fe atoms are in the second layer. This fit is complicated by the fact that the ARAES peaks from Fe atoms in the third layer are at the same positions as the peaks for the second layer (see figure 3-3) and therefore focusing from one or two over layers is difficult to distinguish.

The fitting result suggests that the 1.0 ML Fe film is reasonably flat. The 24 ± 7 % result is likely a combination of some interdiffusion and some three dimensional growth, both of which cannot be avoided in this system. This result, in combination with the AES deposition versus time analysis suggests that the growth mode is near layer by layer.

Chapter 4

The Thickness -dependent fcc to bcc Structural Change in Iron Films: Use of a 2 ML Ni/W(110) Substrate

Section 4.1

Introduction

The research paper which follows in section 4.2 is a complete report on the growth mode of the Fe/Ni(111)/W(110) system from 0 to 12 ML Fe coverage. Experimental techniques and computer simulations discussed in chapter 3 are used extensively in this study and the instrument described in chapter 2 was used to perform the ARAES measurements. The author of this thesis is the principal author of the research paper, having performed all of the experimentation and computer simulations. The author also is responsible for most of the analysis. D.Venus was involved as the author's Ph.D. supervisor, providing guidance throughout the project. Venus was also involved in the final analysis of the structural transition. After the author had developed the ARAES technique for use in the laboratory, C.S. Arnold used the technique to study ultrathin Co/W(110) films. Because the analysis of the Fe/Ni(111)/W(110) and the Co/W(110) data was done at the same time, Arnold has made a contribution to the development of the data analysis techniques.

This work has been submitted to the journal Physical Review B, November 1, 1996. The copyright on this work has not been assigned.

The thickness-dependent f.c.c. to b.c.c. structural change in iron films:

Use of a 2ML Ni/W(110) substrate

H.L. Johnston, C.S. Arnold and D. Venus

Deptartment of Physics and Astronomy
and Brockhouse Institute for Materials Research
McMaster University
Hamilton, Canada L8S 4M1

Abstract

The f.c.c. to b.c.c. structural change in the growth of ultrathin iron films, is studied for films grown on an (111) f.c.c. surface, in an attempt to mimic the geometry of the Martensitic transition in bulk iron, where the interface is formed from the close-packed planes of the two structures. The use of a 2 ML Ni/W(110) substrate allows good wetting and lattice matching of the iron, without introducing either significant interdiffusion at the interface, or a large amount of magnetic material. LEED and angle-resolved Auger electron spectroscopy show that the iron films grow as a slightly distorted (111) f.c.c. surface for 3 ML, after which a surface cell intermediate to f.c.c. and b.c.c. appears in a specific Kurjumov-Sachs (KS) orientation. Thicker films show a simultaneous relaxation of the surface unit cell to a b.c.c. structure, and the movement of the layer stacking from the position f.c.c. to the KS b.c.c. position. The approximate layer-by-layer evolution of the structure is in marked contast to the complicated growth transition seen for iron films grown on (001) f.c.c. surfaces. This promises to be a useful system to isolate the relation of the structural transition and magnetism, without important contributions from other growth processes.

A. Introduction

Iron grown as a thin, metastable film upon a face-centred cubic substrate has proven to be a fascinating and complex system for the study of magnetism at surfaces and interfaces, and for the demonstration of the links between film structure, morphology and magnetism. One factor which contributes to the changes in the magnetic properties of these films as their thickness is increased, is the transition from a metastable, epitaxial, f.c.c.-like growth structure, to a b.c.c.-like growth structure related to bulk b.c.c. iron. A number of methods, such as the use of surfactants,[1] have been used to stabilize the f.c.c. structure, but for pure, clean iron films, it is difficult to escape the fact that the b.c.c. structure has lower energy and makes a f.c.c. to b.c.c. growth transition inevitable. The relation of this structural change to the magnetic properties of the iron film has been studied extensively for films grown on noble metal substrates, and particularly[2] on Cu(001). Here, as a function of film thickness, one finds sheared face-centred tetragonal growth,[3] a transition f.c.c. region,[4] and finally b.c.c. growth,[5] all with characteristic and fascinating magnetic properties.[6] Unfortunately, the structure and morphology is greatly complicated by the tendancy of the iron to mix with the copper substrate,[7] and the film to roughen dramatically as the growth transition occurs.[5,8] It is only through an impressive effort that the contributions of these various issues to the magnetic behaviour have been identified and, to some degree, studied systematically. A positive aspect of these works is that Fe/Cu(001) is an ideal system to study the interaction of the many influences on film magnetism; an alternative viewpoint is that it might be fruitful to gain insight through the study of related systems where the magnetic behaviour is dominated by a single characteristic of the growth. This attitude has lead to interesting initial studies of iron films grown on Ni(001) and Co(001) substrates,[9] where intermixing of the film and substrate are expected to be less serious, and the growth transition itself should the overriding influence on the film magnetism. For these systems, however, the magnetic properties of the iron film are difficult to study since they may be slaved to the larger net magnetic moment of the substrate, and because it is difficult with many experimental techniques to separate the magnetic response of the iron atoms from that of the substrate atoms. However even these studies do not address the root of the problem: if one wishes to study the relation between the f.c.c. growth to b.c.c. growth transition on the magnetic properties of the iron film, the (001) surface is a poor choice for the f.c.c. substrate.

The thickness dependent structural change in iron films has much in common with the phase transition from the f.c.c. structure to the b.c.c. structure in bulk iron, which is a classic example of a first-order Martensitic transition.[10] In this diffusionless transition, an interface plane (termed the habit plane) moves through the bulk iron and divides the regions having f.c.c. and b.c.c. structures. These two regions are oriented such that a close-packed $\{111\}_{fcc}$ plane is parallel to a close-packed $\{110\}_{bcc}$ plane. The most likely alignments of the close-packed planes are the Kurjumov-Sachs (KS) , where a $<011>_{fcc}$ and $<111>_{bcc}$ direction are parallel, and the Nishiyama-Wasserman (NW), where a $<1\underline{2}1>_{fcc}$ and $<101>_{bcc}$ direction are parallel. The habit plane, however, is a plane which is invariant under the structural transformation, a condition which is possible because of the compensatory effects of lattice distortion and shear. The habit plane is often irrational, but in the case of pure iron (up to 0.4% C) the habit plane is the close-packed plane itself. Therefore, using the bulk transition as a model, one is prompted to study the growth transition in thin films in a geometry where the direction of increasing thickness is normal to the natural habit plane of the bulk transition — that is, on a (111) f.c.c. substrate. In this geometry, the f.c.c. to b.c.c. growth transition is roughly analogous to a bulk Martensitic transition "in progress" with the habit plane "frozen" at a certain depth in the film. Of course, there are important differences between the film and bulk situations. The thin films are, afterall, metastable, and are also much freer to distort in the direction normal to the film surface than are bulk samples along a crystallographically similar direction. Still, the essential soundness of this idea is consistent with the scanning tunneling microscopy studies[5,8] of the growth transition of iron films on Cu(001). A very complicated, but patterned, arrangement of defects and shear planes appear at an angle to the surface, and various regions of the surface undergo very different transitions. The

LEED pattern shows a series of reconstructions related to the shear of the surface layers[3] and the defect patterns[5], and the final Fe b.c.c. phase greatly resembles the close-packed (110) surface in an orientation with respect to the underlying (001) f.c.c. which is not observed for bulk geometries.[11] This process can be thought of as a method by which the natural habit plane for the transition, which is initially at an angle to the surface, can be re-established normal to the film growth direction.

This line of analysis recommends the study of iron films grown on Cu(111). A number of such studies have been performed with the finding that the epitaxially grown iron does not wet this surface well, but immediately forms islands.[2,12] The growth on the islands undergoes the transition to the b.c.c. structure before the islands themselves have properly coalesced. This leads again to the situation where there may be an interplay of the effects of the growth mode and the structural transition on the magnetic properties of the films. The search for a more ideal system leads again to the Ni and Co substrates, where better wetting is expected, and where Bauer and van der Merwe[13] have predicted that the details of the lattice matching on the close-packed planes should lead to relatively thick epitaxial iron growth. Studies of these systems consist mainly of transmission electron microscopy of the endpoint of the growth transition for thick films[14] — we are unaware of detailed layer growth studies. Even so, there remain the problems associated with the magnetic characterisation of a thin film grown on a magnetic substrate. It is therefore a happy coincidence that Ni is known to grow in a highly ordered (111) f.c.c. structure on a W(110) substrate, even for very thin film thicknesses of two or three monolayers.[15,16] Such a thin Ni buffer layer will continue to have magnetic consequences, but perhaps at least the master/slave relationship bewteen substrate and film will be reversed. This line of argument has lead to the present study of iron films grown on a 2 ML Ni/W(110) substrate, with the aim of discovering a simple example of the f.c.c. to b.c.c. iron growth transition which is amenable to magnetic studies, and with characterizing the structural aspects of that transition.

The remainder of this paper is divided into four sections. In part B, the preparation of the Ni/W(110) substrate is described and its structure is confirmed. In part C, the epitaxial growth of f.c.c. iron on the substrate is demonstrated, and in part D the transition to b.c.c. growth is documented and analysed. It turns out that one sees a transition dominated by intralayer atomic motions following simple geometric relations, in agreement with the foregoing discussion. This system therefore seems well suited for further studies of the relation of the structural transition and the magnetic properties of iron films.

B. Preparation of the 2ML Ni/W(110) substrate

The growth of thin Ni films on the W(110) surface has been well-characterized in a number of studies.[15,16] The purpose of the present section is to document the method of preparation of the substrate, as the properties of very thin films are much more sensitive to experimental uncertainties than are thick films. Figure 1 shows the geometry of the lattices involved. The solid outline defines a f.c.c. unit cell, and the dashed outlines define two b.c.c. unit cells which are oriented in the NW alignment (to the left of the f.c.c. cell) and one of the KS alignments (below the f.c.c. cell). In this paper, the W(110) single crystal substrate is always aligned as the NW b.c.c. cell in fig.1, and all LEED patterns, experimental substrate manipulations, etc., are presented with respect to this orientation in space and on the page. The tungsten crystal was cut and polished to within 0.4° of the $(110)_{bcc}$ surface, and was cleaned before each film deposition by heating to 1800 K in 5×10^{-7} Torr oxygen, and then flashing to 2500 K. This yielded a sharp LEED pattern and carbon contamination levels which were just detectable with a four-grid retardation Auger electron analyser. Ni was evaporated by electron bombardment of a pure wire, using an evaporator which had an integral flux monitor to ensure a constant depostion rate.[16] The LEED pattern showed initially pseudomorphic growth, then a 7x1 reconstruction along $W[001]_{bcc}$ for thicker films, and finally a six-fold pattern that was very close to hexagonal, with no reconstruction sattelite spots — all in agreement with previous results. In accord with these authors, we interpreted the hexagonal pattern as the formation of two stacking domains of the f.c.c. Ni(111) surface, and the 7x1 reconstruction as evidence for the NW relative orientation of the Ni and W unit cells, as illustrated in fig. 1. For exact matching along the Ni$[\underline{2}11]_{fcc}$ and W$[1\underline{1}0]_{bcc}$ directions, the Ni cell must be expanded by 3.7% from its bulk lattice constant. Along the W$[001]_{bcc}$ direction, the reconstruction matches nine Ni cells onto seven W cells by contracting the Ni cell by 1.0% from its bulk lattice constant. A matching of this type predicts a distorted f.c.c. cell with internal angle $\alpha_{fcc}=61.14°$, whereas an experimental value of $60.8\pm0.4°$ was determined for a 2ML film in the present experiments.

In order to accurately determine the thickness of the Ni layer, Auger electron spectra were recorded as a function of deposition time at room temperature in the energy interval containing the Ni 61 eV and W 48 ev Auger peaks. The spectra were fit using a least-square criterion to a linear combination of the spectra for the clean W substrate, and a thick Ni film where the W Auger peak was not detectable. The fitting constant for the Ni is plotted in fig. 2a as a function of deposition time. These data were fit in turn to one, two , three and four linear segments, with a least squares algorithm free to determine the slopes and intersection points of the lines. The χ^2 from each fit were compared using the f-test, which takes into account the reduction in degrees of freedom as the number of linear segments is increased. The statistical analysis suggests that the Ni Auger uptake curve is best represented by three linear segments, where there is a first weak slope change at the deposition time $0.44\tau_{fcc}$ and a stronger slope change at τ_{fcc}. The labelling of these times reflects our interpretation of the stronger slope change as the completion of the reconstructed monolayer, and the weaker slope change as associated with the end of pseudomorphic growth. (The LEED reconstruction was first visible at about $0.6\tau_{fcc}$.) These results are in detailed agreement with those of Kolaczkiewicz and Bauer,[15] with even the ratios of the slopes at the slope changes (0.70 and 0.53) being in quantitative agreement. These data confirm the very good wetting of W(110) by Ni, and serve to calibrate the Ni film thickness to within ±0.1 ML.

The very low solubility of most metals in W permits films to be annealed without causing intermixing at the interface. Experimentation showed that the LEED pattern of the Ni film was improved when the films were grown at an elevated temperature, and that this did not affect the Auger electron intensities. All the Ni/W(110) substrates in this study were thus prepared by growing the first monolayer at a substrate temperature of 550 K and subsequent layers at 390 K. The LEED pattern for a 2ML Ni film then had a sharp hexagonal pattern of spots, and more diffuse reconstruction spots which were significantly weaker than those observed for the monolayer.

C. Growth of f.c.c. Fe on 2ML Ni/W(110)

Since preliminary studies showed that growing Fe directly on 1ML Ni/W(110) lead quickly to a very diffuse LEED pattern, a 2ML Ni film was chosen as the thinnest practical magnetic substrate. The Fe evaporator was calibrated by LEED and Auger experiments of deposition directly onto the W(110) surface at room temperature. This system is known to produce a series of distinctive LEED patterns with increasing coverage, which were reproduced in the present studies.[18] Data for the Fe Auger uptake curve is plotted in fig. 2b, following the same analysis procedure described for the Ni deposition. Once again, according to the f-test, the data is best represented by three linear segments. The first, very weak change in slope has also been observed by Gardiner[19] (the ratios of slopes at these changes, 0.89 and 0.45, are in quantitative agreement with those measured by Gardiner), but the characteristic feature of this curve in previous studies at room temperature is the much stronger slope change which has be shown to represent the completion of the Fe bilayer[20] on W(110). This feature is therefore interpreted at $2\tau_{bcc}$, and it is then found that the first slope change occurs at $0.95\tau_{bcc}$. Using this calibration, the ratio of the areal atom densities on the W(110) and Ni(111) surfaces gives a time for the deposition of Fe equivalent to one pseudomorphic layer on Ni(111) as $\tau_{fcc} = 1.3\ \tau_{bcc}$. (Of course, this τ_{fcc} is different than that in fig. 1a, since a different evaporator is being calibrated.) A similar Auger intensity experiment was then performed for Fe deposition at room temperature on 2ML Ni/W(110), the results being presented in fig. 2c. The same analysis leads to three linear segments, with the unconstrained positions of the slope changes fit to $1.02\tau_{fcc}$ and $1.92\tau_{fcc}$ in terms of the independent calibration in fig. 2b. This is internally consistent evidence that the Fe wets the Ni film well, grows pseudomorphically on the strained f.c.c. template, and that in the initial stages at least the growth mode is approximately layer-by-layer. The thickness of the Fe films in ML in this paper, will therefore refer to the calibrated amount of material deposited in τ_{fcc}.

A final Auger electron spectroscopy experiment was performed to gain insight into the amount of intermixing of the Fe into the Ni film. 0.8ML of Fe was deposited onto 2ML Ni/W(110), and Auger spectra were recorded (close to room temperature) as a function of annealing temperature. The low energy region of the spectrum was fit to a linear combination of the Auger spectra of 2ML Ni/W(110) and a very thick Fe film. The higher energy region was fit to a single, clean W Auger spectrum. The resulting fitting constants are plotted in fig. 3, where the lines are guides to the eye. The W Auger intensity stays rather constant until an annealing temperature of 550 K, where it begins to increase. This is interpreted as the onset of significant islanding of the film, probably as islands on top of a single monolayer which is tightly bonded to the W surface. The Fe and Ni signals, however, change rather linearly starting immediately at the lowest annealing temperature. This is interpreted as intermixing of the Fe and Ni, and the lack of plateau at low annealing temperatures suggests that some intermixing has already occurred in the film as deposited. It is difficult to quantify the amount of intermixing from this experiment, but it is clearly a gradual process — annealing to 360 K, for instance, makes only a small change in the Auger intensities. Because of this, and because the Ni film is grown at slightly elevated temperature, the effect of growing the Fe film at slightly elevated temperature (360 K) was investigated. This lead to an improvement in the sharpness of the LEED pattern, and this growth temperature was therefore adopted for all subsequent films.

The structure of the Fe films was investigated using LEED patterns and angle-resolved Auger electron spectroscopy (ARAES). Initially, deposition of Fe on 2ML Ni/W(110) lead to no important changes in the LEED pattern observed for the 2ML Ni film. The sharpness of the spots was at first degraded, but then improved again, so that at

3ML of Fe, a sharp hexagonal LEED pattern with no reconstruction was obtained. This is illustrated in fig. 4, for a primary energy of 96 eV. An internal angle α_{fcc}=60.8±0.4° was measured from photographs of the pattern, and the lack of three-fold symmetry again indicates that there are domains of two stacking sequences present.

The angle-resolved Auger experiments[21] are illustrated schematically in the inset to fig. 5a. High energy Auger electrons are, to a good approximation, emitted isotropically by an excited atom, but the angular distribution of the Auger electrons can be perturbed if the emitting atom is in a crystalline enviornment. The trajectories of the electrons passing close to a positive ion core can be deflected towards the ion core, causing a focussing of the Auger electrons along the crystallographic directions where the ion cores are situated. This forward-focussing effect is strongest in very thin films where multiple forward-scattering interactions are not geometrically possible, and is observed primarily along the directions where nearest neighbours lie. For thicker films, the focussing along a linear chain of atoms is more complicated by multiple forward-scattering interactions, some of which may focus the electrons, and some of which may defocus the electrons.[22] Since elastic Auger electrons characteristic of different atom types can be resolved, this method gives structural information specific to the film and the substrate. Qualitative information concerning the film structure can be obtained by simply noting the presence and/or absence of peaks in ARAES at the emission angles characteristic of the nearest neighbour directions in different crystal structures. In the present experiments, the films were rotated about the NW$[001]_{bcc}$ direction of the W crystal illustrated in fig. 1 (this is equivalent to the $[01\underline{1}]_{fcc}$ direction of the 2ML Ni). Assuming the f.c.c. stacking position marked "A" in fig. 1, the geometry illustrated in the inset to fig. 5a is obtained, and forward-focussing at Θ_{out}=35° is expected. Assuming the alternate f.c.c. stacking position in the upper half of the f.c.c. unit cell in fig. 1, predicts a peak in the ARAES at Θ_{out}=55°. Assuming a b.c.c. structure in the orientation of the NW orientation of the W substrate predicts a peak at Θ_{out}=45°.

The ARAES experiments were performed with a fixed angle between the incoming primary, 2000 eV electron beam and the entrance aperture of the electron energy analyser, such that $\Theta_{in}+\Theta_{out}=90°$. The angular resolution of the electron optics was ±2°. An electron energy spectrum was recorded to identify the peak energy of the Fe (702 eV) Auger electrons, and two positions suitable for extrapolating a linear background to the peak. In order to compensate for the possible drift of the electron gun current, the electron count was recorded at these three energies in a rapid series of interleaved time steps which totaled approximately one minute per point. The ARAES data was then evaluated as the ratio of the Auger peak counts minus the background, all normalized to the background. While this method removed spurious temporal drifts, it introduced an arbitray scale of normalization — the angularly dependent inelastic background of the Auger spectrum. This was removed by constructing the average, angle-resolved inelastic background as measured in many ARAES experiments. Since this function was found to be smoothly varying and had little scatter, it was fit to a polynomial, and the resulting function was multiplied times the normalized ARAES spectra to give the angular dependence of the Fe Auger electrons alone, normalized to constant exciting beam current. These data are shown in fig. 5a for 1, 2 and 3ML Fe films grown on 2ML Ni/W(110). The spectra for 2 and 3ML Fe show clear peaks at $\Theta_{out}=35°$ and 55°, and no discernable peak at 45°, indicating that two stacking domains of f.c.c. iron are present (in agreement with the LEED pattern), but that b.c.c. iron is not present. Small peaks may also be present at the f.c.c. forward-focussing angles for the 1ML Fe film. Since the Fe emitter must be below another atom to produce forward-focussed electrons, the size of these peaks is a measure of the imperfection of the Fe films due to a combination of mechanisms: i) the degree to which the 2ML Ni substrate contained regions of 1ML thickness, ii) the uncertainty in the Fe film thickness, and iii) the amount of intermixing of Fe into the Ni film. The data are evidence that none of these effects is serious.

It is also useful to compare the data to quantitative calculations of Auger electron forward-focussing. This is introduced here, as it will be particularly important in the next section. The ARAES spectrum from a single emitter at a particular lattice site, n, is denoted $I_{out}(\Theta_{out},n)$, and may be calculated by assuming that an isotropic, outgoing electron wave is scattered elastically by an array of atoms, where only independent, single-scattering events are considered.[23] The scattered amplitudes far from the array are summed and the scattered intensity is computed. The present experimental geometry is complicated by the fact that the incoming electron beam may also experience forward-focussing. This can be seen in the insert to fig. 5a, where the beam from the electron gun may be focussed by a first-layer atom onto a second layer atom, so that the latter experiences a greater excitation probability at $\Theta_{in}=55°$ than at other angles. In photoemission, the state of the outgoing photoelectron, and that of an incoming plane-wave electron are related by time-reversal. Since this is also found to be a good approximation for high energy Auger electrons,[24] the incoming focussing $I_{in}(\Theta_{in},n)$ may be calculated by the same method as $I_{out}(\Theta_{out},n)$, but using a transformation of variables.[25] The observed angular dependence of Auger emission from a particular atom will then be the product of these two. Finally, the contribution from all atoms must be normalized to the same scale, and summed. The calculation described thus far is normalized "per Auger electron generated at site n", and the relative probabilities of excitation of atoms in different lattice sites is given by the relative energy dissipation at these sites. A first approximation to this function is given by the phenomenological attenutation of the primary beam.[26] This varies exponentially from layer to layer, and as $1/\sin\Theta_{in}$ within each layer as the primary beam approaches glancing incidence. Taking these together, the experimental measurements are given by

$$I_{net}(\Theta_{out}) = \underline{n}\ I_{in}(\Theta_{in},n)\ I_{out}(\Theta_{out},n)\exp[-d(n)/(\lambda\sin\Theta_{in})]\,/\,\sin\Theta_{in}\,, \qquad (1)$$

where d(n) is the perpendicular depth of the lattice site from the surface, and λ is the inelastic attenutation depth. Single-scattering calculations were carried out using the program SSC, developed by Friedman and Fadley[25], with scattering phase shifts calculated in the program FEFF, developed by Rehr, Albers and Mustre de Leon[27]. These are presented in fig. 5b for the cases of 1 and 2ML Fe films, where the single-scattering assumption is strictly valid. The index n was summed over the two inequivalent positions in both possible f.c.c. stacking sequences. The agreement between the measured and calculated spectra is very good, and confirm the f.c.c. structure of the Fe. It also permits a more detailed understanding of three important points: i) the rising "background" as Θ_{out} becomes smaller is a true effect which results from increased energy deposition in the surface region at glancing angles of primary electron incidence; ii) The same mechanism enhances the intensity of peaks at small emission angles relative to those at large emission angles. Thus the peaks at 35° and 55° due to equal amounts of the two f.c.c. stackings are not equal in height; iii) in the present geometry the appearance of the characteristic peaks at 35°, 45° and 55° are not affected by the forward-scattering of the incoming beam, because in all three cases, the incoming and outgoing beams experience forward-focussing at equivalent geometries. At very low emission angles, however, the enhanced sensitivity can lead to prominent peaks due to second-order focussing (as between 15° and 20°) which complicate a qualitative interpretation.

In conclusion, the Auger uptake curves, LEED and ARAES measurements are a self-consistent data set which indicate that up to 3ML Fe grows on the 2ML Ni/W(110) substrate as two domains of a slightly distorted $(111)_{fcc}$ surface with different stacking sequences, which are epitaxial to the Ni film.

D. F.C.C. to B.C.C. transition for Fe/2ML Ni/W(110)

The first indications of the growth of b.c.c. Fe are given by LEED patterns recorded for 4ML Fe films, as shown in fig. 6. Fig. 6a shows the pattern for a primary energy of 96 eV, and fig. 6b gives a schematic interpretation. Four of the six the bright spots associated with the distorted f.c.c. Fe have split into triplets, so that the twofold symmetry of the pattern is more pronounced. Variation of the primary energy shows that the upper spots on the left are correlated with the lower spots on the right, and *vice versa*. Fig. 6b shows that these new spots can be represented as a superposition of two domains of b.c.c.-like units cells in an orientation which is given by the KS orientation in fig. 1. Two qualitative features are worth particular attention. First, the observed KS orientations represent only two of the six possible such orientations.[28] A true, unstrained f.c.c. cell has three equivalent nearest neighbour directions along which the b.c.c. nearest neighbours in the close-packed plane may be aligned (each giving two KS domains related by a mirror plane). However, the 3ML Fe films show a distortion equivalent to that seen for the 7x1 reconstructed Ni films, where there is a 3.7% expansion along $[\underline{2}11]_{fcc}$ and a 1.0% compression along $[01\underline{1}]_{fcc}$. Using the nearest neighbour distance for bulk Fe, the observed KS orientation represents a 0.7% compressive strain along the $[01\underline{1}]_{fcc}$ matching direction, whereas matching along the nominal $[\underline{1}01]_{fcc}$ or $[\underline{11}0]_{fcc}$ directions would require a 2.9% expansion. (A NW orientation requires a 10.4% expansion.) A rigid model therefore shows a clear reduction of strain energy for the observed KS orientations. Second, the new spots represent a distorted b.c.c.-like cell, since the internal angle α_{KS} defined in fig. 1 is equal to ±57.6° instead of the true b.c.c. value of ±54.7°. The observed distortion allows the b.c.c.-like cell to maintain registry with the f.c.c. underlayers in the $[\underline{1}10]_{fcc}$ direction in direct space, as can be seen by the horizontal alignment of the spots in fig. 6a. This arrangement presumably reduces the energy of interlayer interaction.

LEED patterns of thicker films show a fading of the f.c.c. spots, and an evolution of the b.c.c.-like KS unit cells to smaller values of α_{KS}. A new qualitative feature is seen first for 8ML Fe films. It is illustrated in a 12ML Fe film in fig. 6c, where it is fully developed. The f.c.c. spots are now absent, but six new spots are present (two are hidden in the photograph by the shadows cast by a Helmholtz coil arrangement near the sample holder). The new spots are indicated as open circles in the schematic representation in fig. 6d. They can be represented as a b.c.c.-like cell in the NW configuration in fig. 1, with internal angle α_{NW}=55.4°. The figure also shows that the orginal KS cells have evolved such that α_{KS} is also equal to 55.4°, so that the entire LEED pattern can be represented as the incoherent superposition of three equivalent b.c.c.-like cells: two KS cells rotated ±55.4° from an NW cell, all referenced to the underlying f.c.c. Fe. It is not clear why the emergence of domains of the NW orientation is favourable, other than to note that they occur on the b.c.c.-like surface (not on the f.c.c. surface), and then only once the internal angle α_{KS} has obtained a value close to that of a true b.c.c. cell. The particular NW orientation which appears is the only one that preserves the twofold symmetry of the original, distorted f.c.c. surface. It may be that this orientation nucleates at the boundaries where the different KS domains meet.

The evolution of the b.c.c. cells measured from photographs of LEED patterns is summarized in fig. 7, where the internal angles α for both orientations are presented as a function of film thickness. The internal angle of the f.c.c. cell is also shown for those thicknesses where it is observed. This plot is very suggestive of a f.c.c. to b.c.c. transition in three distinct steps. The first is the sudden appearance of a stucture intermediate to f.c.c. and b.c.c. in the KS orientation, followed by a gradual relaxation of the surface unit cell to that of a b.c.c. structure. Finally, identical b.c.c. cells nucleate in the NW orientation. The evidence for the gradual relaxation of the KS cells is particularly intriguing. LEED at a primary energy near 100 eV should measure a weighted average of the structure of the first few atomic layers, giving the smearing of the spots in fig. 6 perpendicular to the radial direction — that is, along the direction the spots move with changing film thickness. The fact that the spots do not degrade into a continuous arc, but rather remain relatively well-defined and show measureable dispersion, suggests that the b.c.c. iron is not growing as rough islands which expose many layers with a range of α_{KS}, but rather continues to follow approximately layer growth, with each layer having a unit cell which is incrementally relaxed from the previous layer. This is further supported by the rapid disappearance of the f.c.c. LEED spots.

As the surface unit cell distorts continuously towards a b.c.c. structure, the potential minimum inside the cell is expected to shift from the f.c.c. stacking position, labelled by "A" in fig. 1, to one of the b.c.c. stacking positions labelled "B" and "C" in fig.1. Since the layer spacing between bulk close-packed f.c.c. and b.c.c. planes is the same (when measured in units of the nearest neighbour distance), no change in the interlayer spacing is expected. In order to investigate the stacking of the surface unit cells, a series of angle-resolved Auger experiments were conducted for films showing the transition to b.c.c. Fe. These are presented in fig. 7a. The extended lines on the y-axis show the amount by which successive curves have been displaced to avoid overlapping. In overview, the data first show a dispersion of the peaks from the f.c.c. angles of 35° and 55° to smaller and larger angles, respectively, as the films get thicker. The latter peak becomes significantly weaker, appearing as a shoulder. Then, for 12ML Fe films, there is a complete change in character, with a very strong peak occurring at 45°.

These curves may be interpreted by comparison to the calculated ARAES spectra for different stacking positions of the layers along the lines AC or AB in fig.1. Since the single-scattering theory is strictly valid for films only 1 or 2ML thick, and since the most prominent structure is expected to arise from simple, forward-focussing by nearest neighbour atoms, the following approximate method has been adopted. A two layer system is formed from a bottom layer a true f.c.c. Fe structure, and a top layer in the intermediate KS structure given by the LEED pattern in fig. 6a. The interlayer distance is assumed to be constant at the distance common to the close-packed planes in both f.c.c. and b.c.c. bulk structures. Calculations made according to eq.(1), for different layer stacking sites along the lines AB and AC are presented in fig. 7b. The solid symbols represent the calculations for a progression of the stacking site along AC, from the f.c.c. site to the KS b.c.c. site. The open symbols represent the calculation at the endpoint stacking site B for the NW b.c.c. structure. Because of the neglect of contributions from atoms deeper than the second Fe layer, the calculated peak heights are not as reliable as the peak positions. There is an impressive agreement with the evolution of the calculated and experimental spectra. The calculated peak positions are summarized in fig. 9. The ARAES experiments up to 8 ML thick Fe films are well represented by the calculations for movement of the stacking position from the f.c.c. to the KS b.c.c. site. The approximate nature of the calculation, and the width of the experimental peaks make a more precise correlation of stacking position against film thickness unreliable. For the 12ML Fe films, the experiments are in good agreement with the calculation for stacking at the NW b.c.c. site.

These results give strong support to a description of f.c.c. to b.c.c. transition in these films as a layer-by-layer evolution of the surface cells in both shape and stacking position. The ARAES and LEED studies are internally consistent, with the stacking position moving toward the KS b.c.c. site as the surface unit cell relaxes to two domains of the true b.c.c. structure in the KS orientation. Only when this process in nearly complete does the LEED show the appearance of the NW b.c.c. domains, in agreement with the strong peak at 45° in the ARAES at these thicknesses. The experimental ARAES spectrum for the thickest film (12 ML) is in fact well-represented by a summation of the calculated curves for the KS and NW stacking sites, since the calculation for the KS site shows little structure. The details of the emergence of the NW b.c.c. domains remains unexplained, as it is not clear how this unit cell can be accomodated to the existing KS b.c.c. growth without a significant distortion which is not observed in the LEED pattern. To our knowledge, the f.c.c. to b.c.c. structural changes in ultrathin Fe films grown on $(111)_{f.c.c.}$ surfaces studied so far, show either a KS or NW orientation, but not both.[28,29] Some studies of thick Fe films (of order 100 ML) grown on a Ni(111) single crystal show a combination of KS and NW domains,[14] but this seems to correspond to a loss of epitaxy to the substrate, since all possible configurations are present.

E. Discussion

Insofar as the experimental methods used in these studies can detect, Fe films grown on 2ML Ni/W(110) show a simple f.c.c. to b.c.c. growth transition, with evolution of the structure in the direction of film growth. This is accomplished by the nucleation of surface unit cells in the KS orientation which are midway between f.c.c. and b.c.c., followed by the incremental evolution of the shape and stacking position of the cells to that of true b.c.c. The present studies give no direct indication of the film morphology, but the continuous evolution of the LEED and ARAES measurements suggest that the film growth in the transition region is not rough, but rather exposes only a few layer thickness at any time. This type of incremental structural transition is unusual in that the b.c.c. structure does not seem to be introduced as defects which reduce the in-plane strain of the film, while leaving the structure of the f.c.c. and b.c.c. portions fixed. Scanning tunneling microscopy (STM) and reflection high energy electron diffraction studies of the growth of these films would provide a most welcome test of these conclusions. The STM experiments may have difficulty in detecting the growth transition itself, since the layer spacing of the f.c.c. and b.c.c. structure is expected to be very nearly the same.

It is interesting to speculate on the rough analogy between the growth transition in these films and the Martensitic phase transition in bulk Fe. In the first place, the present finding of a simple transition with a planar geometry supports the use of a film geometry where the surface lies parallel to the habit plane in the bulk transition. These experiments show at first a discontinuous change in the surface unit cell (as would be expected in an analogous first-order phase transition), followed by an incremental relaxation of the unit cell, as might be forseen for a "frozen" Martensitic transition front. The most analogous metallurgical situation would seem to be the interfaces of finite, metastable Martensitic particles in bulk materials. Recent electron microscopy studies of Cu precipitates in a b.c.c. Fe matrix show a series of epitaxial relationships, depending on particle size.[30] For particles with diameters less than 17 μm, the three-dimensional boundary constraints force complicated twinning structures which reduce strain. Interfaces more analogous to planar films are found for larger particles. Here, an untwinned, distorted f.c.c. structure close to the KS orientation, is found. Growth of the particle finally leads to an f.c.c. structure in the KS orientation for particle sizes greater than 40μm. While these studies of precipitates are of a b.c.c. to f.c.c. Martensitic transition (the reverse of the present film studies), in both cases there is a gradual, epitaxial accommodation as the relative importance of the interface is decreased because the particle/film grows larger/thicker.

Finally, it appears that the use of the 2ML Ni/W(110) substrate provides a tractable experimental system for the study of the magnetic behaviour of Fe films as they undergo the f.c.c. to b.c.c. growth transition. Despite the extreme thinness of the Ni buffer layer, epitaxial f.c.c. Fe films with little intermixing are produced up to a thickness of 3 ML. The slightly distorted f.c.c. unit cell further simplifies the growth transition by causing a preferred orientation among the many possible KS alignments. There is hope that the Ni will not dictate the magnetic properties of the Fe film, except perhaps in the interesting region of ≤ 1 ML Fe. These, and other magnetic studies are currently underway.

Acknowledgements

We are pleased to acknowledge the technical assistance of M. Kiela. We thank G. Purdy for a critical reading of the manuscript. This work has been supported by the Natural Sciences and Engineering Research Council of Canada. H.L.J. gratefully acknowledges an O.G.S. scholarship from the goverment of Ontario.

References

1. A. Kirilyuk, J. Giegiel, J. Shen and J. Kirschner, Phys. Rev. B **52**, 11 672, (1995).

2. Extensive references are found in M.T. Kief and W.F. Egelhoff Jr., Phys. Rev. B **47**, 10 785, (1993).

3. J.V. Barth and D.E. Fowler, Phys. Rev. B **52**, 11 432, (1995).

4. M. Wuttig and J. Thomassen, Surface Sci. **282**, 237, (1993).

5. M. Wuttig, B. Feldmann, J. Thomassen, F. May, H. Zillgen, A. Brodde, H Hannemann and H. Neddermeyer, Surface Sci. **291**, 14, (1993).

6. J. Thomassen, F. May, B. Feldmann, M. Wuttig and H. Ibach, Phys. Rev. Lett. **69**, 3831, (1992); D.P. Pappas, C.R. Brundle and H. Hopster, Phys. Rev. B **45**, 8169, (1992); D. Li, M. Freitag, J. Pearson, Z.Q. Liu and S.D. Bader, Phys. Rev. Lett. **72**, 3112, (1994).

7. D.A. Steigerwald, I. Jacob and W.F. Egelhoff Jr., Surface Sci. **202**, 472, (1988).

8. J. Giergiel, J. Kirschner, J. Landgraf, J. Shen and J. Woltersdorf, Surface Sci. **310**, 1, (1994); J. Giergiel, J. Shen, J. Woltersdorf, A. Kirilyuk and J. Kirschner, Phys. Rev. B **52**, 8528, (1995).

9. W.L. O'Brien and B.P. Tonner, Phys. Rev. B **52**, 15 332, (1995); E.J. Escoria-Aparicio, R.K. Kawakami and Z.Q. Qiu, J. App. Phys. **79**, 4964, (1996).

10. A simple introduction is: L. Delaey in *Materials Science and Technology, Vol. 5*, edited by R.W. Cahn, P. Haasen and E.J. Kramer, (VCH, New York, 1991).

11. W. Pitsch, Philos. Mag. 4, 477, (1959).

12. A. Brodde and H. Neddermeyer, Ultramicroscopy **42-44**, 556, (1992).

13. E. Bauer and J. H. van der Merwe, Phys. Rev. B **33**, 3657, (1986).

14. J. Echigoya, M. Nemoto and H. Suto, Trans. Jap. Inst. Metals **21**, 99, (1980).

15. J. Kolaczkiewicz and E. Bauer, Surface Sci. **144**, 495, (1984).

16. K-P. Kämper, W. Schmidt, G. Güntherodt, and H. Kuhlenbeck, Phys. Rev. B **38**, 9451, (1988).

17. T. Jones, J. Sawler and D. Venus, Rev. Sci. Instrum. **64**, 2008, (1993).

18. U. Gradmann and G. Waller, Surface Sci. **116**, 539, (1982).

19. T.M. Gardiner, Thin Solid Films **105**, 213, (1983).

20. M. Przybylski, I. Kaufmann and U. Gradmann, Phys. Rev. B **40**, 8631, (1989).

21. W.F. Egelhoff Jr., in *Ultrathin Magnetic Structures I*, edited by J.A.C. Bland and B. Heinrich, (Springer, Berlin, 1994).

22. A.P. Kaduwalla, D.J. Friedmann and C.S. Fadley, J. Electron. Spect. Rel. Phenom. **57**, 223, (1991).

23. D.J. Friedmann and C.S. Fadley, J. Electron Spect. Rel. Phenom. **51**, 689, (1990).

24. S. Chambers, Adv. Physics, **40**, 357, (1991).

25. S. Chambers, J.M. Vitomiron and J.H. Weaver, Phys. Rev. B **36**, 3007, (1987).

26. Y. Gao and J. Cao, Phys. Rev. B **43**, 9692, (1991).

27. J.J. Rehr, A.C. Albers and J. Mustre de Leon, physica b **158**, 417, (1989).

28. U. Gradmann and P. Tillmanns, phys. stat. sol. (a) **44**, 539, (1977); D. Tian, F. Jona and P. Marcus, Phys. Rev. B **45**, 11 216, (1992).

29. B. Voigtlander, G. Meyer and N.U. Amer, Surface Sci. **255**, L529, (1991); S. Andrieu, M. Piecuch and J.F. Bobo, Phys. Rev. B **46**, 4909, (1992).

30. P.S. Othen, M.L. Jenkins and G.D.W. Smith, Phil. Mag. A **70**, 1, (1994).

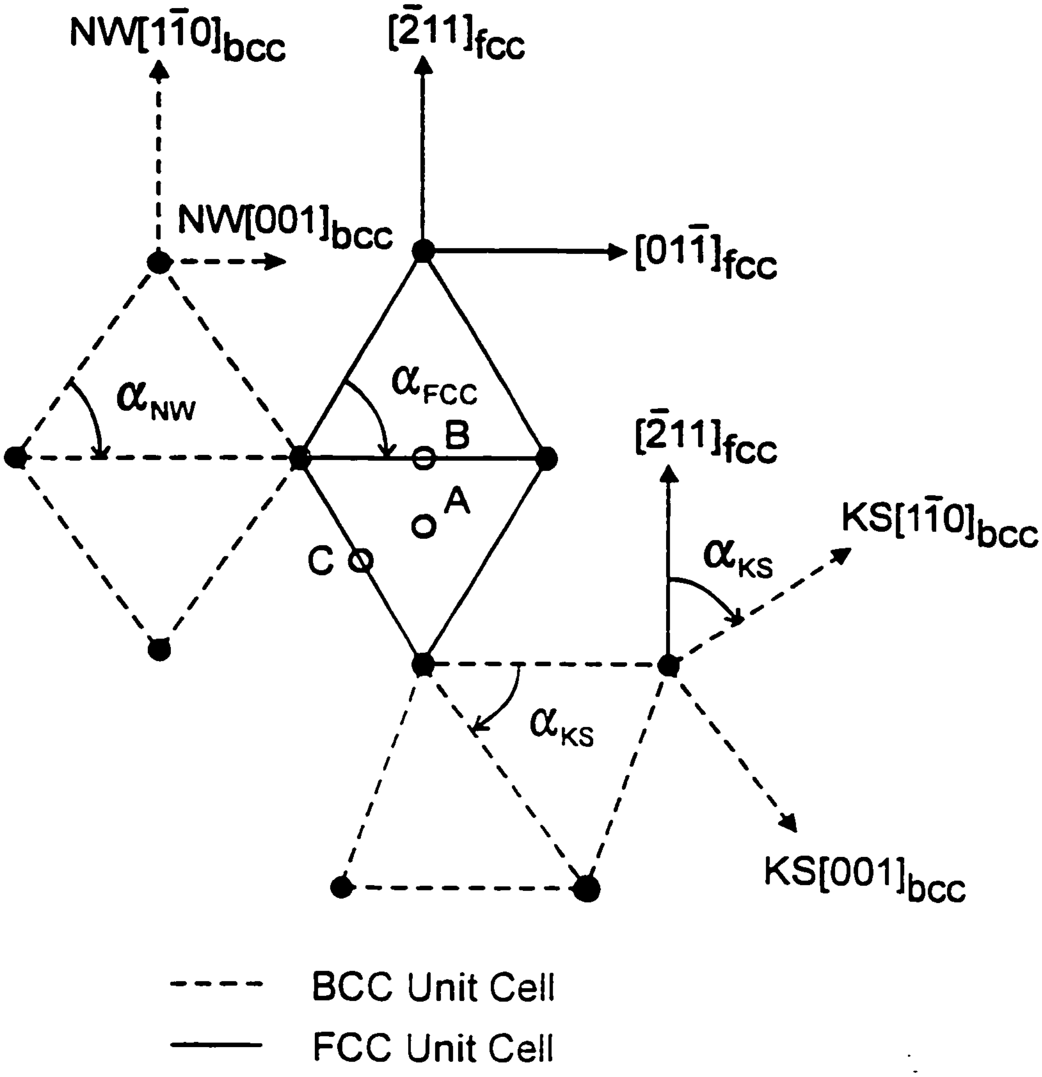

Fig. 1 - The relative orientation of the surface unit cells of the substrate and films are illustrated, with the surface normal projecting out of the page. A $(111)_{f.c.c.}$ surface cell is shown by the solid outline, and dashed lines show the NW and KS orientations of the $(110)_{b.c.c.}$ with respect to it. The internal angles α are defined for each cell type. The open circles mark the atomic position of the the next layer for a f.c.c. structure (A), a NW b.c.c. structure (B), and a KS b.c.c. stucture (C). The $W(110)_{b.c.c.}$ single crystal substrate is aligned as the NW b.c.c. cell.

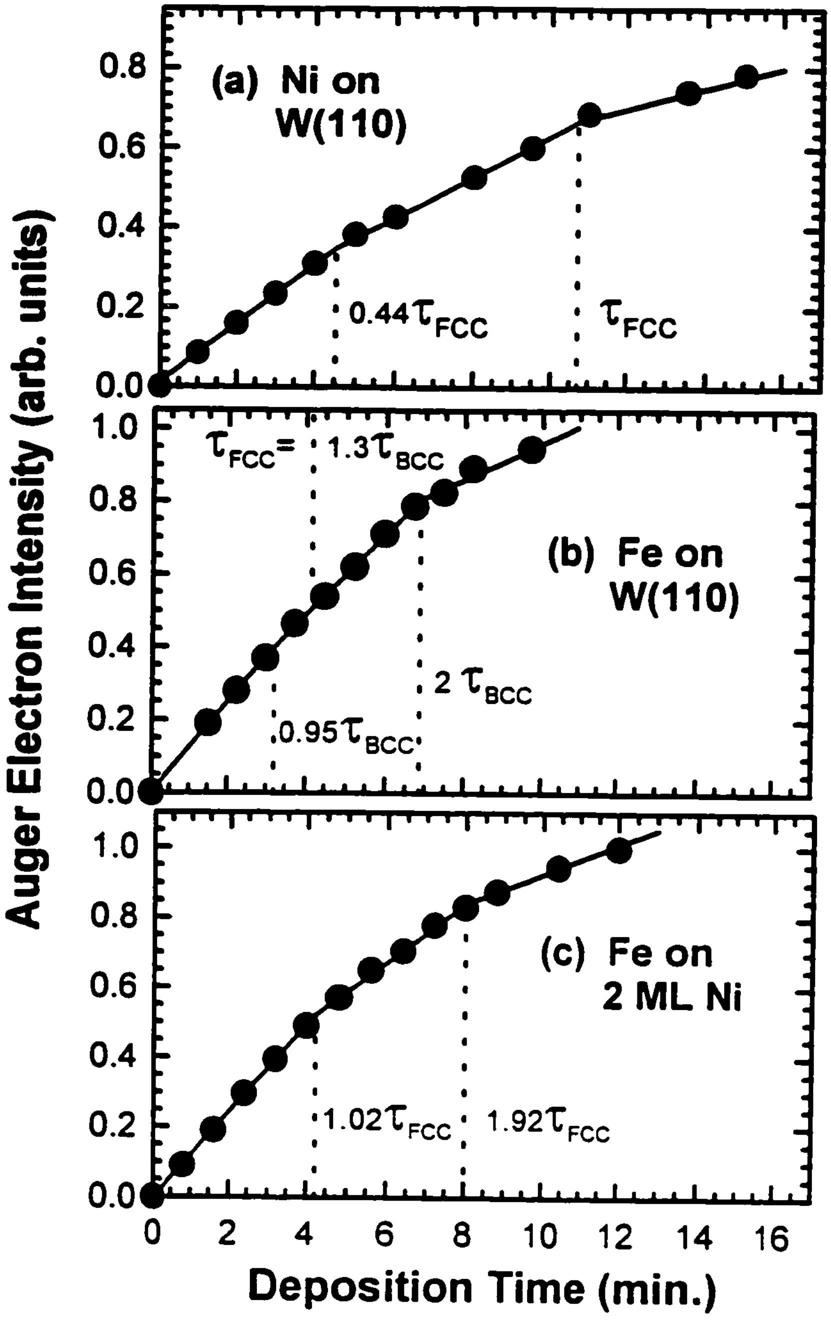

Fig.2 - The intensity of characteristic lines in the Auger electron spectroscopy spectra as a function of the time of metal evaporation. a) Ni (61 eV) deposited on W(110). b) Fe (47 eV) deposited on W(110). c) Fe (47 eV) deposited on 2ML Ni/W(110). The lines and labelled times τ are unconstrained, linear least-squares fits to linear segments, and are discussed in the text.

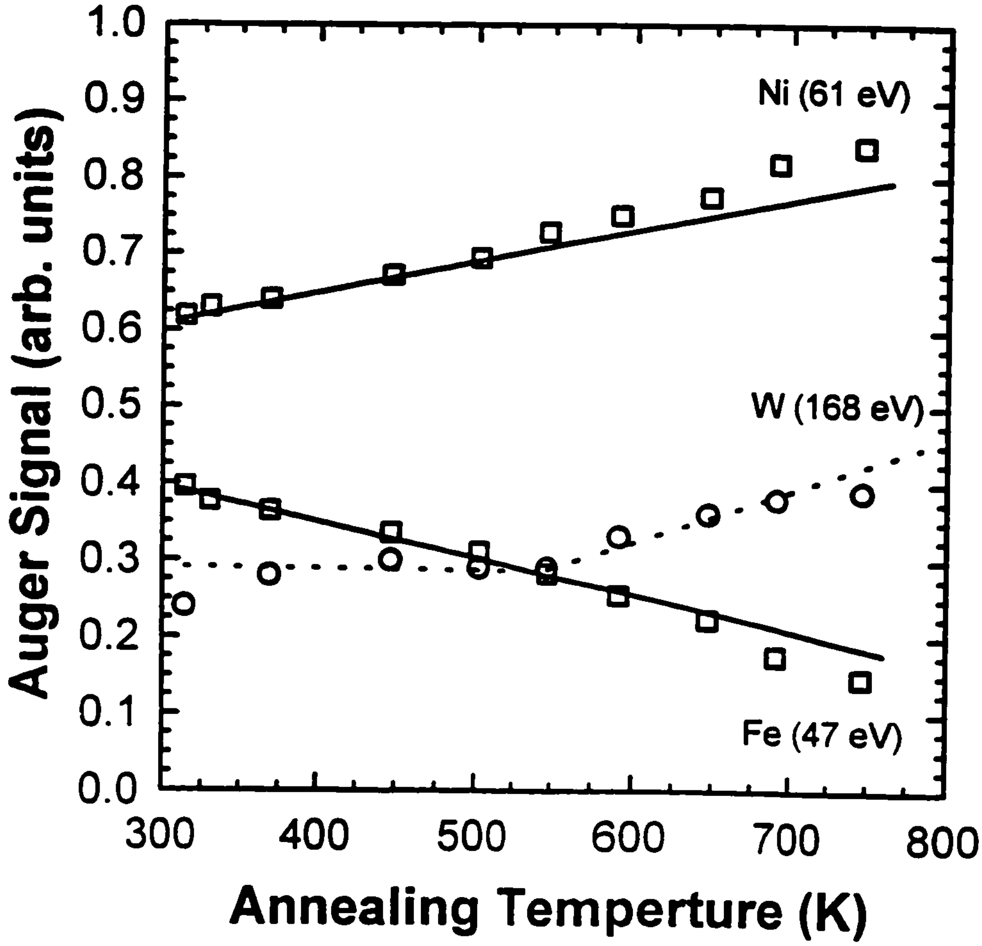

Fig. 3 - The intensity of characteristic lines in the Auger electron spectroscopy spectra for a 0.8ML Fe/ 2ML Ni/W(110) film, which was grown at room temperature, and annealed to successively higher temperatures. The lines are guides for the eye.

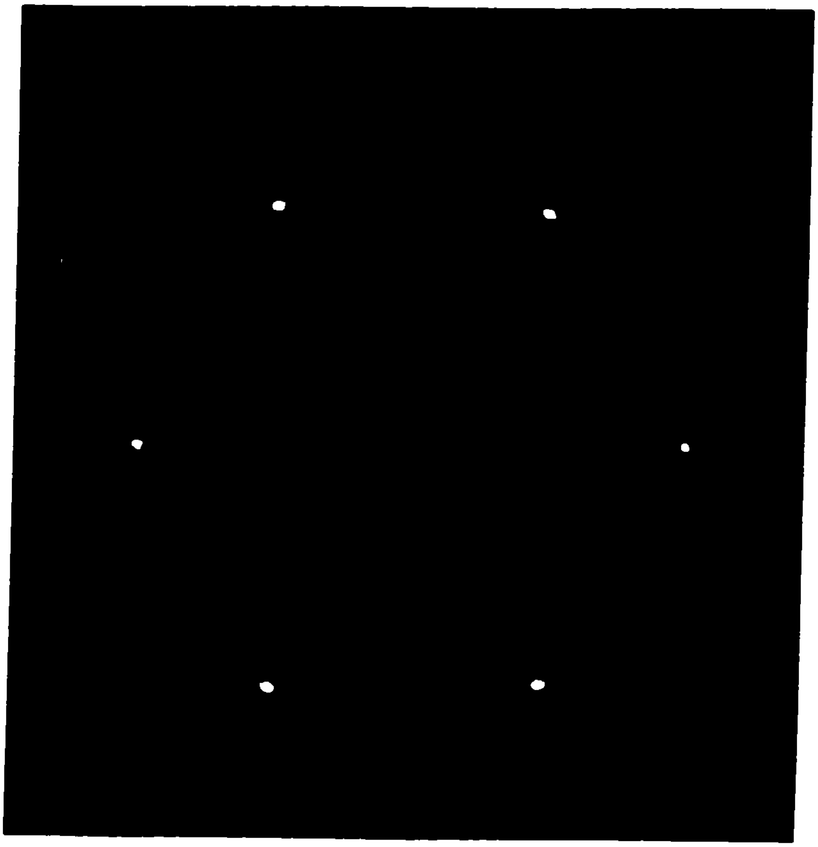

Fig. 4 - Photograph of the LEED pattern of 3ML Fe/ 2ML Ni/W(110), for a primary beam energy of 96 eV. The orientation of the tungsten substrate and Ni film in direct space is as the NW unit cells in fig. 1.

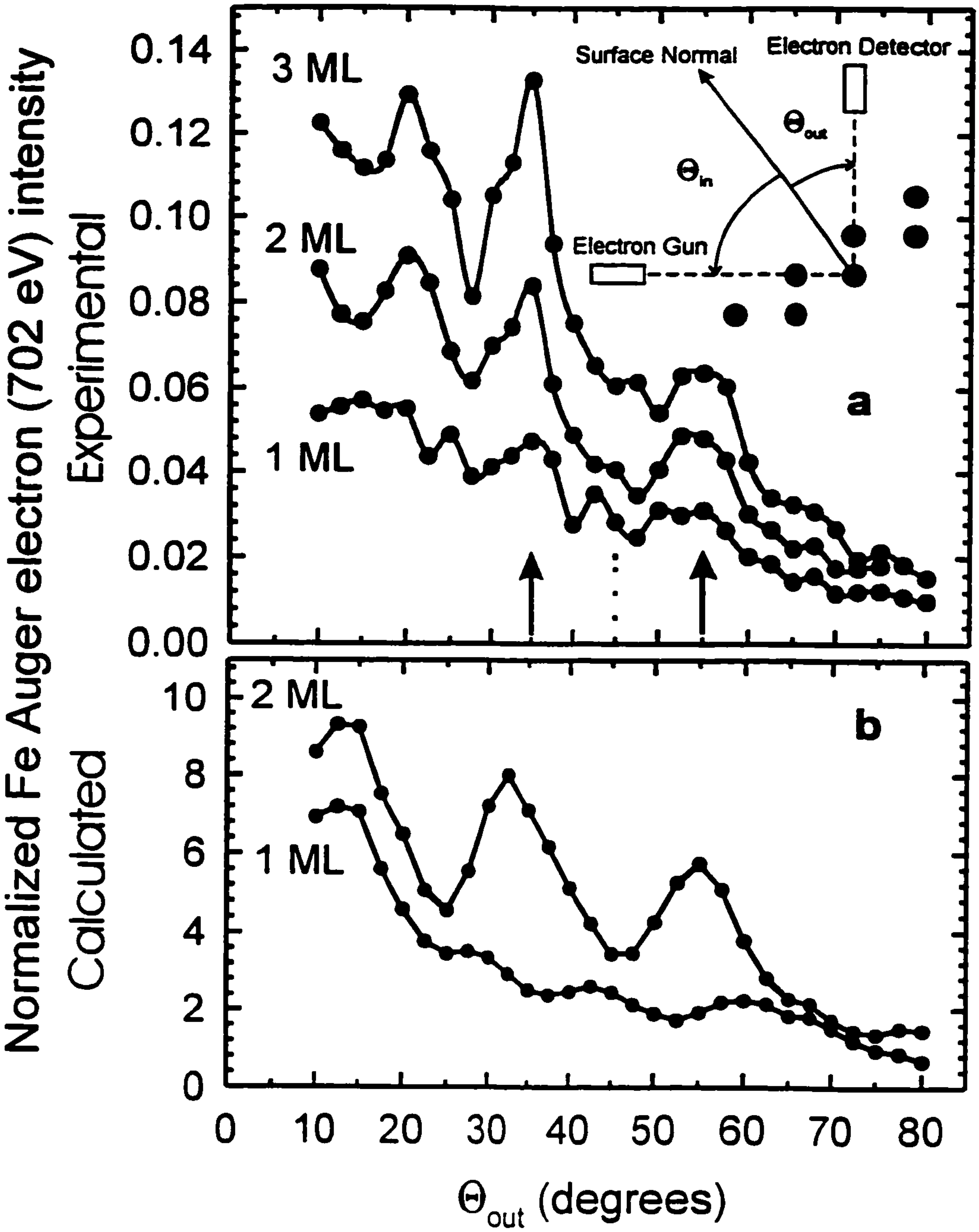

Fig. 5 - Angle-resolved Auger electron spectroscopy (ARAES) traces for Fe films on 2ML Ni/W(110). The experimental geometry is illustrated in the inset. a) Experimental results for 1, 2, and 3 ML Fe films. The expected angles for forward-focussing by a f.c.c. surface cell in the NW orientation (arrows), and by a b.c.c. surface cell aligned with the W substrate (dotted line) are marked. The curves are normalized to the same incoming primary beam flux. b) The calculated traces for a 1 and 2 ML Fe film with a f.c.c. surface cell in the NW orientation. Both incoming and outgoing focussing conditions are included, as is discussed in the text.

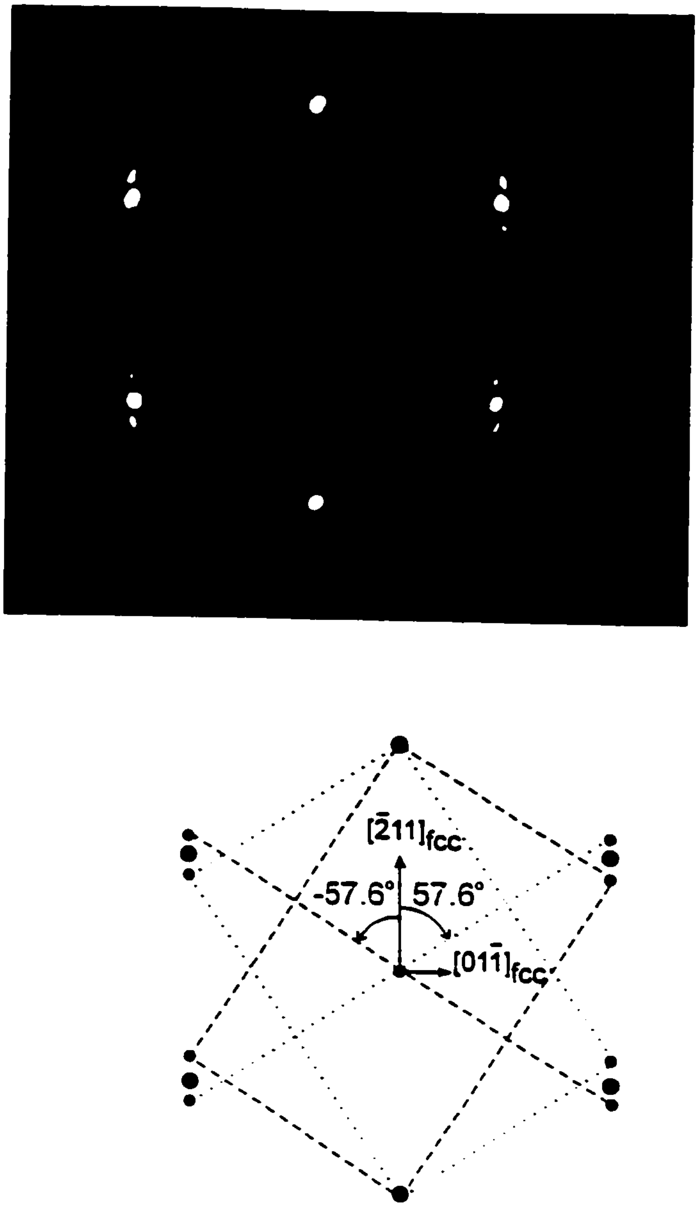

Fig. 6 - LEED patterns at a primary beam energy is 96 eV for thicker Fe films grown on 2ML Ni/W(110). LEED pattern (a) and schematic (b) are for a 4 ML Fe film. The schematic shows two distorted b.c.c. surface cells in the KS orientation of fig. 1. LEED pattern (c) and schematic (d) are for a 12 ML Fe film. The schematic shows, using open circles, a slightly distorted b.c.c. surface cell in the NW orientation of fig. 1.

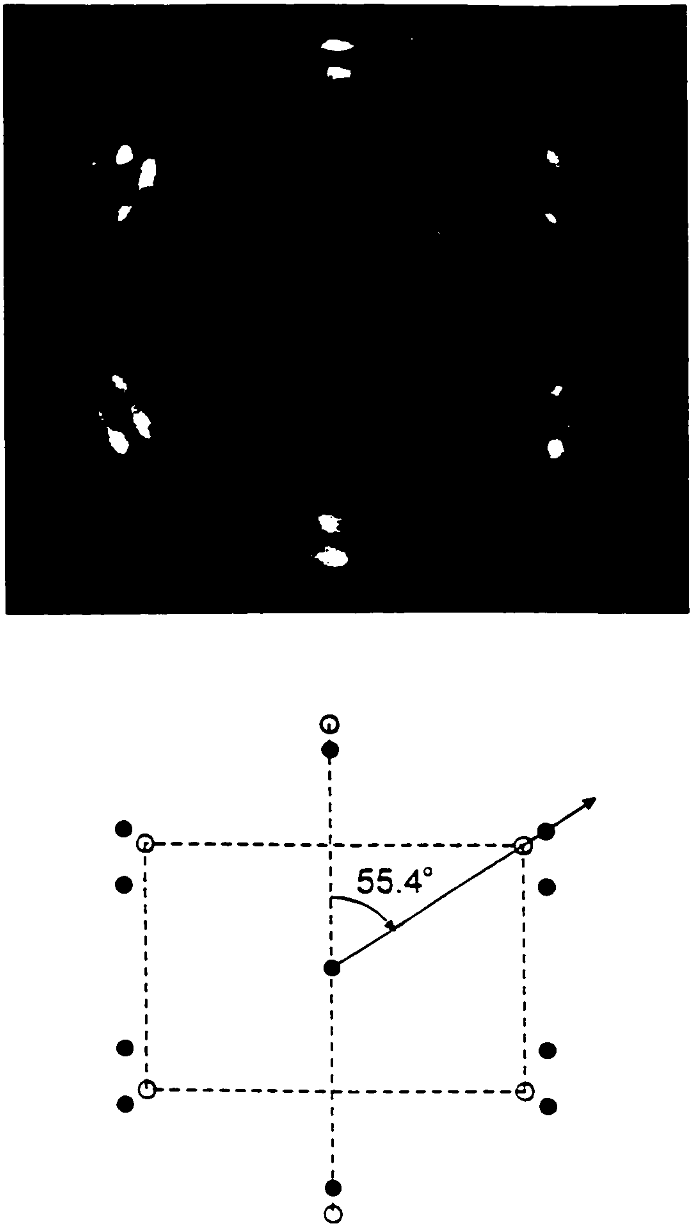

Fig. 6 - (c) and schematic (d).

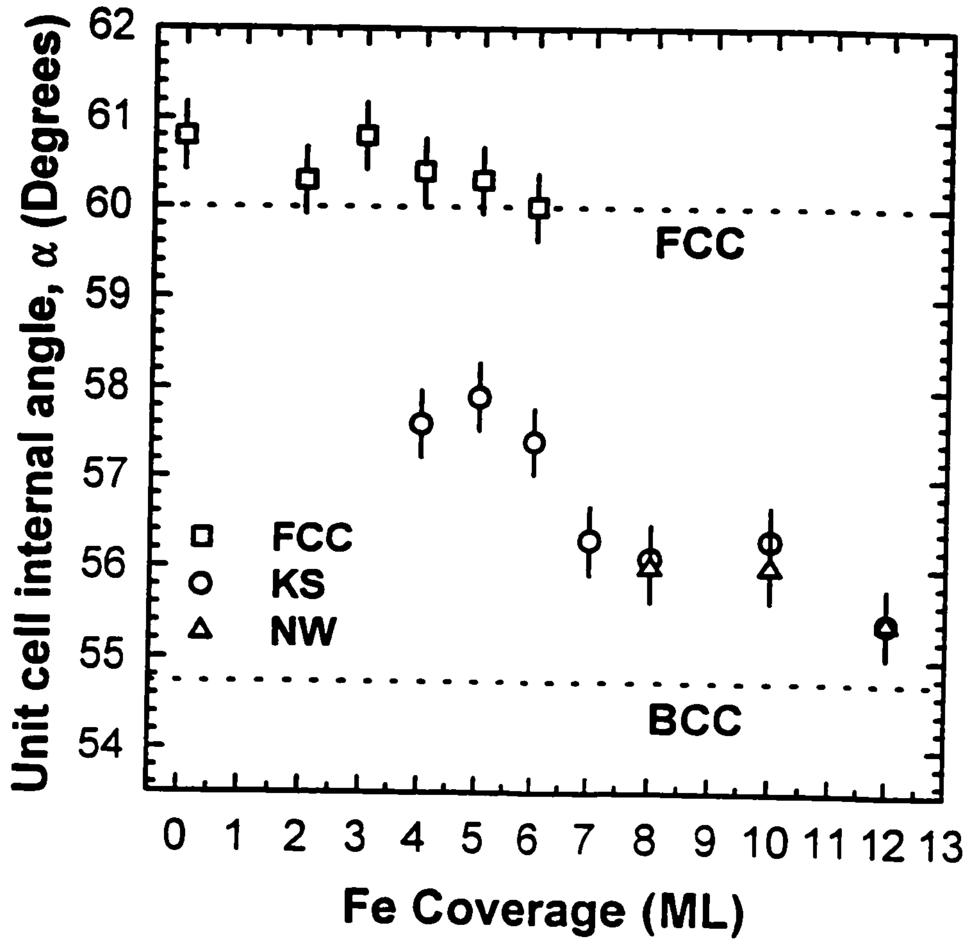

Fig. 7 - The internal angles α (defined in fig. 1) of the different surface unit cells, measured from photographs of LEED patterns, as a function of the Fe film thickness. The dashed lines show the expected angles for the f.c.c. and b.c.c. structures.

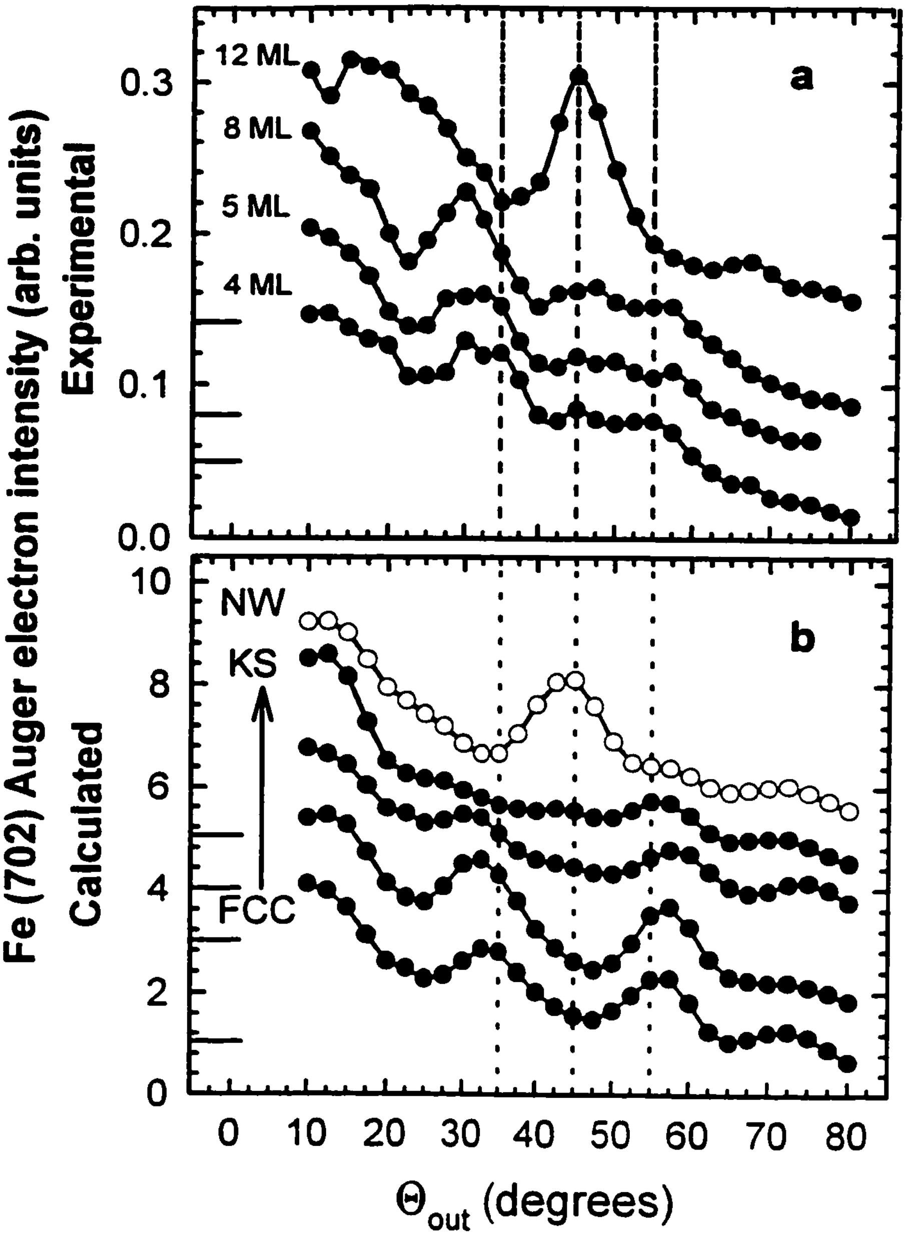

Fig. 8 - Angle-resolved Auger electron spectroscopy traces for thicker Fe films. a) Experimental results, where successive curves have been displaced an amount indicated by the extended lines on the y-axis. b) Calculated curves for different stacking positions of an Fe layer formed from the KS b.c.c.-like surface unit cells of a 4 ML film, on top of an f.c.c. unit cell for the 3ML film. The filled symbols are for stacking positions along the line AC in fig. 1. The open symbols are for the stacking position B in fig. 1. Successive curves have been displaced an amount indicated by the extended lines on the y-axis.

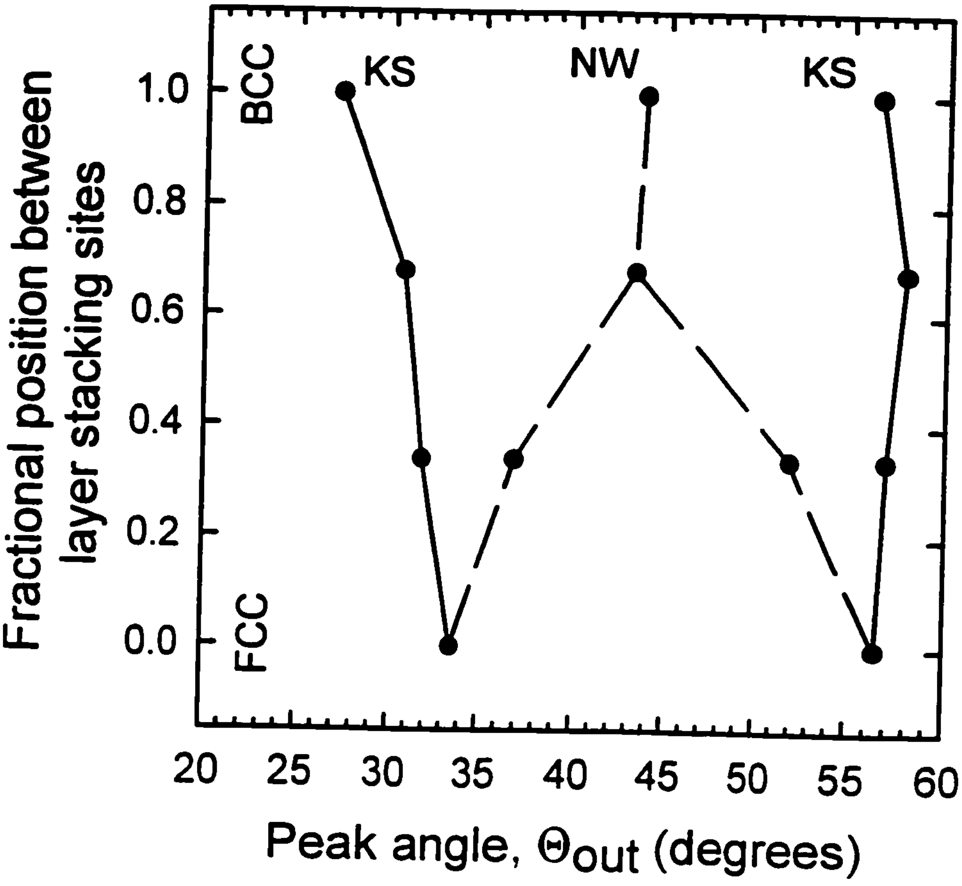

Fig. 9 - Positions of the forward-focussing peaks in the calculated ARAES traces (as in fig. 8) as a function of the stacking position along the line AC in fig. 1 (ending in the KS b.c.c. stacking position) and along the line AB in fig. 1 (ending n the NW b.c.c. stacking position).

Chapter 5

Magnetic Properties of Fe/Ni(111)/W(110) Ultra-Thin Films

Section 5.1

Introduction

In this chapter a preliminary magnetic survey of the Fe/Ni(111)/W(110) is presented. Because of time constraints, the magnetic measurements were designed to reveal the basic properties of the system. The results of this survey are very intriguing and have encouraged other researchers to take up the study of this system.

As discussed in previous chapters, the Fe/Ni(111)/W(110) films should be an ideal system to study the interplay between structure and magnetism in ultra-thin films . In the growth range of 0 to 3 ML Fe, the structure is fcc which grows in an approximate layer-by-layer manner. Therefore the evolution of the magnetism from the Ni substrate to the 3 ML Fe film should give important information about the magnetic properties of fcc(111) Fe films, without the structural problems encountered in the Fe/Cu(111) system. The Ni(111)-Fe(111) interface is also an interesting magnetic region which could be probed by studying sub-monolayer Fe coverages.

At 4 ML a structural transition from fcc to bcc occurs, which will have a profound effect on the magnetism. Once the bcc-like growth is established the structure evolves in a continuous manner towards bulk bcc. This region is also of considerable interest because it provides a magnetic system with well documented continuous structural change.

In the study presented in this chapter, measurements have been limited to the fcc region below 4 ML. Initial magnetic measurements have revealed very interesting magnetic behavior in this region. Work is currently underway in this laboratory to fully characterise the magnetic properties of this system.

Section 5.2

Magnetic Measurements

For completeness and continuity, the energy/spin analyser should be used to perform the magnetic characterisation of the Fe/Ni(111)/W(110) system. Unfortunately nature has conspired against this plan, providing a magnetic system which is particularly unsuitable for study with electrons. The problem is that the coercive fields of the Fe films are at the upper limit or beyond the capabilities of our present system. (The coercive field is the external applied magnetic field required to reverse the remanent magnetisation of the film).

The spin polarisation instrumentation was designed to study films with coercive fields below about 100 Oe. When larger magnetic field pulses are applied to the sample, ferromagnetic materials in the vacuum chamber are magnetised and tend to deflect the electron beam. The deflection appears in the data as a spurious switch in the spin polarisation.

In the Fe/Ni(111)/W(110) system coercive fields in excess of 3000 Oe are observed. This made it very difficult to study the system unless a concerted (and very time consuming) effort was made to find the offending magnetic components and remove them. Because of time constraints, the magnetic studies were made with the magneto-optic Kerr effect (MOKE).[64]

Magneto-Optic Kerr Effect

Magnetic measurements were made using a MOKE magnetometer developed by Stephen Arnold.[65] When linearly polarised light is reflected from a magnetic surface the polarisation of the light is rotated slightly. The rotation angle (the Kerr angle) is proportional to the magnetisation of the surface. The magnetic properties of the film are determined by measuring this rotation as a function of applied magnetic field. Unlike electrons, laser light is not perturbed by applied magnetic fields so measurements could be made with fields up to 3000 Oe.

A schematic of the MOKE apparatus is shown in figure 5-1. Light from a He-Ne laser is first polarised by a polarising filter and then reflected from the sample. The sample is surrounded by Helmholz coils which can create magnetic fields parallel and normal to the surface of the sample. The reflected light is then passed through a second polarising filter, after which the intensity is measured with a photodiode.

The two polarising filters are first set 90° apart so that the signal at the photodiode is extinguished. At this setting any change in the polaristion of the light at the sample results in a departure from extinction and a change in the signal at the photodiode. For small Kerr rotations this response may be linearised and optimised by moving slightly away from extinction.[65]

MOKE Measurements

Three MOKE techniques were used to study the magnetic properties of the Fe films. Hysteresis and remanent magnetisation switching experiments will be discussed in this thesis. A.c. magnetic susceptibility experiments were also performed, but at this time this technique is in the early stages of development. The results of these measurements will be published in the future.[66]

MOKE Magnetic Hysteresis Measurements (Perpendicular Magnetisation)

The measurement of magnetic hysteresis is by far the most common technique used to study the magnetic properties of a material. Hysteresis measurements are popular because they are simple to perform and contain significant information about the magnetic properties of the system.[64] To make a hysteresis measurement with MOKE a magnetic field is applied along a fixed direction and the magnitude is changed incrementally from $-H_{max}$ to $+ H_{max}$ and then back to $-H_{max}$. At each increment the Kerr intensity is measured.

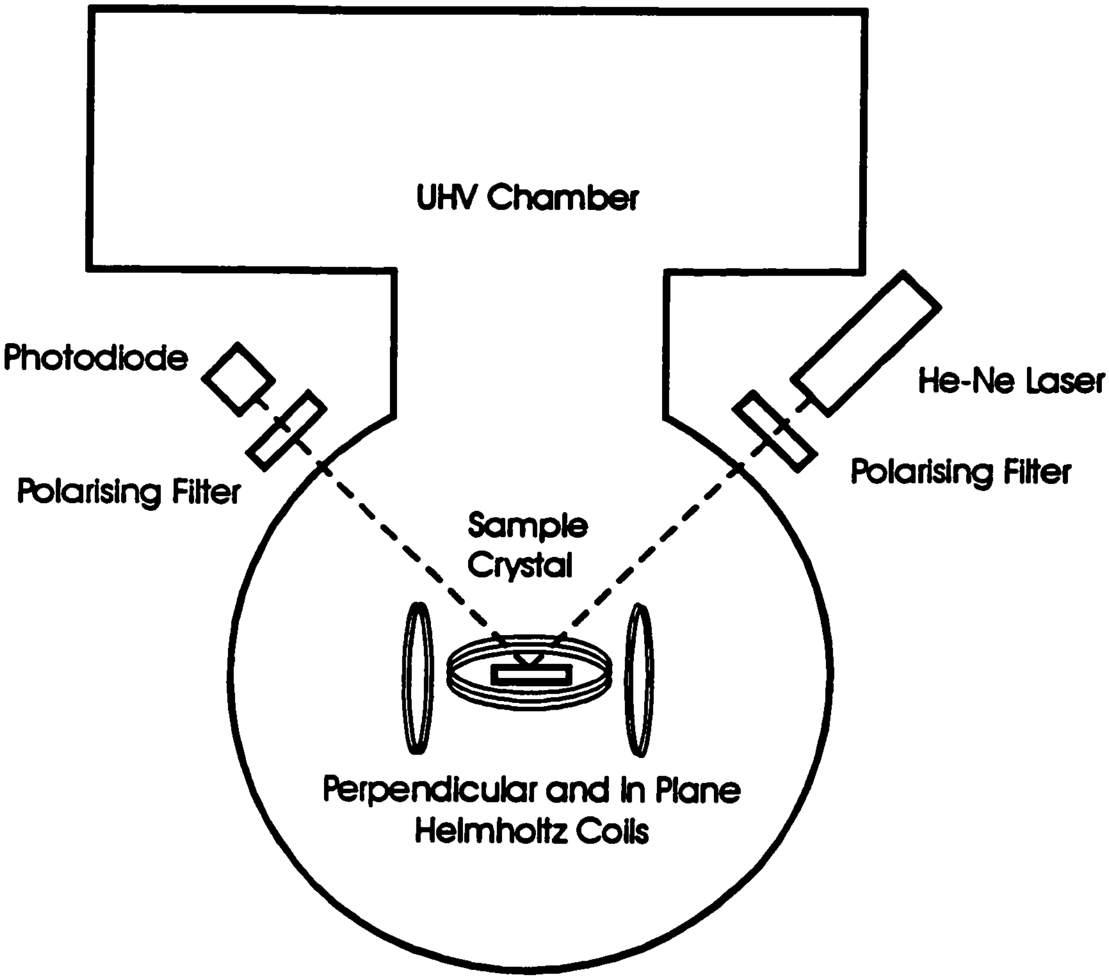

Figure 5-1
Magneto-optic Kerr effect apparatus showing the He-Ne laser, polarising filters and photodiode. The MOKE measurements are performed on the sample which is surrounded by two sets of Helmholtz coils which generate magnetic fields parallel and perpendicular to the sample surface.

Hysteresis is a fundamental property of all ferromagnets. Hysteresis refers to the fact that the response of a ferromagnet to an applied magnetic field is a function of both the magnetic field and the magnetic history of the ferromagnet (although there is no etymological connection between the words hysteresis and history!). Figure 5-2 shows a series of hysteresis measurements (or loops) made on the Fe/Ni(111)/W110) films at different temperatures and thicknesses. The details of these measurements will be discussed later. All of these data show a response in the Kerr signal to the changing magnetic field. Hysteresis is clearly evident in all but two of the Kerr loops.

Concentrating on the 1.0 ML loop in figure 5-2, the first branch of the loop from -200 to 200 Oe is plotted as circles, the second branch from 200 to -200 Oe is plotted as squares. The loop begins at the lower left where the film has been completely magnetised by the -200 Oe field. As the magnetic field is reduced, the magnetisation remains at the maximum value (the saturation magnetisation) because the film is ferromagnetic. Even as the applied field goes to zero and then reverses in direction, the magnetisation of the film does not change. Only when the coercive field is reached, does the magnetisation of the film change. For this film the coercive field (H_C) is about 110 Oe. Beyond the coercive field the film remains at the saturation magnetisation, this time in the opposite direction. As the field is changed in the opposite direction the process repeats at about -110 Oe. The 'hysteric' nature of the magnetisation occurs between $\pm H_C$ where the magnetisation is by no means a single valued function of the applied field.

The Ni Buffer

All attempts at obtaining a magnetic signal from the 2 ML Ni(111)/W(110) at temperatures between 190 and 380 K failed. This is noteworthy because Li and Baberschke report that this system is ferromagnetic with an in plane easy axis of magnetisation and a Curie temperture of 325 K.[67] It should be noted that Li and Baberschke used ferromagnetic resonance to determine the magnetic properties, not MOKE loops. MOKE is not as sensitive to in plane magnetisation as it is to perpendicular

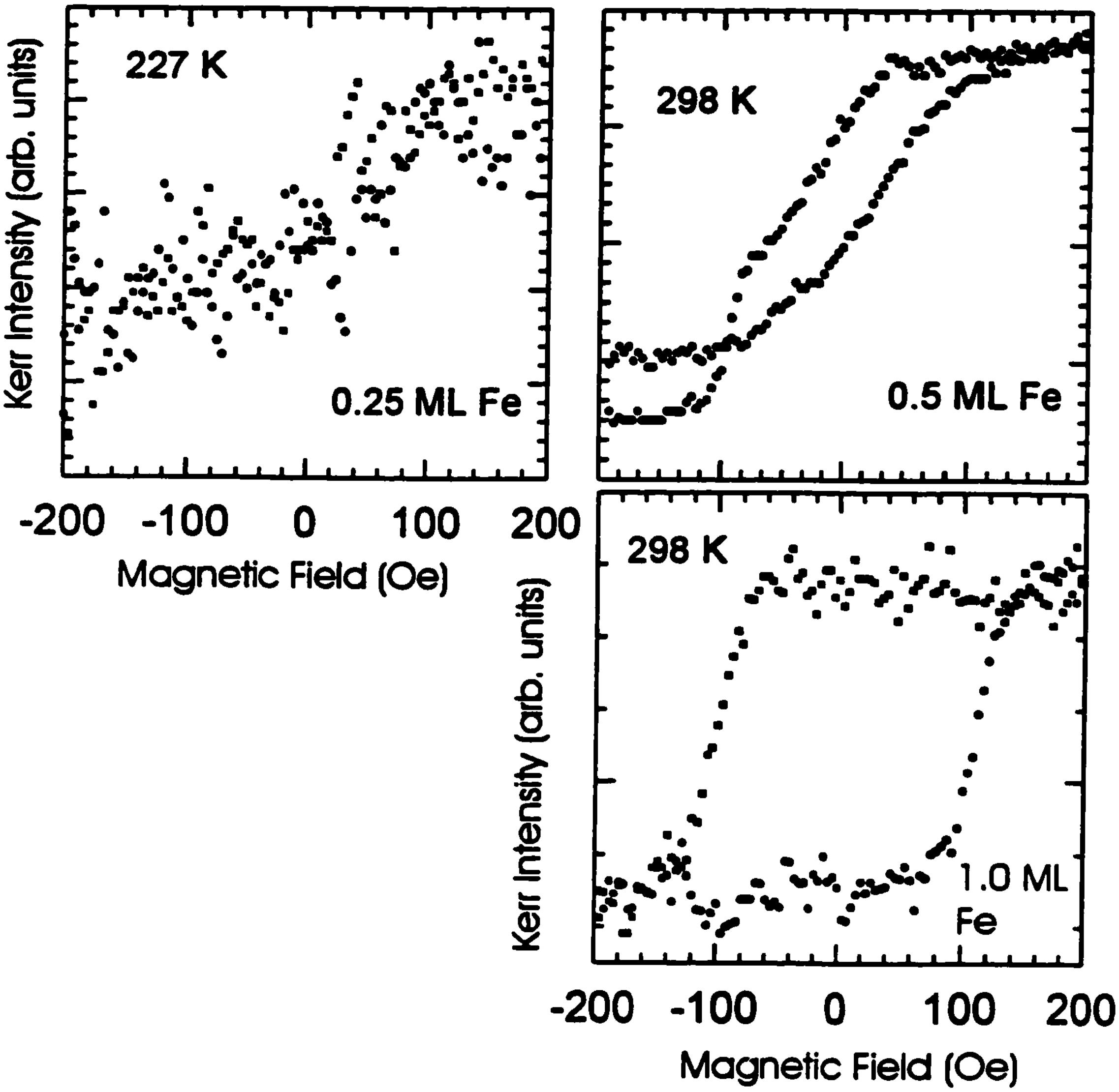

Figure 5-2
Perpendicular MOKE hysteresis measurements for 0.25 ML, 0.5 ML and 1.0 ML Fe on Ni(111)/W(110).

magnetisation. This and the small Ni magnetic moment may explain why ferromagnetism was not seen. It is also possible that differences in substrate and/or sample preparation are responsible for this discrepancy.

0.25 to 1.0 Monolayer Fe Films: Submonolayer Magnetism

Hysteresis loops for 0.25, 0.5 and 1.0 ML Fe films grown on the Ni(111)/W(110) substrate are shown in figure 5-2. The magnetic field was applied perpendicular to the surface for all three loops. The 0.5 and 1.0 ML films show clear hysteresis behavior at room temperature suggesting that these films have a perpendicular easy axis of magnetisation. The 0.25 film shows some magnetic response but hysteresis is not clearly visible.

The Curie temperature for 0.5 and 1.0 ML films is clearly above room temperature which is rather remarkable. In magnetic films the Curie temperature is expected to scale inversely with thickness in a power law relationship.[68] The result is that the Curie temperature drops very quickly for decreasing film thickness after about 5 ML. For Fe on W(100), 1.3 ML of Fe has a Curie temperature of about 125 K and Curie temperatures above 298 K were reported for films 2.4 ML and thicker.[69] For Fe on Cu(100) the Curie temperature drops from about 300 K to 100 K between 2.5 and 1.5 ML.[10]

The fact that the 0.5 and 1.0 ML films are ferromagnetic above room temperature strongly suggests that the Ni substrate is also involved in the magnetism. If both the Ni and Fe are considered, these films have a total magnetic thickness of 2.5 and 3.0 ML which are consistent with Curie temperatures above 298 K.

The magnetically active Ni hypothesis is also supported by the fact that the 0.25 and 0.5 ML Fe films show any magnetic response at all. At these coverages the films are below the magnetic percolation limit (~0.6 ML), or the minimum coverage required for the film to sustain continuous nearest neighbour magnetic coupling.[70] Such films are expected to be paramagnetic. This suggests that below the percolation limit the isolated Fe islands are magnetically coupled through the Ni buffer and therefore the Ni is a participant in the magnetism.

To further study the submonolayer magnetism a remanent magnetic switching experiment was performed. At zero applied magnetic field the ferromagnet is in a state of remanent magnetisation. The direction of the remanent magnetisation with respect to the crystalline lattice is called the easy axis of magnetisation of the system.

The remanent magnetisation of the films may be measured by applying large magnetic field pulses along the easy axis. The first pulse applied in the '+' direction leaves the film in a state of '+' remanence. The second pulse is applied with equal strength, but in the opposite '-' direction, reverses the direction of the remanent magnetisation to the '-' direction. If the Kerr intensity is measured between pulses a switching in the Kerr intensity is seen which is proportional to the magnetisation.

To make these measurements the following procedure was followed: The sample is magnetised by applying a magnetic field pulse perpendicular to the surface of the film. The rotation angle of the second polarising filter is set in the linear response region such that the signal from the photodiode is V_r. Then a magnetic pulse is applied in the opposite direction. If the magnetisation of the sample has changed, the polarisation angle of the reflected light will have rotated and the signal at the photodiode will have changed. The polarising filter is rotated until the signal returns to V_r. This angle is the Kerr rotation angle. This measurement was made 12 times per film sample and a mean Kerr rotation angle and experimental uncertainty was extracted.

When remanent measurements are made it is crucial to ensure that the magnetic pulses are sufficient in magnitude to achieve saturation (complete) magnetisation. This was done by first applying pulses in alternating directions, and increasing the magnitude of the pulses until the Kerr rotation angle stopped increasing. The pulser provided pulses

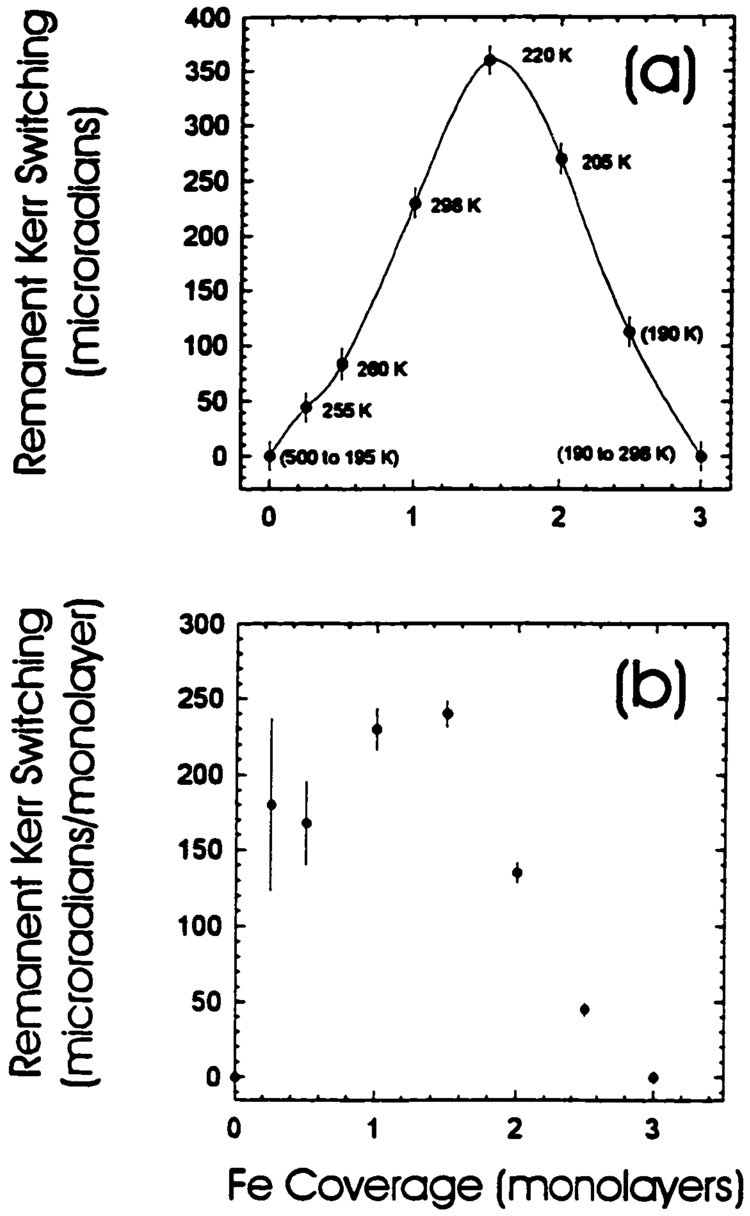

Figure 5-3
(a) Remanent Kerr switching measurements for Fe on Ni(111)/W(110) films. The temperature for each measurement is given beside the data point. Temperatures given in parentheses are discussed in the text.
(b) The same data as in (a) presented as remanent Kerr switching per Fe monolayer.

of about one millisecond duration at magnetic fields up to 3000 Oe. For all of the films studied (except for the 2.5 ML), saturation magnetisation was achieved.

Remanent magnetisation data for the Fe films from 0.25 to 3.0 ML shown in figure 5-3(a). At 0.25 ML it is clear that the film is ferromagnetic with a perpendicular easy axis of magnetisation. The remanent magnetisation increases with thickness until 1.5 ML.

Figure 5-3(b) shows the remanent magnetisation per Fe ML. In this plot it is clear that both the 0.25 and 0.5 ML Fe films have a remanent magnetisation per atom which is less than but comparable to the 1.0 ML Fe film. This is also consistent with the hypothesis that the Ni is magnetically active. In general, the magnetic moment of Ni is smaller than Fe and therefore the Ni contribution to the magnetisation is expected to be smaller than the Fe contribution.[5]

Fe Films from 1.5 to 3.0 ML

In figure 5-3(a) and (b) it is clear that something interesting is happening in the thickness range of 1.5 to 3.0 ML Fe. In this region the remanent magnetisation drops off rapidly and the sample has to be cooled before any magnetic response is seen. Figure 5-4 shows hysteresis loops at three different temperatures for a 1.5 ML Fe film. At 298 K no remanent magnetisation was measured and the film had to be cooled before hysteresis was observed.

This sudden drop in the temperature dependence of the 1.5 ML film is unexpected given the room temperature hysteresis observed in the 0.5 and 1.0 ML films . In figure 5-3(a), the temperature at which each remanent measurement was made is given beside each data point. As the thickness increased from 1.0 to 2.0 ML the films had to be cooled significantly to achieved saturation remanence. At 2.5 ML saturation remnance was not reached at 190 K, the lowest temperature available and at 3.0 ML, no remanence was seen at 190 K.

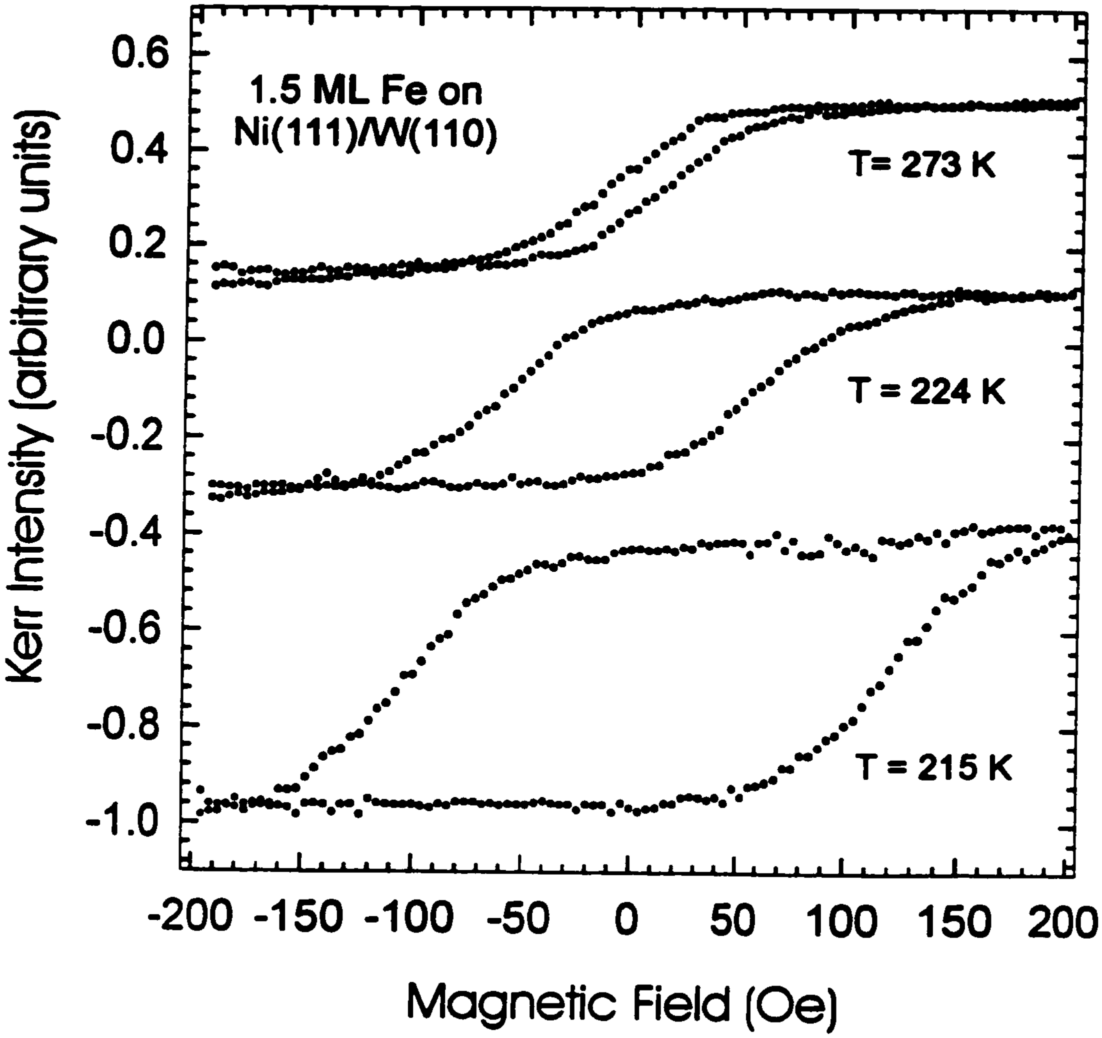

Figure 5-4
Perpendicular MOKE hysteresis measurements of 1.5 ML Fe on Ni(111)/W(110). Measurements were made at the temperatures indicated in the figure.

There are two likely explanations for this loss of perpendicular remanent magnetisation as the film thickens. The first explanation is that the nature of the magnetic coupling is changing. As mentioned in the introduction to this thesis, fcc Fe may be ferromagnetic, non-magnetic or antiferromangetic depending upon the crystal structure.[11,12] It is possible that in the Fe/Ni(111)/W(110) system the magnetic coupling changes after about 1.0 ML.

A similar transition is seen for fcc Fe grown on Cu(100) and Co(100) substrates.[11,14] In both of these systems room temperature growth first produces a ferromagnetic face centered tetragonal (fct) film which shows perpendicular magnetism to coverages of about 5 ML. At 5 ML the structure of the whole film appears to change to fcc and the films become anti-ferromagnetic (or possibly non-magnetic) except for a ferromagnetic 'live layer' at an interface (The Fe/vacuum interface on the Cu(100) substrate and the Fe/Co interface on the Co(100) substrate).

In the Fe/Ni(111)/W(110) system the structure does not change between 1.0 and 3.0 ML and is strained fcc throughout. However there is an important point which must be made. Fcc refers to a three dimensional lattice with a unit cell three layers thick in the (111) direction. Below three layers these films are simply close packed. Therefore it is possible that as the film grows into the third dimension, the magnetic coupling becomes non-magnetic or antiferromagnetic and the magnetisation decreases. From the submonolayer results it is clear that the Ni is participating in the magnetism. If the total amount of magnetic material is considered (Ni + Fe), the magnetisation begins to decline at 3.0 ML, which coincides with the completion of one fcc unit cell. Therefore it is possible that a change in the magnetic coupling is reducing the magnetisation of the film.

Spin Reorientation Transformation

A more likely explanation for the decline in magnetisation above 1.0 ML is a spin reorientation transition. This type of transition is also seen in the Fe/Cu(100) system when the Fe growth temperature is below about 200 K.[11] In a spin reorientation transition the easy axis of magnetisation changes from perpendicular to parallel to the plane of the film as the film thickness increases.[15] This is a consequence of the change in the relative importance of the surface, volume and shape magnetic anisotropy energies as the film thickness changes (see chapter one).

In the Fe/Cu(100) system the reorientation transition is characterised by three regions. At low coverages the system has a perpendicular easy axis of magnetisation. At about 6 ML Fe, a sharp drop in remanent magnetisation occurs over about 0.5 ML thickness. This followed by a region about 1.0 ML thick where both perpendicular and in plane remanent magnetisation coexist. This is followed by a sharp increase in the remanent magnetisation in the plane of the film and a region above about 7 ML where no perpendicular remanent magnetisation is seen.

Figure 5-5 shows both perpendicular and in plane hysteresis loops for 2.5 and 3.0 ML Fe films. For the in plane loops the magnetic field was applied along the fcc<211> direction. At 2.5 ML, the Fe film shows clear perpendicular remanent magnetisation at 190 K. The in plane hysteresis loop also shows a weak magnetic response which looks like a hard axis Kerr loop (a Kerr loop taken with the magnetic field applied in a direction other than the easy axis and therefore no remanent magnetisation is observed).[6] However, remanent magnetisation measurements made with the pulser indicated that the 2.5 ML film had a very small in plane remanent magnetisation. Therfore at 2.5 ML small perpendicular and in plane remanent magnetisations were observed in coexistence.

At 3.0 ML coverage the perpendicular Kerr measurement made at 190 K shows a hard axis response where the saturation magnetisation has not been reached. Also shown is an in plane Kerr loop for the same film taken at room temperature. This Kerr loop shows clear hysteresis and remanent magnetisation, suggesting that at 3 ML the easy axis is in plane. Also shown in figure 5-4 is an in plane Kerr loop of a different 3.0 ML film. This loop was taken at 380 K and clearly shows in plane magnetisation with an easy axis along the fcc<211> axis.

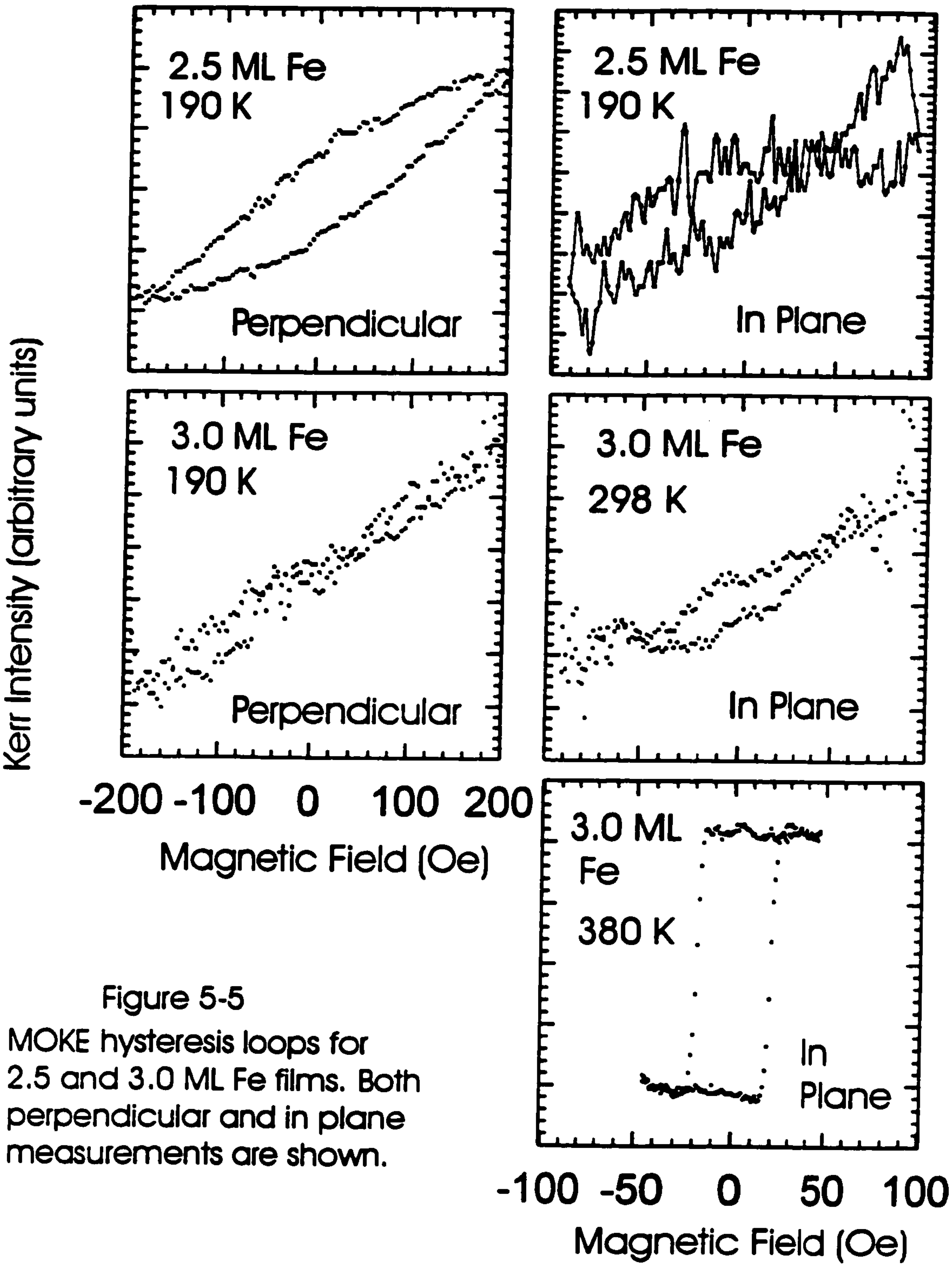

Figure 5-5
MOKE hysteresis loops for 2.5 and 3.0 ML Fe films. Both perpendicular and in plane measurements are shown.

At 3.0 ML no perpendicular remanent magnetisation was detected using the magnetic field pulser. This suggests that at 3.0 ML the easy axis of magnetisation is now in the plane of the film. From the 2.5 and 3.0 ML data it is clear that the easy axis of magnetisation changes from perpendicular to in plane. This and the coexistence of perpendicular and inplane easy axes at 2.5 ML strongly suggests that a reorientation transformation occurs in the Fe/Ni(111)/W(110) system at thicknesses between 2.5 and 3.0 ML. If the Ni is included, the transition occurs between 4.5 and 5.0 ML coverage.

It is interesting to note that this transition appears to occur at lower coverages than the Fe/Cu(100) system. This suggests that the surface anisotropy for the Fe/Ni(111) films is smaller than that for Fe/Cu(100). The surface anisotropy energy for Fe(111)/Cu(111) films has been observed to be about half that of Fe(100)/Cu(100) films.[9] For Ni(111) films the surface anisotropy energy favours an in plane easy axis.[9] Therefore it is likely that the Fe/Ni(111) films will have a weak perpendicular anistropy and therefore a spin reorientation transition which occurs at a lower coverage.

Conclusion

Preliminary magnetic studies of the Fe/Ni(111)/W(110) system reveal two interesting phenomena. For coverages from 0.25 to 1.0 ML Fe ferromagnetism is observed at temperatures at and slightly below room temperature. This strongly suggests that the Ni is participating in the perpendicular magnetism. This is interesting for two reasons. The first is that all attempts at measuring a magnetic signal from the 2 ML Ni buffer failed. Therefore it appears that only a small amount of Fe (0.25 ML) is required to induce perpendicular magnetism in the Ni. The second interesting point is that ultrathin Ni(111) films have an in plane easy axis of magnetisation and therefore 0.25 ML of Fe appears to be sufficient to change the direction of the easy axis.

At coverages above 1.0 ML the magnetic behavior appears to be consistent with that of a spin reorientation transformation. The fact that the transformation occurs at lower Fe coverages than that observed for the Fe/Cu(100) system is consistent with the expectation that the perpendicular anisotropy for the Fe(111)/Ni(111) system is smaller than that for the Fe/Cu(100) system.

Chapter 6

Discussion and Conclusions

The main emphasis of this work is the relationship between the structure and magnetism of ultrathin films. The study of the growth of Fe/Ni(111)/W(110) illustrates how the structure of ultrathin films can change dramatically over several monolayers thickness. Because the magnetic properties of a material are a strong function of the structure, this shows that good structural characterisation is essential to the understanding of ultrathin film magnetism.

It also must be emphasised that the characterisation of ultrathin films should involve a number of complementary surface probes. In this study LEED which probes long range structural order was complemented with ARAES which probes nearest neighbour structural relationships. The orientational relationship between the fcc and bcc domains was deduced from the LEED patterns and stacking relationship between successive layers was deduced from ARAES giving a complete picture of the fcc to bcc transition.

The ARAES technique which uses structure sensitive high energy Auger electrons was complemented by the Auger intensity versus deposition technique which uses low energy Auger electrons that are very sensitive to changes in film thickness. Although the intensity versus deposition method suggested near layer by layer growth, significant interdiffusion of Fe and Ni could only be ruled out after ARAES measurements were made.

Careful analysis of the growth mode of the Fe films has identified a region of high quality strained fcc growth between 0 and 4 ML coverage. In this growth region, a preliminary magnetic survey suggests that a spin reorientation transformation occurs between 2.5 ML and 3.0 ML Fe coverage . Because a careful structural study of the system was performed it can be stated with certainty that the reorientation of the magnetisation from perpendicular to in plane occurs when the Fe film has a strained fcc structure. This is an important conclusion because it has been observed in other fcc Fe systems that a transition from perpendicular to in plane magnetisation occurs at the structural transition from fcc to bcc.[11,14,16]

As a result of this work, further research into the magnetic properties of the Fe/Ni(111)/W(110) system may be undertaken with a comprehensive understanding of the structure. Investigations are currently underway at McMaster and at the Max Planck Institute for Microstructure Physics in Germany and promise to reveal important information about the nature of magnetism.

References

[1] A good scientific and technological review is by Jelto Smits, Physics World (November 1992) 48.

[2] C. Rau et al, Phys. Rev. Lett. **57** (1986) 3221.

[3] W.F. Egelhoff Jr. and M.T. Kief, Phys. Rev. **B45** (1992) 7795.

[4] A good introduction to intinerant magnetism is by W.A. Harrison, **Electronic Structure and Properties of Solids** (W.H. Freeman, San Francisco, 1980.)

[5] J.G. Gay and R. Richter in **Ultrathin Magnetic Structures** I (J.A.C. Bland and B. Heinrich ed., Springer-Verlag, Berlin, 1994).

[6] S. Chickazumi, **Physics of Magnetism** (Wiley, New York, 1964).

[7] G.H.O. Daalderop, P.J. Kelly and M.F.H. Schuurmans in **Ultrathin Magnetic Structures** I (J.A.C. Bland and B. Heinrich ed., Springer-Verlag, Berlin, 1994).

[8] M.D. Mermin and H. Wagner, Phys. Rev. Lett. **17** (1966) 1133.

[9] W.J.M. de Jonge, P.J.H. Bloemen and F.J.A. den Broeder in **Ultrathin Magnetic Structures** I (J.A.C. Bland and B. Heinrich ed., Springer-Verlag, Berlin, 1994).

[10] S.D. Bader, Dongqi Li and Z.Q. Qiu, J. Appl. Phys. **76** (1994) 6419.

[11] Dongqi Li et al, Phys. Rev. Lett. **72** (1994) 3112.

[12] V.L. Moruzzi *et al*, Phys. Rev. **B34** (1986) 1784.

[13] J.S. Kouvel and R.H. Wilson, J.Appl, Phys. **32** (1961) 435.

[14] W.L. O'Brien and B.P. Tonner, Surf. Sci. **334** (1995) 10.

[15] S.D. Bader, Dongqi Li and Z.Q. Qiu, J. Appl. Phys **76** (1994) 6419

[16] J. Thomassen et al, Phys. Rev. Lett. **69** (1992) 3831.

[17] J.G. Gay and R. Richter in **Ultrathin Magnetic Structures** I (J.A.C. Bland and B. Heinrich ed., Springer-Verlag, Berlin, 1994).

[18] M.T. Kief and W.F. Egelhoff Jr. Phys. Rev. **B47** (1993) 10785

[19] A. Modinos, **Field, Thermionic and Secondary Electron Emission Spectroscopy,** (Plenum Press, New York, 1984).

[20] D. Roy and J.D. Carette, **Electron Spectroscopy for Surface Analysis** (Topics in Current Physics 4, H. Ibach ed. Springer Berlin 1977) 13-58.

[21] D. Mauri, R. Allenspach and M. Landolt, J. Appl. Phys. **58** (1985) 906.

[22] D. Roy and D Tremblay, Rep. Prog. Phys. **53** (1990) 1621

[23] J. Sawler and D. Venus, Rev. Sci. Instrum **62** (1991), 2409.

[24] D. Venus, Rev. Sci. Instrum. **62** (1991), 1361.

[25] T.L. Jones, J. Sawler and D. Venus, Rev. Sci. Instrum. **64** (1993) 2008.

[26] T.L. Jones and D. Venus, Surface Science **302** (1994), 126.

[27] D. Venus and H.L. Johnston, Phys. Rev. **B50** (1994), 15 787.

[28] R. Feder, **Polarized Electrons at Surfaces,** (Springer-Verlag, Berlin, 1985), 61.

[29] E. Kisker, M Campangna, W. Gudat and E Kuhlman , Rev. Sci. Instrum. **50** (1979). 1598.

[30] E.M. Purcell, Phys. Rev. **54** (1938), 818.

[31] E. Harting and F.H. Rhead, **Electrostatic Lenses,** (Elsevier, Amsterdam, 1976).

[32] G. Martinez, M. Sancho and F.H. Rhead, J. Phys. E: Sci. Instrum **16** (1983), 631.

[33] P. Grivet, **Electron Optics** (Pergamon, London, 1972).

[34] D.A. Dahl and J.E. Elmore, Idaho National Laboratory Engineering Report EGG-CS-7233 (1987).

[35] K. Jost, J. Phys. E: Sci. Instrum. **12** (1979), 1001.

[36] Supplied by Acheson Colloids, Brantford, Ontario.

[37] Supplied by Duramic/Wesgol Palisades Park, New Jersey, U.S.A.

[38] T. Rikitake, **Magnetic and Electromagnetic Shielding** (Terra, Tokyo, 1987).

[39] Supplied by the Magnetic Shield Corp. Bensenville, Illinois, USA.

[40] E.J. Scheibner and L.N. Tharp, Surface Science **8** (1967) 247.

[41] M.A. Van Hove, W.H. Weinberg and C.-M. Chan, **Low-Energy Electron Diffraction** (Springer-Verlag, Berlin, 1986).

[42] J. Kolaczkiewicz and E. Bauer, Surf. Sci.,**144** (1984) 495.

[43] U. Gradmann an G. Waller, Surf. Sci.,**116** (1982) 539.

[44] Andrew Zangwill, **Physics at Surfaces** (Cambridge University Press, Cambridge U.K. 1988).

[45] E. Bauer, Appl. Surf. Sci. **11/12** (1982) 479.

[46] A. Brodde and H. Neddermeyer, **Ultramicroscopy** (1992) 42.

[47] John R. Smith and Amitava Banerjea, Phys. Rev. Lett. **59** (1987) 2451.

[48] E. Bauer and Jan van der Merwe, Phys.Rev. **B33** (1986) 3657.

[49] Andries Rinse Miedema, Z. Metallkde **69** (1978) 455.

[50] W.F. Egelhoff Jr, in **Ultrathin Magnetic Structures I** (J.A.C. Bland and B. Heinrich eds., Springer-Verlag, Berlin, 1994)

[51] B.H. Bransden and C.J. Joachain, **Physics of Atoms and Molecules** (Longman, London, 1983).

[52] T.L. Jones, M.Sc. Thesis (McMaster University, 1993).

[53] C. Daniel and F.S. Wood, **Fitting Equations to Data** (Wiley, New York, 1980).

[54] D. Venus and B. Heinrich, Phys. Rev. **B53** (1996) 1733.

[55] W.F. Egelhoff Jr., Phys. Rev. Lett. **59** (1987) 559.

[56] A.P. Kaduwela, D.J. Friedman and C.S. Fadley, J. Electron Spectrosc **57** (1991) 223.

[57] D.J. Friedman and C.S. Fadley, J. Electron Spectrosc. **51** (1990) 689.

[58] J.J. Rehr, R. C. Albers and J. Mustre de Leon, Physica **B158** (1989) 417.

[59] Y. Gao and Jianming Cao, Phys. Rev. B43 (1991) 9692.

[60] S. Chambers. Adv. Physics 40 (1991) 357.

[61] S. Tanuma, C.J. Powell and D.R. Penn, J. Vac. Sci. Technol. **A8** (1990) 2213.

[62] S. Tanuma, C.J. Powell and D.R. Penn, J. Electron Spectrosc. **52** (1990) 285.

[63] William H. Press, Brian P. Flannery, Saul A. Teukolsky and William T, Vetterling, **Numerical Recipes** (Cambridge University Press, Cambridge, U.K., 1986).

[64] S.D. Bader and J.L. Erskine in **Ultrathin Magnetic Structures II** (B. Heinrich and J.A.C. Bland ed. Springer-Verlag, Berlin, 1994).

[65] C.S. Arnold and D. Venus, Rev. Sci. Instrum. **66** (1995) 3280.

[66] C.S. Arnold, H.L. Johnston and D. Venus, to be published.

[67] Yi Li and K. Baberschke, Phys. Rev. Lett. **68** (1992) 1208.

[68] G.A.T. Allan, Phys. Rev. **B1** (1970) 352.

[69] H.J. Elmers and J. Hauschild, Surf. Sci. **320** (1994) 134.

[70] H.J. Elmers *et al*, Phys. Rev. Lett. **73** (1994) 898.

Appendix 1
The Energy Resolution of the 90^0 SDA

The energy resolving properties of the 90^0 SDA may be derived from the lens equations, shown truncated after second order:

$Y_{out} / R_0 = \alpha_{in} + \Delta K/K_0 - (Y_{in} / R_0)^2$ (Equation 1a)

$\alpha_{out} \quad = -Y_{in} /R_0 + \Delta K/K_0$ (Equation 1b)

Where α_{in} and α_{out}, are the angular divergences from a tangential orbit at the entrance and exit of the analyser and Y_{in} and Y_{out} are the entrance and exit radial divergence from R_0. All these parameters are shown in figure (5).

Now consider (1a) with a parallel input beam ($\alpha_{in} = 0.$) And limit Y_{out} by fixing an aperture radius at the exit of the SDA of r.

The maximum and minimum energies which may pass are given by:

$\Delta K_{max} /K_0 = r/R_0 + (Y_{in} / R_0)^2$ (Equation 1c)

$\Delta K_{min} /K_0 = -r/R_0$ (Equation 1d)

Combining (1c) and (1d) we obtain:

$(\Delta k_{max} - \Delta k_{min})/K_0= 2 \cdot r/R_0 + (Y_{in} / R_0)^2= \Delta K_b/K_0$ (Equation 1e)

Where ΔK_b is the base resolution. The full width at half maximum of the analyser is estimated to be:

$\Delta K_{fwhm}/K_0 = 0.5 \cdot (\Delta k_b/K_0) = r/R_0 + 0.5 \cdot (Y_{in} / R_0)^2$ (Equation 1f)

Now if we consider a non-tangential converging beam ($\alpha_{in} \neq 0$) entering the SDA at R_0 ($Y_{in}=0$) in the same way we obtain:

$\Delta K_{max} /K_0 = -\alpha_{in}$ (Equation 1g)

$\Delta K_{min} /K_0 =\alpha_{in}$ (Equation 1h)

Combining (1g) and (1h) as for (1e) and (1f) we obtain:

$\Delta K_{fwhm}/K_0= \alpha_{in}$ (Equation 1i)

If we combine equations (1f) and (1i) we obtain the energy resolution to first order:

$$\Delta K_{fwhm}/K_0 = \alpha_{in} + r/R_0 + 0.5\cdot(Y_{in} / R_0)^2 \qquad \text{(Equation lj)}$$

IMAGE EVALUATION
TEST TARGET (QA-3)

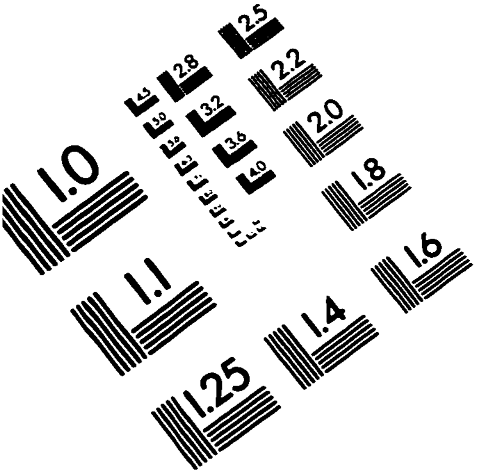

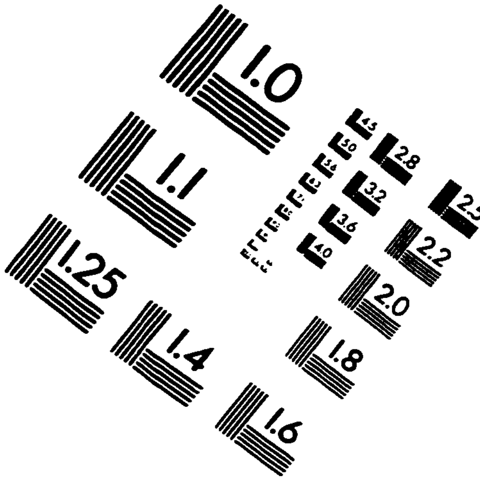

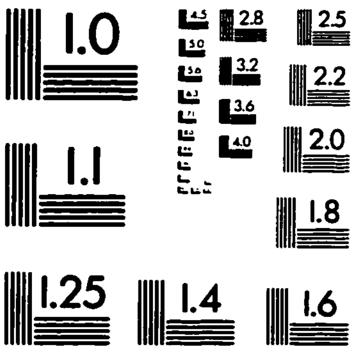

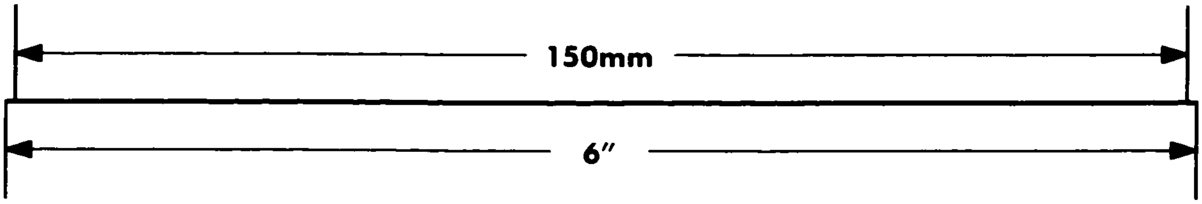

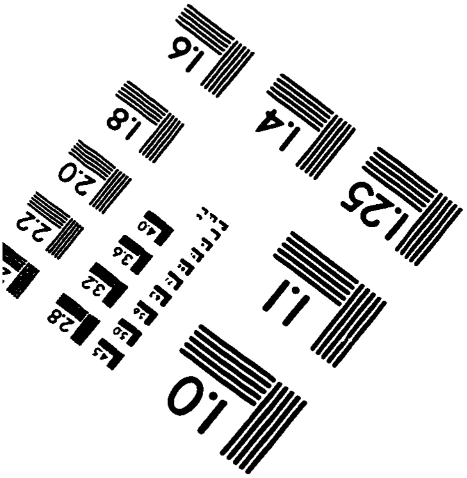

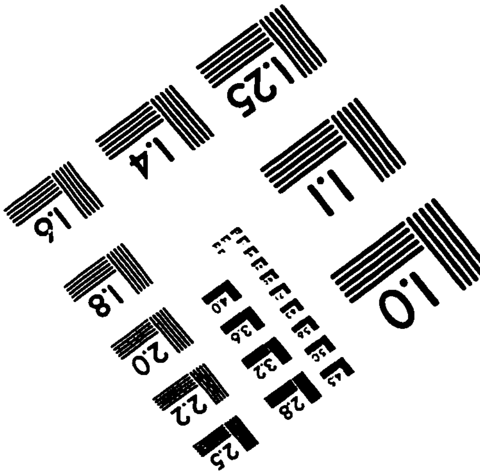

APPLIED IMAGE, Inc
1653 East Main Street
Rochester, NY 14609 USA
Phone: 716/482-0300
Fax: 716/288-5989